University of Alberta

Search for Microscopic Black Holes in Multijet Final States with the ATLAS Detector using 8 TeV Proton-Proton Collisions at the Large Hadron Collider

by

Asif Saddique

A thesis submitted to the Faculty of Graduate Studies and Research in partial fulfillment of the requirements for the degree of

Doctor of Philosophy

in

Experimental High Energy Physics

Department of Physics

Fall 2014
Edmonton, Alberta

Dedicated

To
Professor Riazuddin (RIP),
the father of physics in Pakistan,
a great physicist and human being.

Abstract

Microscopic black holes are expected to produce a high multiplicity of Standard Model (SM) particles having large transverse momenta in the final state. In this thesis, a search for microscopic black holes in multijet final states with the ATLAS 2012 data using 8 TeV centre of mass energy of proton-proton collisions at the Large Hadron Collider is performed in a data sample corresponding to an integrated luminosity of 20.3 fb^{-1}. The search is simplified to multijet final states because most of the expected SM particles produced from black hole decay would lead to hadronic jets. The data events with high-transverse momenta have been analysed for different exclusive jet multiplicities, i.e. $2, 3, ..., 7$, and inclusive jet multiplicities, i.e. $\geq 3, 4, ..., 7$. In this multijet analysis, Quantum Chromodynamics (QCD) multijet production is the main background. For all the multijet final states, the data distributions for the sum of jet transverse momenta ($H_T = \sum p_T$) in an event have been observed to be consistent with QCD expectations. For inclusive multijet final states, model-independent and model-dependent exclusion limits at a 95% confidence level are set on the production of new physics and non-rotating black holes, respectively. The model-independent upper limit on cross section times acceptance times efficiency is 0.29 fb to 0.14 fb for jet multiplicities ≥ 3 to ≥ 7 for $H_T > 4.0$ TeV. The model-dependent lower limits on minimum black hole mass are set for different non-rotating black hole models.

Acknowledgements

In the name of Allah, the Most Gracious, the Ever Merciful. His kind mercy made it possible to finish my thesis.

My deepest thanks and gratitude go to my supervisor Dr. Douglas M. Gingrich for his support, patience, guidance and providing me an excellent research environment. His flexible attitude always provided a space to work independently, and his professional skills allowed for timely guidance for me. I would also like to thank all of the CPP faculty and staff members for creating a comfortable working atmosphere. I also appreciate all the facilities and the wonderful learning environment provided by the Department of Physics at the University of Alberta.

Because of the help and great support of kind people around me, the task of finishing my thesis became easier and achievable. I would especially thank my senior colleague and postdoctoral fellow Dr. Francesc Vives Vaque, whose polite and encouraging attitude always helped me a lot to boost this work. Besides work, my wife Fauzia Sadiq and I always enjoyed family gatherings with his family.

I would like to acknowledge my current and ex-fellows in the ATLAS Alberta group: Patrick, Andrew, Samina, Nooshin, Kingsley and especially Aatif Imtiaz Butt and Dr. Halasya Siva Subramania for having useful discussions with me regarding this work.

I would like to thank my ex-supervisor Dr. James Pinfold for his support and supervision in the initial phase of my PhD. I also thank my ex-colleagues Long Zhang and Dr. Nitesh Soni for providing me help to train myself in doing data analysis. I, and my wife also, have a lot of good memories of spending time with Nitesh's family.

How can I forget one of impressive personalities whom I met in Canada, Logan Sibley. I learned one thing from him – how to sacrifice your time to help people around you. I also thank him for spending his time for doing a careful proof reading of this thesis.

I am thankful to all of my family friends, Atif, Asad, Omer, Zawar, Jamil, Nadia, Amna andTayyaba, who made our stay enjoyable in Canada. We have had several trips and gatherings during my studies in Canada. Thanks for your wonderful company.

I would love to acknowledge my beloved wife for her caring attitude and moral support in all aspects of my life. She is a wonderful life partner. I would also deeply thank my mother, father (RIP), brothers and sisters for praying and encouraging me to move forward in my life, especially my mother, who always remained worried and loving for me.

Table of Contents

List of Tables

List of Figures

List of Abbreviations and Symbols

ALFA	Absolute Luminosity For ATLAS
ALICE	A Large Ion Collider Experiment
ATLAS	A Toroidal LHC Apparatus
BCM	Beam Condition Monitor
BX	Bunch Crossing
CDF	Collider Detector at Fermilab
CERN	European Organization for Nuclear Research
CF	Correction Factor
CL	Confidence Level
CMS	Compact Muon Solenoid
CR	Control Region
CTEQ	Coordinated Theoretical-Experimental project on QCD
D0	D-Zero Experiment at Fermilab
DSID	Data Set IDentifier
EF	Event Filter
EM	ElectroMagnetic
FCAL	Forward CALorimeter
GRL	Good Run List
HEC	Hadronic Endcap Calorimeter
ID	Inner Detector
IP	Interaction Point
JER	Jet Energy Resolution
JES	Jet Energy Scale
LAr	Liquid Argon

LHC	Large Hadron Collider
LO	Leading Order
LUCID	LUminosity measurement using Cerenkov Integrating Detector
MBTS	Minimum Bias Trigger Scintillator
MC	Monte Carlo
MDT	Muon Drift Tube
MSSM	Minimal Supersymmetric Standard Model
NLO	Next to Leading Order
NMSSM	Next to Minimal Supersymmetric Standard Model
NNLO	Next to Next to Leading Order
NPV	Number of Primary Vertices
NR	Normalization Region
PDF	Parton Distribution Function
QCD	Quantum ChromoDynamics
QED	Quantum ElectroDynamics
QFT	Quantum Field Theory
RMS	Root Mean Square
ROI	Region Of Interest
RPC	Resistive Plate Chamber
SCT	Silicon Central Tracker
SM	Standard Model
SR	Signal Region
SUSY	Supersymmetry
TGC	Thin Gap Chamber
TRT	Transition Radiation Tracker
ZDC	Zero Degree Calorimeter

n	Number of extra spatial dimensions
D	Sum of four usual and number of extra dimensions, i.e. $D = 4 + n$
M_{EW}	Electroweak scale
M_P	Planck scale (in 4 D)
M_D	Multidimensional or true Planck scale
M_{BH}	Black hole mass
$\mathscr{R}$	Size of extra dimension
$\mathscr{A}(\omega)$	Grey body factor of a black hole
l_P	Planck length corresponding to M_P
l_D	Planck length corresponding to M_D
r_H	Event horizon radius of a black hole
p_T	Transverse momentum of a jet
H_T	Sum of the jet transverse momenta
N	Number of jets in the final state or jet multiplicity
η	Pseudorapidity
ϕ	Azimuthal angle around the beam axis
μ	Number of interactions per bunch crossing
σ	Total Cross section

Chapter 1

Introduction

The large difference between the electroweak ($M_{EW} \sim 0.1$ TeV[1]) and the Planck scales ($M_P \sim 10^{16}$ TeV) is known as the hierarchy problem. In other words, gravity appears to be very weak as compared to the SM forces. Technically, the problem can also be expressed in terms of the large difference between the physical Higgs boson mass and the Planck mass. The physical Higgs boson mass lies near the electroweak scale, which is much smaller than the Planck mass. If the SM is valid up to the Planck scale then the bare mass of the Higgs boson has a natural value of order of the Planck scale. In this case, an incredible fine tuning ($\sim 10^{17}$) of the cancellation of the radiative corrections and the bare Higgs boson mass is required to obtain a low value for the physical Higgs boson mass to the order of the electroweak scale. The hierarchy problem can also be solved if new gravitational physics exists near the electroweak scale. In this scenario, a new fundamental Planck scale of the order of the electroweak scale is defined. The contribution from the radiative corrections to the bare Higgs boson mass is much smaller than the previous case. Hence a large tuning of the corrections and the bare Higgs boson mass is not required to solve the hierarchy problem.

[1] It is assumed $\hbar = c = 1$ throughout this thesis.

The production of microscopic black holes in the high energy proton-proton (pp) collisions at the LHC is one of the most exciting predictions of low-scale quantum gravity models [1–5]. These models are motivated by the hierarchy problem and explain the weakness of gravity as compared to the other SM forces. According to some of the low-scale gravity models [1–3], gravity is the only force that propagates in the extra dimensions (n) while the other forces are confined to the four observed dimensions. Therefore, the apparent gravity measured in the four dimensional physical world corresponding to the large Planck scale M_P is always much weaker than the actual gravity measured in $D = 4+n$ dimensions corresponding to the true Planck scale (M_D). The low-scale ($\sim$ TeV) gravity would appear strong enough to be compared to the other SM forces and, as a consequence, the formation of the massive and extra-dimensional objects such as microscopic black holes may occur at the LHC.

In this thesis, a microscopic black hole search based on the predictions of low-scale gravity models in high energy pp collisions with 8 TeV centre of mass energy ($\sqrt{s}$) at the LHC collected by the ATLAS detector in the year 2012 will be presented. The data correspond to a total integrated luminosity of 20.3 fb^{-1} with a luminosity uncertainty of 2.8%[2]. The low-scale gravity models predict that short-lived ($\sim 10^{-27}$ sec) microscopic black holes would decay in the detectors and leave some distinguishable signature such as events with high multiplicities (number of particles in the final states) and high transverse momenta (p_T). The black hole decay produces particles primarily according to the SM degrees of freedom (number of charge, spin, flavour and color states), which mainly leads to jets of hadrons in the final states. Therefore, our search for microscopic black holes is focussed on multijet final states. Observations of such multijet final

[2] The uncertainty in luminosity for the ATLAS 2012 data is derived by using the same method adopted for the 2011 ATLAS data, which is shown in Ref. [6].

states having high p_T may provide valuable information about the nature of black holes, the dimensionality of space-time and the fundamental Planck scale.

The main variable chosen for this study is H_T, the scalar sum of p_T of jets in an event. The H_T distributions are expected to have the same shape for different jet multiplicities for the main QCD background in this study [7–10]. This shape invariance with multiplicity is the key assumption of this analysis used to estimate the QCD background for the expected microscopic black hole signals at the LHC.

In chapter 2, SM physics and motivations for the physics beyond the SM are discussed. The theories with extra dimensions are important candidates for the potential extension of the SM, and predict the production of microscopic black holes at the LHC. Since a search for microscopic black holes at the LHC is the main scope of this thesis, microscopic black hole physics is briefly described along with some practical implications for observing them at the LHC.

Chapter 3 is dedicated to the description of the LHC and the ATLAS detector at the CERN. Various sub-detectors of the ATLAS detector are discussed according to their functionality, importance and use in this study. The trigger and the data collection system of the ATLAS detector are also discussed at the end of chapter 3.

Chapter 4 presents the main analysis, illustrating the necessary tools, assumptions, procedure and results of the study for the search of microscopic black holes in multijet final states of the ATLAS 2012 dataset. The data used in the analysis are studied for different jet multiplicities with the assumption of H_T shape invariance with jet multiplicity for QCD events, which is directly determined from the data with corrections due to the effects of non-invariance derived from MC simulations. A summary of

the study will be made by showing model-independent limits on the production of new physics and model-dependent limits on the production of microscopic black holes. The overall summary of the analysis is discussed in chapter 5. In addition to the primary analysis, my other contributions to the ATLAS experiment are described in appendix A.

Chapter 2

Standard Model Physics and Beyond

2.1 Introduction

The SM is the most established theoretical framework of particle physics. Many modern particle detectors, for example ATLAS and CMS at the LHC have not found any evidence against the foundations of the SM. This theory has enjoyed many major experimental successes, like the discovery of $W^{\pm}$ and Z^0 bosons, the top quark, and now the discovery of Higgs boson.

The SM is not a "theory of everything" because it neither incorporates gravity nor does it explain many open questions, for example, why the weak force is 10^{32} times stronger than the gravitational force, the matter-antimatter asymmetry, the nature of dark matter and dark energy, the strong CP problem and neutrino oscillations. These are the primary reasons to build theoretical models beyond the SM of particle physics.

In this chapter, a brief introduction to the SM and its major limitations will be described along with some theories beyond the SM. There are many possible extensions of the SM and the theory of large extra dimensions is one of the important candidates. The production of microscopic black holes is an important consequence of the theory of large extra dimensions, which is the model used in this thesis. The physics of microscopic black holes will be discussed by describing their production, nature and decay. In the last section of this chapter, the observables that might show the

possible signatures of microscopic black holes at the LHC will be described.

2.2 The Standard Model of Particle Physics

The SM of particle physics is the theory that describes the role of the fundamental particles and interactions between them. All the known matter is composed of particles from the SM. There are two types of particles in the SM, the fundamental fermions (leptons, quarks and their antiparticles) and the fundamental bosons (gauge bosons and the Higgs boson). The fermions are half-integer spin particles, whereas bosons are integer spin particles. There are six leptons classified in three generations. The electron (e) and the electron neutrino (ν_e) are in the first generation, the muon (μ) and the muon neutrino (ν_μ) are in the second generation and the tau (τ) and the tau neutrino (ν_τ) make the third generation. Similarly, there are six quarks in three generations, up (u) and down (d) in the first generation, strange (s) and charm (c) in the second generation and bottom (b) and top (t) in the third generation. Each quark can have three colours, red (r), green (g) and blue (b), but no free colour charge exists in nature at long distances. Except for the special case of the top quark[1], quarks only appear in bound states called hadrons like the proton (uud) and pion ($u\bar{d}$).

There are four fundamental interactions in nature: the electromagnetic, the weak, the gravitational and the strong force. Every interaction has mediators: the photon for the electromagnetic force, two W's and a Z boson for the weak force, eight gluons for the strong force and maybe the graviton for gravity. The gluons themselves carry colour and anti-colour and therefore do not exist as isolated particles, but they can exist within hadrons or in colourless combinations (glueballs). Although the SM does not expain gravity, it has incorporated the other known forces into a sin-

[1] The mean lifetime of top quark is predicted to be 5×10^{-25} s [11], which is shorter than the timescale for strong interactions, and therefore it does not form hadrons.

gle model. This model has achieved many experimental successes over the years and provided significant predictions, such as the existence of the top quark, and the masses of the weak force carriers.

The SM forces are governed by three gauge theories, Quantum Electrodynamics (QED), Quantum Chromodynamics (QCD), and Electroweak interactions from the Glashow-Weinberg-Salam model. The Standard Model is a gauge theory based on the product group $\mathrm{SU}_C(3)\times\mathrm{SU}_L(2)\times\mathrm{U}_Y(1)$ associated with the colour (C), weak and hypercharge (Y) symmetries. The subscript L indicates that the charged weak interaction involves couplings only to the chiral left-handed component of the fermion. In the SM, all the gauge theories are required to be invariant under global and local gauge transformations.

QED is an abelian and renormalisable gauge theory with symmetry group U(1). This theory describes the interactions between spin-1/2 charged particles, the electromagnetic interactions. The theory provides a description of the interactions between two charged particles by the exchange of a field quantum, the photon.

QCD is a non-abelian and renormalisable gauge theory based on SU(3) group that describes the interaction of quarks via gluons. The non-abelian nature of the SU(3) group results in self interaction terms of gluons generating three and four-gluon vertices in the theory, which leads to a strong coupling, large at low energies and small at high energies. As a consequence QCD has two important features, confinement and asymptotic freedom. According to confinement, the quarks generally are confined in hadrons and an infinite amount of energy is required to separate a quark to infinity from its hadron. For example, if the quark and antiquark move far enough apart in a meson, then field energy increases to produce two new mesons instead of creating two free quarks. According to asymptotic

freedom, the strength of strong coupling is small at very small distances such that quarks and gluons interact weakly and behave as free.

Electroweak theory is a unified description of the electromagnetic and weak interactions. The massive gauge bosons are the mediators of the weak force. The fermions (leptons and quarks) and the gauge bosons are required to be massless in gauge theories. The massive leptons and quarks, and $W^{\pm}$ and Z gauge bosons, are accommodated in the gauge theories by the Higgs mechanism. Accordingly the local symmetry of the gauge group $\mathrm{SU}_L(2)\times\mathrm{U}_Y(1)$ is spontaneously broken and a Higgs field is generated that interacts with other fields to produce not only the massive gauge bosons, but also the masses of leptons and quarks. The mechanism also postulates the existence of a massive scalar particle known as the Higgs boson.

2.2.1 Electroweak Theory and Higgs Mechanism

The electroweak gauge theory is the unified description of electromagnetic and weak interactions under the gauge group $\mathrm{SU}_L(2)\times\mathrm{U}_Y(1)$. The electroweak Lagrangian density can by written as a combination of two parts [12]

$$\mathscr{L}_{EW} = \mathscr{L}_{symm} + \mathscr{L}_{Higgs}. \tag{2.1}$$

The first part of the Lagrangian density ($\mathscr{L}_{symm}$) involves only the gauge bosons and interactions of all fermions (including quarks and leptons). The Higgs part of the Lagrangian density ($\mathscr{L}_{Higgs}$) is for a neutral scalar field (ϕ) and its interaction with the fermionic field (ψ), can be written as

$$\mathscr{L}_{Higgs} = (D_\mu\phi)^\dagger(D_\mu\phi) - V(\phi^\dagger\phi) - \overline{\psi}_L\Gamma\psi_R\phi - \overline{\psi}_R\Gamma^\dagger\psi_L\phi, \tag{2.2}$$

where Γ, include all the coupling constants, are the 3×3 diagonal matrices[2] that make the Yukawa couplings invariant under the Lorentz and gauge

[2] The diagonal elements of a Γ matrix provide three coupling constants to the three generations of fermions.

groups, and μ is a four vector index, i.e., $\mu = 0, 1, 2, 3$. D_μ is the covariant derivative, which will be described later in this section. In the minimal SM, all the left-handed fermionic fields (ψ_L) are doublets and right-handed fermonic fields (ψ_R) are singlets. A doublet scalar filed ϕ is considered in order to generate fermion masses. Equation (2.2) is further divided into two parts, the pure scalar and Yukawa interaction Lagrangian densities

$$\mathscr{L}_{Higgs} = \mathscr{L}_{\phi} + \mathscr{L}_{Yukawa}. \tag{2.3}$$

The Yukawa interaction part is

$$\mathscr{L}_{Yukawa} = -\overline{\psi}_L \Gamma \psi_R \phi - \overline{\psi}_R \Gamma^\dagger \psi_L \phi. \tag{2.4}$$

The scalar part of equation (2.2) can be written as

$$\mathscr{L}_{\phi} = (D_\mu \phi)^\dagger (D_\mu \phi) - V(\phi^\dagger \phi). \tag{2.5}$$

The potential term $V(\phi^\dagger \phi)$ is symmetric under the SU(2)×U(1) group, which is written as

$$V(\phi^\dagger \phi) = -\frac{1}{2}\mu_1^2 \phi^\dagger \phi + \frac{1}{4}\lambda_1 (\phi^\dagger \phi)^2. \tag{2.6}$$

Here μ_1 and λ_1 are real and positive constants. In order to incorporate the massive fields in the SM, the gauge symmetry is broken spontaneously by introducing a non-zero vacuum expectation value in theory. The vacuum expectation value of scalar field ϕ is the value giving a minimum of the potential V and is written as

$$\langle \phi_0 \rangle \equiv \langle 0 | \phi(x) | 0 \rangle = v \neq 0, \tag{2.7}$$

where $\langle \phi_0 \rangle$ is the ground state expectation value of scalar field ϕ. By using the above non-zero value of the minimum potential in equation (2.4) for the Yukawa interaction, it is possible to obtain a fermionic mass matrix

$$M = \overline{\psi}_L \mathcal{M} \psi_R + \overline{\psi}_R \mathcal{M} \psi_L, \tag{2.8}$$

with

$$\mathcal{M} = \Gamma\langle\phi_0\rangle, \tag{2.9}$$

where $\langle\phi_0\rangle$ can be written in a doublet form as

$$\langle\phi_0\rangle = \begin{pmatrix} 0 \\ v \end{pmatrix}. \tag{2.10}$$

The left-handed fermions ψ_L are doublets and all the right-handed fermions ψ_R are singlets in the SM, therefore, only Higgs doublets would be able to give masses to the fermions. One complex Higgs doublet is sufficient for the construction of fermionic masses [12]. The couplings of the physical Higgs H to the gauge bosons can be obtained by replacing

$$\phi = \begin{pmatrix} 0 \\ v + (H/\sqrt{2}) \end{pmatrix} \tag{2.11}$$

in equation (2.2), the first term of the covariant derivative can be written as

$$D_\mu\phi = \left[\partial_\mu + ig\sum_{A=1}^{3} t^A W_\mu^A + \frac{i}{2}g'YB_\mu\right]\phi. \tag{2.12}$$

Here g and g' are the coupling constants for the SU(2) and U(1) gauge groups, t^A and Y are the generators of the group SU(2)×U(1), whereas W_μ^A and B_μ are the gauge fields for the SU(2) and U(1) gauge groups. The index $A = 1, 2, 3$ corresponds to the fields of three gauge bosons, W^+, W^- and Z^0, respectively.

Similarly, the mass terms for the $W^\pm$ and Z^0 bosons can be obtained by using the non-zero expectation value in equation (2.5). In this scenario, only the symmetry of the SU(2) group is spontaneously broken, whereas the U(1) group maintains its symmetry. The weak mediators $W^\pm$ and Z^0 therefore obtain masses and the electromagnetic mediator (the photon) remains massless. In other words, the spontaneous symmetry breaking of SU(2)×U(1) group splits the electroweak force into two separate forces, the weak force and the electromagnetic force.

The predicted $W^{\pm}$ and Z^0 bosons by the SM of particle physics have been discovered at the CERN in 1983 [13]. This is considered one of the major achievements of the SM of particle physics.

The search for the Higgs boson was the main goal of the LHC at CERN, the most important missing link of the SM. The discovery of the Higgs boson has been confirmed by the ATLAS and CMS collaborations at the LHC [14, 15]. This particular milestone is considered a great achievement in the history of particle physics.

2.2.2 Limitations of the Standard Model

The energy scales explored up to now demonstrate the success of the SM to an impressive level. Despite this, there are some real challenges for the SM which are the key motivations to search for new physics, or physics beyond the SM. Some major limitations are:

- Since the SM relies on Quantum Field Theory (QFT) and does not cover the scope of the classical theory of general relativity, therefore the fundamental force of gravity is not described by the SM.

- There are more than 20 arbitrary parameters in the SM, e.g., the gauge coupling constants, three angles and a phase in the Cabibbo-Kobayashi-Maskawa matrix [16]. For these constants, the SM takes measurements from experiments.

- The SM was constructed to have massless neutrinos, but neutrinos are observed to have a non-zero mass [17].

- The SM does not provide a good reason for the only three generations of leptons and why charges are always quantised.

- The SM does not explain the large asymmetry between matter and antimatter.

- The SM does not explain the large difference between the electroweak scale and the Planck scale, i.e., the hierarchy problem.

- The SM does not explain the nature of dark matter and dark energy. It does not contain any dark matter particle consistent with the properties of cosmological observations.

In order to address these type of issues, many theories have been developed to describe the physics beyond the SM.

2.3 Physics Beyond the Standard Model

Physics beyond the SM, or often referred to as new physics, is needed to satisfy many deficiencies of the SM. There are many theories which are possible candidates of new physics. For example, people have developed supersymmetric theories (Minimal Supersymmetric Standard Model (MSSM) and Next-to-Minimal Supersymmetric Standard Model (NMSSM)), string theory, M-theory and theories of extra dimensions. All these theories have different approaches towards a unified theory.

This study is based on the theories of extra dimensions. According to this concept, gravity propagates in the extra dimensions (one warped or several large extra dimensions depending on the model) and appears to be strong like other SM forces at the length scale smaller than the fundamental scale (electroweak). As a consequence of strong gravity at small scales, microscopic black holes may be produced in high energy pp collisions at the LHC. These types of theories will be described in the next subsection.

2.3.1 Theories of Extra Dimensions

The concept of extra dimensions followed quite naturally from Einstein's general theory of relativity. Einstein's field equations have a potential of

extending the theory for any arbitrary dimensionality without any mathematical inconsistency. Einstein's equation can be written as

$$R_{\mu\nu} - \frac{1}{2} g_{\mu\nu} R = 8\pi T_{\mu\nu}, \tag{2.13}$$

where $R_{\mu\nu}$ is know as Ricci curvature tensor, $g_{\mu\nu}$ is the metric tensor, R is the scalar curvature and $T_{\mu\nu}$ is the stress-energy tensor. Equation (2.13) contains second-rank tensors whose indices can have any value depending on the spacetime dimensionality. Soon after Einstein's theory of gravity, Kaluza proposed his five dimensional gravitational model. In this model, he introduced one extra spacelike dimension. Later, Klein explained the topology of the extra dimension that it is like a spacelike dimension compact within finite length ($\mathscr{R}$). To be consistent with the observations, the size of the extra dimension must be much smaller than any observable scale. The Kaluza-Klein (KK) gravitational model was the first attempt of a unified theory in which gravity was a fundamental force.

Over the years, the idea of extra dimensions was frequently used in string theory where most commonly six extra spacelike dimensions were taken into account. In string theory, the size of the extra dimensions was assumed to be $\mathscr{R} = {l_P}^3 = 10^{-33}$ cm by using mathematical and physical reasonings. In the 1990s, the theories of extra dimensions entered in a new era when some of the string theories [18–21] gave the idea that the string scale does not necessarily need to be tied to the traditional Planck scale, $M_P = 10^{19}$ GeV. On the basis of these ideas, two types of important theories of extra dimensions were introduced, the theory of large extra dimensions [1–3] and the theory of a warped extra dimension [4, 5]. The former type was introduced in 1998 by Arkani-Hamed, Dimopoulos and Dvali, known as the ADD model. The later was introduced in 1999 by Randall and Sundrum, known as the Randall-Sundrum (RS) model.

[3] Planck length corresponding to M_P

Both types of extra dimensional models use the concept of the brane and the bulk. In string theory, the 4-dimensional space is called the brane and the $(4+n)$-dimensional space is called the bulk, where n is the number of extra spatial dimensions. The SM particles are restricted to the brane which is embedded in the bulk, whereas non-SM particles such as gravitons can also propagate in the extra dimensions.

ADD Model

According to this model, all the SM fields are localized in the 4-dimensional brane while gravitons, possibly scalars and any other non-SM fields can propagate into the full $(4 + n)$-spacetime. The strength of gravity is also shared by the extra spatial dimensions which are hidden at the electroweak scale. Gravity therefore appears to be weak in $(3 + 1)$-spacetime dimensions. The extra spatial dimensions are always compact with finite size $\mathscr{R}$ whereas the usual $(3 + 1)$-spacetime dimensions are infinite. Therefore, in this scenario, M_{EW} and $\mathscr{R}^{-1}$ are the two fundamental scales in nature. With the concept of large extra dimensions [1–3], $\mathscr{R} \gg l_P$ and assuming all extra dimensions have the same size, it is possible to relate the four dimensional Planck scale to the fundamental or extra dimensional Planck scale (M_D) by

$$M_P^2 \backsimeq \mathscr{R}^n M_D^{2+n}. \tag{2.14}$$

The subscript $D = n + 4$ represents the total number of dimensions or the sum of the number of extra dimensions n and the four physical dimensions. By using $G_D = 1/M_D^{2+n}$, the above equation can be transformed into an equation for the gravitational constants as

$$G_D \backsimeq G_4 \mathscr{R}^n. \tag{2.15}$$

The Newtonian gravitational potential between two masses m_1 and m_2 separated by $r \gg \mathscr{R}$ in four dimensions follows the ordinary Newton's law

measured in nature, which is written as

$$V(r) = G_4 \frac{m_1 m_2}{r}. \tag{2.16}$$

The potential between m_1 and m_2 separated by $r \ll \mathscr{R}$ will be much stronger than in the previous case because we are now sensitive to all dimensions, and is postulated as

$$V(r) = G_D \frac{m_1 m_2}{r^{n+1}}. \tag{2.17}$$

From equations (2.16) and (2.17), it can be concluded that the gravitational force follows a $1/r^{2+n}$ law at short length scales, whereas it follows the usual $1/r^2$ law at larger scales. Therefore, the real strength of gravity can appear only at short distances, smaller than the size of the extra dimensions. In this theory, different sizes and numbers of extra dimensions can provide different values of M_D from the same constant M_P by obeying equation (2.14). By expressing $M_P \sim 10^{16}$ TeV in terms of the length scale, i.e. $l_P \sim 10^{-35}$ m, and assuming $M_D \sim 1$ TeV with corresponding length scale $l_D \sim 10^{-19}$ m, equation (2.14) can also be written as

$$\mathscr{R} = 10^{\frac{32}{n} - 19}\text{m}. \tag{2.18}$$

Here it is important to note that as n increases, the size of the extra dimensions get smaller, for example, $\mathscr{R} \sim 10^{13}$ m for $n = 1$, $\mathscr{R} \sim 10^{-3}$ m for $n = 2$ and $\mathscr{R} \sim 10^{-9}$ m for $n = 3$. The $n = 1$ case represents deviation from Newton's gravity over solar system distances and is experimentally excluded. The $n = 2$ case is also ruled out by torsion-balance experiments [22]. Therefore, within current experimental limits, it can be assumed that at least three extra dimensions are required to observe a deviation from Newton's inverse square law. The SM fields are accurately measured at the electroweak scale, which indicates the SM fields do not feel extra dimensions.

If the large extra dimension scenario is true, then strong gravity at short scales can result in the formation of microscopic black holes, which will be discussed in detail in section 2.4.1. The short-lived microscopic black holes will decay mostly into SM particles, producing significant signals for the brane observer, as will be discussed in section 2.4.4.

Randall-Sundrum Model

This is an alternate approach to solve the hierarchy problem and relies on a single extra spatial dimension. There are two types of RS models, RS I [4] and II [5]. In type I, the single extra dimension is bounded by two $(3+1)$-branes, as shown in Figure 2.1. All the SM fields live on the visible brane that is at a finite distance $y = L$ from a hidden brane located at $y = 0$. All the fundamental scales at the hidden brane are of the order of $M_{D'}$, which reduce exponentially to the order of electroweak scale on the visible brane, i.e.,

$$M_{EW} = e^{-kL} M_{D'}, \tag{2.19}$$

where k is the curvature scale or *warp factor* associated with the negative cosmological constants of the five dimensional spacetime model, and $M_{D'}$ is the true Planck scale for one extra spatial dimension, i.e., $D^{'} = 3 + 1$. The effective Planck scale M_P is related to the $M_{D'}$ as

$$M_P^2 = \frac{M_{D'}^3}{k}(1 - e^{-2kL}). \tag{2.20}$$

In RS type I models, gravity is strongly attractive at the hidden brane and gravitons can propagate through the extra dimension, which is bounded by the visible brane. The size of the extra dimension or the separation between the two branes, is small as compared to that described in the ADD model. The difference between the gravitational and electroweak scales depends exponentially on the size of the extra dimension; hence, the

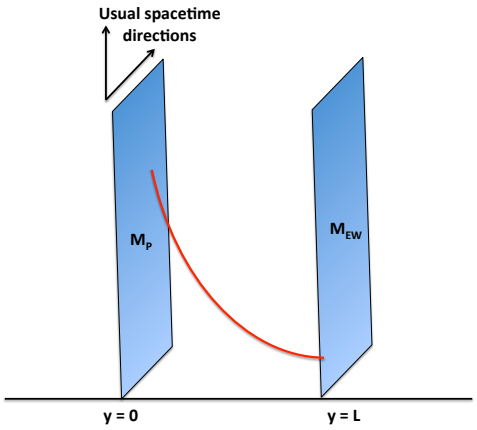

Figure 2.1: Two (3+1)-spacetime branes embedded in a five dimensional spacetime. The red line shows an exponential relation between the two branes.

large difference between the two scales is generated even for a very small size of the extra dimension.

In RS type II models, the visible brane is moved at an infinite distance away from the hidden brane in the extra dimension. Therefore only one brane is effectively used. RS type II models do not yield low scale gravity and microscopic black hole production is only possible in RS type I models.

Both the RS type I and ADD models can explain low scale gravity for the extra dimensional scenarios and predict production of microscopic black holes at the LHC. In this thesis, the ADD types of models have been considered, which are well studied and simulated for the *pp* collisions at the LHC. Therefore, the theoretical and experimental aspects of the production, nature and decay of extra dimensional microscopic black holes will be described in the light of models with large extra dimensions.

2.4 Microscopic Black Hole Physics

In this section, a review of microscopic black holes will be given in the context of the theory of large extra dimensions. In high energy particle collisions, the criteria for their production will be discussed with the necessary boundary conditions along with their properties once they are produced. Higher dimensional microscopic black holes are short-lived and decay in the detectors by emitting mainly SM particles in form of Hawking radiation [23] on the brane or by emitting non-SM particles (e.g. gravitons) into the bulk resulting in missing energy on the brane. The Hawking emission is always dominant because of a higher number of degrees of freedom available for the SM particles. Among SM particles quarks and gluon carry most of degrees of freedom, which lead to the production of a large number of hadronic jets in the detector. Therefore, in high energy particle collisions at the LHC, microscopic black hole signatures such as high p_T multijet final states with high multiplicities are expected. Since the Hawking emission depends on the number of extra spatial dimensions, it is therefore important to study the lifetime, cross section and temperature of microscopic black holes as a function of the number of extra dimensions. In the last section 2.5, the feasibility of their detection with the current experiments at the LHC will be discussed.

2.4.1 Production of Black Holes

In the models with large extra dimensions, strong gravity can be observed at the scale of quantum gravity at which gravitational interactions reach the same order of magnitude as the electroweak interactions. When the magnitude of the true Planck scale M_D is of the order of few TeV, strong gravity in collider experiments can be observed. For $E > M_D$, the production of heavy and extended (having extra dimensions) objects like microscopic

black holes becomes possible.

The two types of models with extra dimensions predict the production of black holes in collider experiments on the brane. Assuming two highly energetic colliding particles form a spherically symmetric black hole, then all the mass would be compressed inside the black hole horizon. The gravitational radius that holds all the compressed mass within it is called the Schwarzschild radius. A boundary around the Schwarzschild radius beyond which the escape velocity from the surface would exceed the velocity of light due to the strong gravitational pull of the compressed mass, is called an event horizon. For a non-rotating spherical black hole, the surface at the Schwarzschild radius acts as the event horizon with radius $r_H(E)$, which is a function of the centre of mass energy E of the colliding particles.

Beside the $E > M_D$ condition, there is also a necessary requirement on the impact parameter (b) of two colliding particles for the production of microscopic black holes. The two colliding particles with $b < r_H(E)$ will form a black hole and disappear forever behind the event horizon according to Thorne's Hoop Conjecture [24]. On the other hand, if $b > r_H(E)$ for energy $E > M_D$, only gravitational elastic and inelastic scattering processes occur, without the formation of black holes.

As an outcome of strong gravity, the microscopic black hole is also a higher dimensional object which extends outside the brane. If the event horizon radius is assumed to be smaller than the size of the extra dimensions $\mathscr{R}$, this type of black hole (spherically symmetric and higher dimensional) may live in a spacetime with $(4 + n)$ non-compact dimensions. By solving Einstein's equation for $D = n + 4$ dimensions for a non-spinning and non-charged black hole, the event horizon radius can be written [25] as

$$r_H = \frac{1}{M_D}\left(\frac{M_{BH}}{M_D}\right)^{\frac{1}{n+1}}\left(\frac{8\Gamma(\frac{n+3}{2})}{(n+2)\sqrt{\pi}^{n+1}}\right)^{\frac{1}{n+1}}, \tag{2.21}$$

n	2	3	4	5	6	7
$x_{\min}$	8.0	9.5	10.4	10.9	11.1	11.2

Table 2.1: $x_{\min} = E/M_D$ as a function of n extra dimensions.

where Γ is the complete Gamma function. The horizon radius depends on the black hole mass M_{BH} with an extra dimensional power law. The linear dependence in $4D$ can easily be restored for $n = 0$. The fundamental Planck scale M_D in the denominator will play an important role in deciding the threshold to create black holes in the high energy collisions.

These black holes may be produced if the Compton wavelength $\lambda_C = 4\pi/E$ of a colliding particle of energy $E/2$ is smaller than the Schwarzchild radius $r_H(E)$ [26]. From equation (2.21), we can write this condition as

$$\frac{4\pi}{E} < \frac{1}{M_D}\left(\frac{E}{M_D}\right)^{\frac{1}{n+1}}\left(\frac{8\Gamma(\frac{n+3}{2})}{(n+2)\sqrt{\pi}^{n+1}}\right)^{\frac{1}{n+1}}. \tag{2.22}$$

From this inequality, it is convenient to define the ratio $x_{\min} = E/M_D$ for the production of black holes for different number of extra dimensions, as shown in Table 2.1. Furthermore, it can be established from equation (2.22) that $E \geq M_D$ is the requirement to produce black holes in the high energy collisions at the LHC.

There is no complete and consistent theory of quantum gravity that can describe the exact conditions for the production of higher dimensional black holes, and the amount of energy absorbed by them, during high energy collisions in a strong gravitational background. The approach which is commonly used to describe the formation of black holes is the Aichelburg-Sexl model [27]. The model is built in four dimensional gravitational theory in the context of general relativity. In this approach, two shock fronts are considered to collide at a central point to form a non-linear and curved region. The uncertainties of quantum particles are neglected by assum-

ing boosting of shock waves to thin fronts because the particles with energy $E > M_D$ have position uncertainty smaller than their horizon radius. The collision of two shock waves can form a closed trapped surface (a two-dimensional closed surface on which outward-pointing light rays are converging towards the surface) or an apparent horizon (a closed trapped surface with no convergence of light rays towards the surface). The latter case is the creation of black hole in which the apparent horizon coincides with the event horizon or lies inside it [28]. The creation of a black hole is therefore a boundary value problem. For $D = 4$ and a perfect head on collision ($b = 0$), by using analytical approach, an apparent horizon is formed with an area $32\pi\rho^2$ [29], where ρ is the energy of the colliding particle ($E = 2\rho$). This defines a lower bound on the area of the event horizon A_H and the mass of black hole M_{BH}, which can be written as

$$A_H = 4\pi {r_H}^2 \geq 32\pi\rho^2 \Rightarrow M_{BH} \equiv \frac{r_H}{2} \geq \frac{1}{\sqrt{2}}(2\rho). \tag{2.23}$$

From this equation[4], the black hole can absorb 71% of the initial energy E. In other calculations it is shown that the black hole can absorb more than 80% of the initial colliding energy [30, 31]. For a higher dimensional regime and perfect head on collision, the above equation (2.23) can be extended [32] as

$$M_{BH} \geq [0.71 \text{ (for } D = 4) \text{ to } 0.58 \text{ (for } D = 11)](2\rho). \tag{2.24}$$

Hence, with the increase in dimensionality, the amount of initial energy absorbed decreases and smaller black holes are produced.

2.4.2 Production Cross Section of Black Holes

A microscopic black hole is treated as a quasi-stable state that is produced and decays semiclassically. At high energies, black hole production has a

[4] Equation (2.23) uses natural units, i.e. , $\hbar = c = G_4 = 1$, where G_4 is the Newton's gravitational constant in four dimensions.

good classical description instead of quantum mechanical treatment [26,33]. The simple form of the classical geometric cross section is given as

$$\sigma_{\text{production}} \simeq \pi r_H^2. \tag{2.25}$$

The Schwarzschild radius (r_H) corresponding to the black hole mass M_{BH} depends on M_D and number of extra dimensions n as shown in equation (2.21). For highly energetic collisions and $b \lesssim r_H$, the cross section depends on the critical value of impact parameter, resulting in a range of black hole masses for a given centre of mass energy E. For a geometrical interpretation of the cross section, the average black hole mass is assumed to be on the order of the centre of mass energy, i.e., $\langle M_{BH} \rangle \approx E$. By using this assumption, and ignoring charge, spin and finite particle size for a microscopic black hole, the production cross section can be expressed in terms of the centre of mass energy of the collision (E) by using equation (2.25) and (2.21) as

$$\sigma_{\text{production}} \propto \pi r_H^2 \approx \frac{1}{M_D^2} \left(\frac{E}{M_D} \right)^{2/(n+1)}. \tag{2.26}$$

This type of unique dependence on energy E in the production cross section is not observed in any of the SM or beyond SM processes. The above equation (2.26) is valid for two elementary and non-composite particles such as partons. In pp collisions, by summing over all the possible pairs of partons and ignoring radiative energy losses, the expression for cross section in terms of parton distribution functions (PDFs) $f_i(x)$ takes the final form [26, 33]

$$\sigma_{\text{production}}^{pp \to \text{BH}} = \sum_{ij} \int_{\tau_m}^{1} d\tau \int_{\tau}^{1} \frac{dx}{x} f_i(x) f_j \left(\frac{\tau}{x} \right) \sigma_{\text{production}}^{ij \to \text{BH}}, \tag{2.27}$$

where i and j are the two colliding partons, x is the parton-momentum fraction, $\tau = \sqrt{x_i x_j}$ is the parton-parton centre of mass energy fraction

and τ_m is the minimum parton-parton centre of mass energy fraction for the black hole production. The cross section gets a considerable enhancement by considering all pairs of partons. Overall, the value of cross section falls off rapidly with the centre of mass energy of pp collisions because of the nature of the PDFs.

The expression for the classical cross section shown in equation (2.25) does not take into account the effects of angular momentum, gauge charges, finite sizes of the incoming particles, non-trapped energy and minimum mass cutoff of the black hole. Many attempts have therefore been made to improve the value of the classical cross section. For example, the effects of angular momentum have been incorporated in a heuristic way in some studies [34–36] with some limited successes. The effects of non-trapped energy and minimum black hole mass cutoff have been studied in Ref. [35–37]. In Ref. [37], different models [34–36] have been compared for possible corrections in the cross section, and it has been shown that the large differences in cross section between the models do not translate into large differences in the limits on M_D. These limits are useful to compare with experimental limits, but their accuracy depends on estimates of large uncertainties in the black hole decay. Therefore, it is usually suggested that M_D limits should be extracted from methods other than the direct search for black holes [38].

2.4.3 The Nature of Black Holes

Microscopic black holes with mass far exceeding the fundamental Planck scale, i.e. $M_{BH} \gg M_D$, are well understood in the context of general relativity. This type of black hole is called a thermal black hole. In general, the thermal black holes are expected to go through different stages during their lifetime [26] as following:

i. The balding phase: at this initial stage, the black hole is highly asymmetric. It emits mainly gravitational radiations and sheds all the quantum numbers and multipole moments apart from those determined by its mass M_{BH}, charge Q and angular momentum J. The energy emission is dominated by gravitational radiation and remains mainly invisible on the brane.

ii. The spin-down phase: the black hole starts losing its angular momentum through the emission of Hawking radiation.

iii. The Schwarzschild phase: the black hole is no longer rotating and continues to lose its mass in the form of Hawking radiation.

iv. The Planck phase: the black hole mass M_{BH} approaches the true Planck scale M_D and then becomes a quantum object. At this stage, its properties are described by a quantum theory of gravity. Either it completely evaporates or becomes a stable quantum remnant.

The non-vanishing temperature of black holes allow them to emit Hawking radiation. The temperature as a function of the number of extra dimensions n and the Schwarzschild radius r_H can be written [39] as

$$T_H = \frac{(n+1)}{4\pi r_H}, \quad \text{for } M_{BH} \gg M_D. \tag{2.28}$$

The above expression implies that higher dimensional black holes at fixed radii are hotter. This property distinguishes microscopic black holes from the large astrophysical black holes that carry an extremely low temperature and the majority of primordial black holes that are characterized by higher temperature [40].

As a consequence of the emission of Hawking radiation, the lifetime of microscopic black holes remains finite except for the case of stable

remnant. The higher-dimensional black holes have the lifetime [39]

$$\tau_{n+4} \sim \frac{1}{M_D}\left(\frac{M_{BH}}{M_D}\right)^{\frac{n+3}{n+1}}, \quad \text{for } M_{BH} \gg M_D. \tag{2.29}$$

By using equation (2.29), the lifetime of a black hole with $M_{BH} = 5$ TeV and $M_D = 1$ TeV is estimated to be on the order of 10^{-26} s for $n = 1$ to $n = 7$ extra-dimensions. Black holes produced in high energy collisions would decay through Hawking radiation. Therefore, the knowledge of the Hawking radiation spectrum is of great importance in the study of microscopic black holes. Classically, nothing is allowed to escape from the event horizon, which is why the phenomena of the emission of Hawking radiation is a quantum mechanical process similar to black body emission.

The scenario of emission of radiation from black holes can be realised by considering a virtual pair of particles near its event horizon. The virtual particle-antiparticle pairs may be produced in the vacuum by the fluctuations of electromagnetic and gravitational fields. The two particles in a pair appear to move apart and then back together, and eventually annihilate each other. If this virtual pair appears near the horizon of a black hole, then one of them may be pulled into the black hole leaving the other particle free. The virtual particle antiparticle pair becomes real when it is boosted by the gravitational energy of black hole. The particle that moves away from the black hole takes away some fraction of the black hole mass. For an observer far away from the black hole, the black hole appears to emit a particle by loosing its mass and it continues to evaporate until the whole black hole mass disappears by emitting mainly SM particles. There is a gravitational potential barrier that reflects some particles back into the event horizon and allows others to escape from the vicinity of the black hole. The transmission or absorption probability of a black hole is known as the *greybody factor*. This factor depends on the nature

of emitted particles (spin s, charge, energy ω, angular momentum numbers l,m) and spacetime properties (number of extra dimensions n, Planck scale M_D). Therefore, the Hawking radiation spectrum is the valuable source of information on the properties of the emitted particles and the gravitational background [40].

Another important feature of the higher dimensional microscopic black holes is the emission of particles both in the bulk and on the brane. The particles that are allowed to propagate in extra space dimensions and carry non-SM quantum numbers, like gravitons, are also emitted in the bulk. The brane observer cannot see the bulk particles and thus they are treated as missing energy and missing momentum on the brane. On the other hand, the black hole emits a variety of four dimensional SM particles on the brane, like fermions, and gauge and Higgs bosons. It is also important to mention that the bulk particles see a $(4 + n)$ gravitational background whereas the brane particles only see a four dimensional gravitational background [40].

2.4.4 Decay of Black Holes

The Hawking radiation from black hole decay is emitted in two different phases during the decay of black holes, the spin down phase and the Schwarzschild phase. To study the emission of Hawking radiation, only the brane localized modes are considered because they are directly visible to a brane observer.

Brane localised Schwarzschild Phase

This phase can be explained through greybody factors $\mathscr{A}(\omega)$ for a spherically symmetric and neutral (with no global charge) black hole that lost all of its angular momentum. The greybody factor will have different values for different spins of particles ($s = 0, 1/2, 1$). The combined "master" equa-

tion of motion for all species of particles has been derived in Ref. [41, 42]. For this equation, the factorised ansatz for the wave function in spherical coordinates (r, θ, ϕ) of the field can be written as

$$\psi_s = e^{-i\omega t} e^{im\phi} \Delta^{-s} R_s(r) S_{sl}^m(\theta), \tag{2.30}$$

where $\Delta \equiv r^2 \left[1 - \left(\frac{r_H}{r}\right)^{n+1}\right]$ is a function of the Schwarzschild radius r_H and the number of extra spatial dimensions n. $R_s(r)$ is the pure radial function for a particle of spin s and $S_{sl}^m(\theta)$ are the spherical harmonics (for spin s and angular momentum numbers l and m). By using Newman-Penrose method [43], decoupled equations can be obtained for the radial function $R_s(r)$ and the spin-weighted spherical harmonics $S_{sl}^m(\theta)$. We concentrate only on the radial part because it is directly related to the greybody factor.

There are two types of methods for obtaining solutions for the radial equation, analytical and numerical. In the analytical approach [41, 42], there are three steps to reach the final solution. First, the equation of motion is solved in the near-horizon regime ($r \backsimeq r_H$). Second, the equation of motion is solved in the far-field regime ($r \gg r_H$). In the the final step, the two asymptotic solutions are matched in an intermediate regime in order to make sure the solutions are continuous over the whole range of radius. Once the solution is obtained, the absorption probability can be written as a function of emitted energy ω as

$$|\mathscr{A}(\omega)|^2 = 1 - |\mathscr{R}(\omega)|^2 \equiv \frac{\mathscr{F}_{horizon}}{\mathscr{F}_{infinity}}, \tag{2.31}$$

where $\mathscr{R}(\omega)$ is the reflection coefficient and $\mathscr{F}$ is the energy flux towards the black hole.

In the microscopic black hole decay, the number of degrees of freedom (dof) play an important role in determining the probability of emission for different particles. The dof is defined [44] as

$$\text{dof} = n_Q \times n_S \times n_F \times n_C, \tag{2.32}$$

Particle Type	Charge State[5]	Spin State	Flavour State	Colour State	dof
Quarks	2	2	6	3	72
Charged leptons	2	2	3		12
Neutrinos[6]	2	1	3		6
Gluons	1	2		8	16
Photon	1	2			2
Z boson	1	3			3
W bosons	2	3			6
Higgs boson	1				1

Table 2.2: Number of degrees of freedom (dof) of the Standard Model particles [44].

where n_Q, n_S, n_F and n_F are the number of charge, spin, flavour and colour states, respectively. Since the black holes mainly decay into SM dof, therefore only SM dof are taken into account, which are shown in Table 2.2 [44].

For a given degree of freedom (z), the absorption cross section for an extra dimensional black hole can be written in terms of absorption probability [45] as

$$\sigma_{abs}^{(z)}(\omega) = \sum_{l} \frac{2^n \pi^{(n+1)/2} \Gamma[(n+1)/2)]}{n! \omega^{n+2}} \frac{(2l+n+1)(l+n)!}{l!} |\mathscr{A}^{(z)}(\omega)|^2. \tag{2.33}$$

The absorption cross section is also sensitive to the particle spin ($s = 0$, 1/2 and 1) and the spacetime properties because of its strong dependence on the greybody factor. The emission rate (number of particles emitted per unit time), in terms of $\sigma_{abs}^{(z)}(\omega)$, is given [23, 46] by

$$\frac{dN^{(z)}(\omega)}{dt} = \frac{1}{(2\pi)^{n+3}} \int \frac{\sigma_{abs}^{(z)}(\omega)}{\exp(\omega/T_H) \pm 1} d^{n+3}p, \tag{2.34}$$

where T_H is the Hawking temperature given in equation (2.28), $p = (\omega, \vec{p})$

[5] If a particle and its antiparticle are different then charge state is two, otherwise one.

[6] Dirac neutrinos have six dof, whereas in case of majorana neutrinos there are three dof because their particle and antiparticle are the same.

D	4	5	6	7	8	9	10	11
Higgs boson	1.00	1.00	1.00	1.00	1.00	1.00	1.00	1.00
Fermions	0.37	0.70	0.77	0.78	0.76	0.74	0.73	0.71
Guage bosons	0.11	0.45	0.69	0.83	0.91	0.96	0.99	1.01

Table 2.3: Fractional emission rates per degree of freedom, normalised to the scalar field, for the Standard Model particles [47].

is the energy-momentum 4-vector, the spin statistics factor has $+1$ for fermions and -1 for bosons in the denominator. By using equation (2.34) with the knowledge of greybody factor, the fractional emission rate or the relative emissivity (ϵ) for different types of particle can be calculated. For non-rotating black holes, the emissivities for different SM particles are calculated in Ref. [47], which are shown for different spacetime dimensions D in Table 2.3. Finally, the probability of emission (P_i) for a particle type (i) is given [44] by

$$P_i = \frac{\epsilon_i \times \mathrm{dof}_i}{\sum_j \epsilon_j \times \mathrm{dof}_j}, \tag{2.35}$$

where ϵ_i and dof_i are the emissivity and the number of degrees of freedom of particle i and the index j in the denominator runs over all the possible particle types. The probabilities of emission for all the SM fields, for different spacetime dimensions D, are shown in Table 2.3 [44]. By talking gravitons and all the SM fields into account, it can be concluded that the multidimensional black hole decay in the detector produces about 74% hadronic energy, 9% missing energy, 8% electroweak bosons, 6% charged leptons, 2% photons, and 1% Higgs bosons [44].

The Spin Down Phase on the Brane

For the spin down phase, the most generic situation for the creation of the black hole by a non-head-on collision is considered when the black hole has a non-vanishing angular momentum. Assuming the extra dimensional black

D	4	5	6	7	8	9	10	11
Quarks	0.71	0.66	0.62	0.59	0.57	0.55	0.53	0.51
Charged leptons	0.12	0.11	0.10	0.10	0.10	0.09	0.09	0.09
Neutrinos	0.06	0.06	0.05	0.05	0.05	0.05	0.04	0.04
Gluons	0.05	0.09	0.12	0.14	0.15	0.16	0.16	0.16
Photon	0.01	0.01	0.02	0.02	0.02	0.02	0.02	0.02
EW bosons	0.03	0.05	0.07	0.08	0.09	0.09	0.09	0.09
Higgs boson	0.03	0.01	0.01	0.01	0.01	0.01	0.01	0.01

Table 2.4: Probability of emission of the Standard Model particles [44].

hole produced in this situation has an angular momentum only along an axis of the three dimensional space. In this case, the absorption probability $|\mathscr{A}(\omega)|^2$ also depends on angular momentum parameter besides the particle spin and the spacetime properties. For a given value of n, the emission rate increases with the increase in angular momentum parameter [34].

There is another important feature of the rotation spectra of the black holes during the spin down phase. The emitted particles during the spin down phase have non-trivial angular momentum distribution because this phase has a preferred axis for the brane localised emission, the rotation axis of the black hole [40].

Emission in the Bulk

The detection of the higher dimensional black holes can greatly be facilitated if a major part of Hawking emission is channelled into brane fields. Any emission into the bulk will be interpreted as missing energy by the brane observer. The bulk emission is sensitive to the number of extra space-like dimensions n, for example, the bulk emission rate for the gravitons [48–50] is greatly enhanced as n increase. Most of these studies have been performed for the Schwarzschild phase.

When both the brane and the bulk channels are available, it is important to investigate whether the higher dimensional black holes prefer to decay into the brane or the bulk. In Ref. [48–50], the bulk to the brane ratio has been shown for the total emissivity. These studies conclude that the bulk to the brane ratio is less than unity and the brane channel remains the most dominant and preferred channel for the intermediate values of n whereas the bulk contribution becomes significantly important for high values of n, e.g., the bulk to the brane ratio becomes 0.93 for $n = 7$.

2.5 Microscopic Black Holes at the LHC

In this section, the feasibility of measuring different observables, e.g., cross section, temperature and mass of the microscopic black holes at the LHC will briefly be described in the context of models with large extra dimensions. A quick illustration of the assumptions for these observables and possible sources of uncertainties in them will be given, in order to realise the accuracy in the measurement of signals for the higher dimensional black holes at the LHC.

2.5.1 Cross Section and Extra Dimensions

The LHC is designed to collide particles with a maximum centre of mass energy of 14 TeV. Even this maximum energy would never be sufficient to produce a black hole in four spacetime dimensions. For example, an estimate of the Schwarzschild radius for a black hole of mass $M_{BH} = 5$ TeV from equation (2.21), for the $D = 4$ case with corresponding classical value of $M_P \simeq 10^{19}$ GeV, is 10^{-35} fm [40], which translates to a very tiny cross section from equation (2.25). On the other hand, if we consider a few TeV extra dimensional Planck scale M_D, for the same type of black hole, then the Schwarzschild radius as a function of the number of extra dimensions would give some measurable estimate for the cross section at the LHC.

Therefore, it is believed that any black hole observed at the LHC would be embedded in extra space dimensions. In other words, the models with extra dimensions facilitate the observation of microscopic black holes at the LHC.

2.5.2 Hawking Temperature

Classically, for fixed black hole radius the value of the Hawking temperature increases with the number of extra dimensions as described by equation (2.28). For models with large extra dimensions, the black hole would have very high temperature[7] which may be an important features to identify black hole events at the LHC. The Hawking temperature should increase progressively with the evaporation process, but a constant value of temperature may also be assumed because of the fact that a black hole has a very short lifetime.

2.5.3 Measurement of Mass

Measurement of the mass of multidimensional microscopic black holes at the LHC is also a goal of primary importance. In the very high energy collisions of the LHC, the only way to reconstruct the black hole mass is through the energies of final state particles which are emitted as a result of evaporation of the black hole. The weak point of this method is the missing energy, which can greatly be improved by selecting the events having no or very little missing transverse energy, or including missing transverse energy in mass calculations. The next subsection is dedicated to briefly describe the role of missing transverse energy in the mass and cross section of the higher dimensional black holes at the LHC.

[7] A higher dimensional black hole would be hotter as compared to the four dimensional black hole, as shown in equation (2.28).

2.5.4 Missing Energy in Black Hole Searches

During the formation and decay of microscopic black holes at the LHC, missing energy may cause underestimation in the mass and the cross section of higher dimensional black holes. The emission of gravitational radiation during the black hole formation is the largest source of missing energy, which results in the largest uncertainty in the black hole mass and cross section. The gravitational radiation is lost into the bulk and appears as missing energy for the brane observer. The effective black hole mass is lowered even before it begins to be detectable by its Hawking evaporations. Since the black hole cross section is the function of mass, therefore the initial radiation loss could significantly lower the production cross section. During the evaporation process high energy neutrinos are also emitted, which further contribute to the missing energy.

If a black hole evaporates and becomes a stable remnant, another complication may arise in the context of missing energy. The mass of the stable remnant could be of the order of the Planck scale, as discussed in [51]. If this stable remnant is charged and ionizing it may be detected, but a large missing energy may arise in the case of a neutral and non-detectable remnant.

There is another possibility causing large missing energy, where the black hole leaves the brane, as discussed in [44]. In this scenario, graviton emission into the bulk can give a sufficient recoil to the black hole to leave the brane and move to the bulk. Normally, black holes are not expected to move to the bulk. It is more likely they will have charge, colour or lepton/baryon number in order to stick them to the brane. But, if there is no symmetry available, the recoil produced by the emission of higher dimensional gravitons will cause the black hole to leave the brane. There might be two possible situations for graviton emission. Firstly, a newly

formed black hole emits higher dimensional gravitons and disappears from the brane without showing any visible signature in the form of Hawking emission. This type of black hole decay remains undetectable and nothing can be done to make it detectable. Secondly, higher dimensional gravitons are emitted during Hawking evaporation resulting in the termination of Hawking radiation as soon as the black hole leaves the brane. This situation may contribute large missing energy during the black hole decay and produce large uncertainties in calculations of the black hole mass and cross section.

With all the possibilities of missing energy during the formation and decay of black holes, it may be difficult to detect microscopic black holes at the LHC with a high confidence level. Furthermore, the parton energy involved in the black hole formation is unknown. Therefore, the fundamental Planck scale and the number of extra dimensions determined from the black hole searches can have large uncertainties. All that can be measured is a threshold for production. The M_D values measured from black hole searches may vary largely from model to model. Therefore, it is more reasonable to rely on M_D limits which are measured from other quantum gravity analysis. The current limits on M_D will be presented in the next subsection.

2.5.5 Current Limits on M_D

The ATLAS and CMS experiments at the LHC have searched for extra dimensions and microscopic black holes. These searches put different limits on the fundamental Planck scale, which are largely model-dependent. Since all the models are still on hypothetical grounds, for M_D limits it is better to rely on other searches for KK resonances in the current scenario. The most recent limits on M_D, in direct graviton emission searches, have been presented in Ref. [38] for LEP (ALEPH and DELPHI experiments),

n	M_D [TeV]						
	Mono-photon		Mono-jet	Mono-photon		Mono-jet	
	LEP	CDF	D0	ATLAS	CMS	ATLAS	CMS
2	1.60	1.40	0.884	1.93		4.17	4.08
3	1.20	1.15	0.864	1.83	1.73	3.32	3.24
4	0.94	1.04	0.836	1.86	1.67	2.89	2.81
5	0.77	0.98	0.820	1.89	1.84	2.66	2.52
6	0.66	0.94	0.797		1.64	2.51	2.38
7			0.797				
8			0.778				

Table 2.5: Lower limits on M_D at the 95% confidence level [38].

Tevatron (CDF and D0 experiments) and LHC (CMS and ATLAS experiments) collider experiments. Current lower limits on M_D are shown in Table 2.5 with 95% confidence level. In Table 2.5, both ATLAS and CMS results correspond to graviton searches in mono-jet plus missing transverse momentum and mono-photon plus missing transverse momentum in the final states.

2.5.6 Decay of Black Holes at the LHC

It was explained in section 2.4.4 that the major black hole signature in the detector is the hadronic energy. The hadronisation of quarks and gluons emitted by the decay of black holes can produce many hadrons in the form of narrow cones called jets with high transverse momenta. Most of the multijet events in high energy pp collisions, however, are produced by QCD and are the main background to the potential multijet final states produced by black holes.

There are some properties of black hole multijet signals which could differentiate them from QCD multijet background. In high energy pp col-

lisions at the LHC, the most dominant QCD process is the production of dijets, where two back-to-back jets are produced with high transverse momenta. On the other hand, black holes are expected to produce high jet multiplicities. Furthermore, the decays of black holes are expected to produce a range of jet multiplicities instead of being biased towards any particular multiplicity. The QCD events with high transverse momenta are expected to become rare as the centre of mass energy of the collisions increases, whereas the production cross section for black holes increases with increasing centre of mass energy, as shown by equation 2.26. It is shown in different studies [26, 52, 53] that QCD dijets could be suppressed in the case of black hole formation. As a result, multijet events produced by the decays of black holes at the LHC are differentiable from QCD backgrounds. Therefore, this study is only focussed on the multijet final states for black hole searches in the ATLAS 2012 data.

The multijet final state data are used to calculate model-independent exclusion limits on the production of new physics. To set model-dependent exclusion limits, several black hole event generators, e.g., CHARYBDIS [54], CATFISH [55], BLACKMAX [56] and QBH [57], have been developed to model the formation of different types of black holes at the LHC. CHARYBDIS is the most widely used black hole generator, using PYTHIA [58] or HERWIG [59] simulations to handle all the QCD interactions, hadronisation and secondary decays. In this study, the data samples produced from the CHARYBDIS generator are used to set model-dependent exclusion limits on the production of black holes.

Chapter 3

The ATLAS Detector at the Large Hadron Collider

3.1 Introduction

The analysis described in this thesis has been performed using pp collisions collected by ATLAS in 2012. ATLAS is one of the general purpose detectors at the LHC. In this chapter, a brief introduction to the ATLAS detector is given by describing its major components. The types of information used in the analyses are mostly based on calorimeter measurements. The important sub detectors of ATLAS will be described in detail.

3.2 The Large Hadron Collider

The LHC is the world's largest particle accelerator operating at the highest collider energy ever achieved in an accelerator. It is a ring 27 kilometres in circumference, 100 metres beneath the French-Swiss border near Geneva, Switzerland. It is designed to collide mainly proton-proton (pp) beams, moving in opposite directions, with 14 TeV centre of mass energy and a luminosity of 10^{34} $\mathrm{cm}^{-2}\mathrm{s}^{-1}$. Inside the LHC, there are eight accelerating cavities and each one of them provides a strong electric field of about 5 MV/m used to accelerate the beams. It also contains 1232 superconducting main dipole magnets (to bend the beams), providing a

total field of 8.33 T, and 392 super conducting quadrupole magnets (to focus the beams), providing a total field of 6.86 T. The LHC is expected to shed light on some of the most fundamental questions of physics, the understanding of basic laws through which nature governs this universe. In the exciting year of 2012, the LHC not only successfully operated at 8 TeV centre of mass energy but also accomplished one of its major goals, the discovery of the Higgs boson [14, 15].

There are four major detectors on the LHC ring: ATLAS, CMS, ALICE (dedicated to heavy ion physics) and LHCb (dedicated to b-physics). ATLAS (A Toroidal LHC ApparatuS) and CMS (Compact Muon Solenoid) are the two general purpose detectors that have been built to probe pp collisions mainly. The analysis described in the next chapter is performed with the ATLAS 2012 data from pp collisions. ATLAS has recorded an integrated luminosity of 21.7 fb^{-1} in 2012, as shown in Figure 3.1.

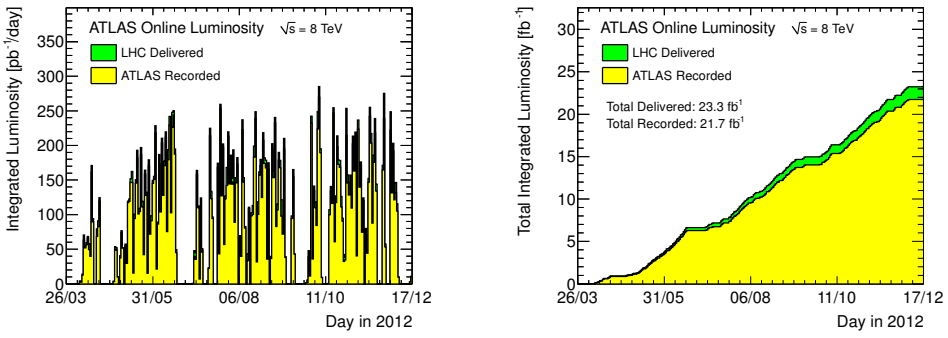

Figure 3.1: The maximum instantaneous luminosity (left) and the cumulative integrated luminosity (right) delivered by the LHC per day and recorded by ATLAS per day for pp collisions at 8 TeV centre of mass energy during the stable beams in 2012 [60].

3.3 The ATLAS Detector

The ATLAS detector [61] is shown in Figure 3.2. The centre of the detector is called the nominal interaction point (IP) and is the origin of the

coordinate system of the ATLAS detector. The beam axis is defined as the z-axis and the x-y plane is considered as the plane transverse to the beam axis. The positive x-axis is defined as pointing from the interaction point to the centre of the LHC ring and the positive y-axis is defined as pointing upwards.

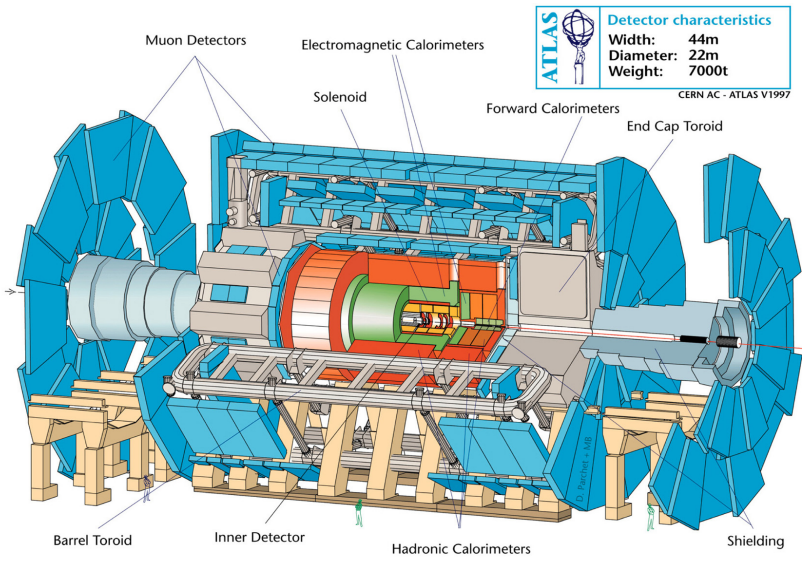

Figure 3.2: Layout of the full ATLAS detector [62].

The azimuthal angle ϕ is measured around the beam axis, and the polar angle θ from the positive beam axis. On the basis of the polar angle one can define pseudorapidity as $\eta = -\ln \tan(\theta/2)$. The ATLAS detector is symmetric in the z-axis and it covers the whole range of ϕ.

The Inner Detector (ID), the Calorimeters and the Muon Spectrometer are the major sub detectors of ATLAS, which will briefly be described in the next sections. The ATLAS detector has a three-level trigger system for the selection of events and event storage for offline analysis, which will be described in the last section of this chapter. Starting from the IP, the detector closest to the IP is the Inner Detector (ID).

3.4 Inner Detector

The ATLAS ID combines high-resolution detectors at the inner radii with continuous tracking elements at the outer radii, capable of recognising primary and secondary vertices in an event. All the ID systems are housed in a central solenoid magnet to provide a field of 2 T to the inner tracking. There are three main components of the ID: the Semiconductor Pixel detectors followed by the Semiconductor Tracker (SCT) and then the Transition Radiation Tracker (TRT) at the outer radius. In the barrel region, they are arranged in concentric cylinders around the beam axis, while the end-cap detectors are mounted on disks perpendicular to the beam axis, as shown in Figure 3.3. Typically for each track, the pixel detector, the SCT and the TRT contribute 3, 4 and 36 tracking measurements, respectively. Hence, the 3 layers of the pixel detector and the 4 layers of the SCT precisely measure the tracks and momentum within the radius of 56 cm, surrounded by a continuous tracking system provided by the TRT.

The pixel and the SCT are called the precision detectors and cover the region of $|\eta| < 2.5$. In the barrel region, the pixel and the SCT layers are segmented in azimuthal (R-ϕ) and axial (z) directions, whereas in the end-cap region, the disks are segmented in azimuthal (R-ϕ) and radial (R) directions. The TRT covers the region of $|\eta| < 2$ and measures in R-ϕ plane only. The pixel sensors have better resolution as compared to the SCT and the TRT to provide precise measurements close to the IP. Each layer of pixels has an accuracy of 10 μm (R-ϕ) and 115 μm (z) in the barrel region, and 10 μm (R-ϕ) and 115 μm (R) in the end-cap region. The 80.4 million pixels on different silicon wafers allow them to identify the positions of different tracks accurately, since the hits on individual pixels are measured. The SCT is less accurate than pixels. Each of its layer has an accuracy of 17 μm (R-ϕ) and 580 μm (z) and 17 μm (R-ϕ) and 580 μm (R) in the

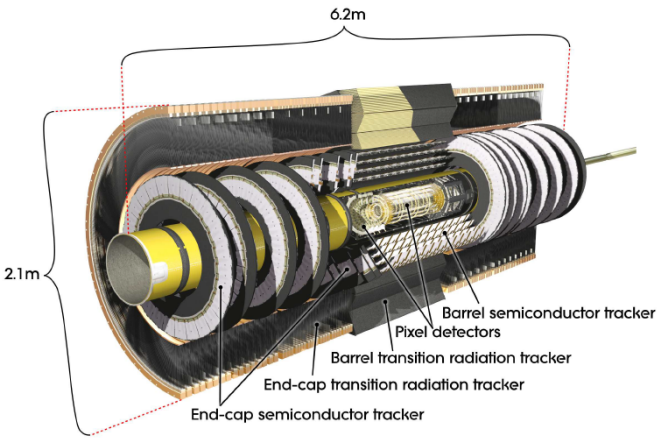

Figure 3.3: Cut-away view of ATLAS Inner Detector (ID) [61].

barrel and end-cap regions, respectively. The TRT is a straw tube detector filled with a xenon-based gas mixture that can also identify electrons, it has a drift-time accuracy of 130 μm per straw.

3.5 Calorimeters

The ATLAS calorimeter system is the set of detectors which is radially outside the ID, providing a full ϕ-symmetry and coverage of $|\eta| < 4.9$ around the beam axis, shown in Figure 3.4. The system has two major types of calorimeters: the electromagnetic and the hadronic calorimeters, both of which are shower-based detectors. The electromagnetic system uses liquid-argon (LAr) as an active detector medium chosen for its intrinsic linear behaviour, stability of response over time and intrinsic radiation-hardness. The hadronic system is based on scintillator tiles with an absorbing medium of steel. The inner-most calorimeters are mounted in three cryostats, one barrel and two end-caps. The barrel cryostat contains the electromagnetic barrel calorimeter, whereas the two end-cap cryostats each contains an electromagnetic end-cap calorimeter (EMEC), a hadronic end-cap calorimeter (HEC), located behind the EMEC, and then a forward calorimeter (FCal) to cover the region closest to the beam.

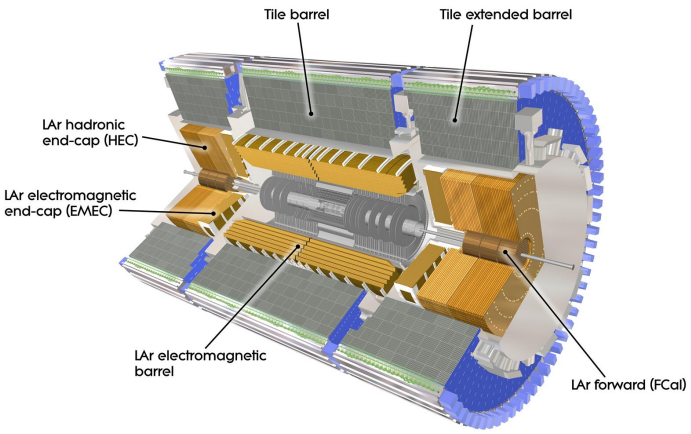

Figure 3.4: The ATLAS calorimeters [61].

3.5.1 Liquid Argon Calorimeter

The electromagnetic calorimeter mainly measures the energies of charged and neutral particles that interact electromagnetically, for example electrons and photons. It consists of several layers of accordion-shaped absorbers of lead and copper electrodes, and LAr between them. For example, a high energy electron interacts with the absorber and forms a shower of low energy electrons, positrons and photons, which passes through LAr and produces more negatively charged electrons and positively charged ions by ionisation. Finally, these ionisation electrons are collected on electrodes and the charge is measured leading to measure energy of the primary electron. The accordion geometry of the LAr calorimeter provides several active layers in the system, three in the precision-measurement region ($1.5 < |\eta| < 2.5$), two in the higher-η region ($2.5 < |\eta| < 3.2$) and two in the overlap region ($1.375 < |\eta| < 1.5$) between the barrel and the EMEC. For $|\eta| < 2.5$, one of the high precision-measurement components with its three layers is shown in Figure 3.5, the first layer contains narrow strips positioned with a 4 mm separation in the η-direction with a very fine granularity of $\Delta\eta \times \Delta\phi = 0.0025 \times 0.01$. The second layer consists of small

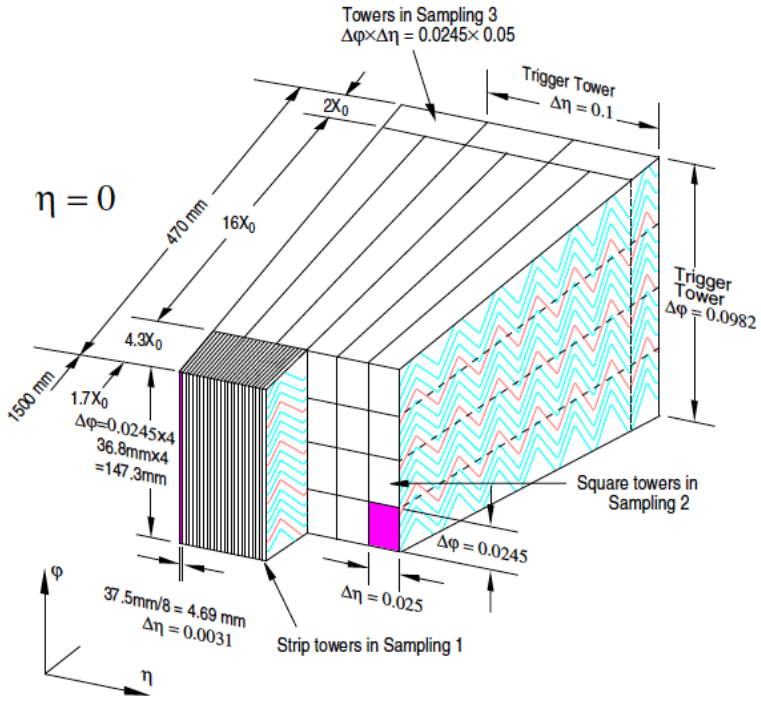

Figure 3.5: Drawing of barrel module of the LAr calorimeter [61].

segments placed into towers with granularity of $\Delta\eta \times \Delta\phi = 0.025 \times 0.025$. The third layer has relatively low precision, as compared to the previous two, with a granularity $\Delta\eta \times \Delta\phi = 0.05 \times 0.025$. Overall, the barrel part of LAr calorimeter provides a coverage of $|\eta| < 1.475$, while the two end-cap components provide $1.375 < |\eta| < 3.2$ coverage.

3.5.2 Hadronic Calorimeter

The tile calorimeter is the next layer to the electromagnetic calorimeter in both the barrel ($|\eta| < 1$) and the end cap regions ($0.8 < |\eta| < 1.8$). The hadronic system also works like the electromagnetic system. In this case, strongly interacting particles interact with the absorbing steel to produce showers of secondary hadrons (for example protons, neutrons and pions) and these showers interact with the scintillating tile material to produce the measurable signals.

The HEC calorimeters are mounted in two wheels per end cap and placed just after the EMEC calorimeter. Each HEC wheel contains two layers and hence there are four HEC layers per end-cap. They cover the $1.5 < |\eta| < 3.2$ region with variable granularity: $\Delta\eta \times \Delta\phi = 0.1 \times 0.1$ for $1.5 < |\eta| < 2.5$ and 0.2×0.2 for the $2.5 < |\eta| < 3.2$ region.

The FCal provides higher electromagnetic and hadronic coverage in the forward region ($3.1 < |\eta| < 4.9$), mounted in each end-cap. It consists of three modules, also containing LAr as a sensitive material. The first one is made up of copper (to optimise electromagnetic interactions), while other two are made up of tungsten (to optimise hadronic interactions).

3.6 Muon Spectrometers

The outermost part of ATLAS detector is the muon spectrometer, designed to detect muons in the pseudorapidity range $|\eta| < 2.7$. The different components of Muon Spectrometer are shown in Figure 3.6. Energetic muons are typically the only detectable particles that can traverse all the calorimeters without being stopped. The muon spectrometer surrounds the calorimeter and measures the muon's path by determining their momenta with a typical resolution of about 10%. It contains thousands of charged particle sensors in the central and end-cap regions in order to perform a precision measurement. The sensors are similar to the straw tubes of the ID, but with larger tube diameters. The large superconducting toroidal coils inside the muon spectrometer produce a magnetic field of 0.5 T in the central region and 1 T in the end-caps regions. The minimum energy for muons to reach the spectrometer is ~ 3 GeV, due to energy loss in the calorimeters.

The precise tracking of muons through the spectrometer is accomplished by CSCs (Cathode Strip Chambers) and MDT (Monitored Drift Tube) chambers. The fast trigger system of the spectrometer consists of

three RPC (Resistive Plate Chamber) stations in the barrel, and three stations of TGCs (Thin Gap Chambers) in the end-cap regions.

The MDT chambers consist of aluminium tubes with a central W-Re wire and a gas mixture of Ar-CO_2, which is filled at an absolute pressure of 3 bars that provides a maximum drift time of approximately 700 ns. The MDT chambers are constructed from 2×4 and 2×3 monolayers of drift tubes for the inner and middle/outer stations, respectively. In the drift chambers, the avalanche of secondary ionisations is being detected, which is proportional to the initial ionisation. The CSCs ($2 < |\eta| < 2.7$), using a mixture of Ar, CO_2 and CF_4 gas, are multiwire proportional chambers with a segmented cathode strip readout providing position measurements from the avalanche formed on the anode wire. The RPC ($|\eta| < 1.05$) is a gaseous detector ($C_2H_2F_4$ gas), constructed without wires from two detector layers and four readout strip panels. It typically provides space and time resolutions of 1 cm and 1 ns, respectively. Finally, the TGCs ($1.05 < |\eta| < 2.4$) are multi-wire proportional chambers. The anode wires and readout strips of these chambers are arranged parallel and orthogonal, respectively, to the MDT wires and provide both the spatial and trigger information.

3.7 Forward Detectors

In addition to the main ATLAS detector systems described in previous sections, there are five smaller sets of detectors to cover the forward region in more detail: the Beam Condition Monitor (BCM), the Minimum Bias Trigger Scintillator (MBTS), the LUminosity measurement using Cerenkov Integrating Detector (LUCID), the Zero Degree Calorimeter (ZDC) and the Absolute Luminosity ALFA detectors at distances 1.84 m, 3.6 m, 17 m, 140 m and 240 m from the IP of ATLAS, respectively. They are symmetric

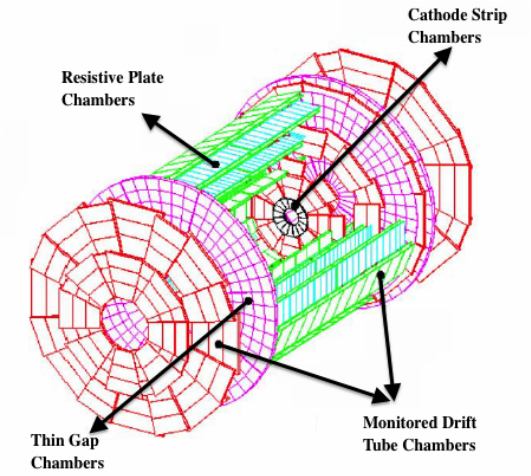

Figure 3.6: Layout of Muon Spectrometer [63].

Forward Detectors	Rapidity Range
BCM	$\|\eta\| \sim 4.2$
MBTS	$2.1 < \|\eta\| < 3.8$
LUCID	$5.6 < \|\eta\| < 5.9$
ZDC	$\|\eta\| > 8.3$
ALFA	$1.06 < \|\eta\| < 13.5$

Table 3.1: Rapidities of forward detectors of ATLAS.

on either side of the IP. Along with the central detectors of ATLAS, the forward detectors provide an additional rapidity coverage in the forward regions as shown in Table 3.1. The forward detectors are closely connected to the luminosity determination in ATLAS, which will briefly be described in the next section.

3.8 Luminosity Measurement

The ATLAS luminosity is measured in inelastic interactions by using different forward detectors and their corresponding counting-algorithms [64]. For a given fraction of bunch crossings (BXs), the number of registered events by a detector are counted according to specific selection criteria, with event selection efficiency (ε), which depends on the specific detector

and the algorithm chosen. The luminosity ($\mathcal{L}$) corresponding to an inelastic cross section (σ_{inel}), for the total number of BXs at the IP (n_b) and the number of inelastic interactions per BX (μ), can be written as

$$\mathcal{L} = \frac{\mu n_b f_r}{\sigma_{inel}} = \frac{\mu_{vis} n_b f_r}{\sigma_{vis}}, \tag{3.1}$$

where f_r is the bunch revolution frequency of the proton bunches. In the above equation, σ_{vis} is the visible cross section related to the average visible interactions per BX (μ_{vis}). The quantity μ_{vis} is the visible quantity seen by a detector which is defined as $\mu_{vis} \equiv \varepsilon\mu$, hence $\sigma_{vis} \equiv \varepsilon\sigma_{inel}$. In the limit $\mu_{vis} \ll 1$, i.e., for a low number of interactions per BX, μ_{vis} is linearly related to the event counting in a detector (N^{vis}) as

$$\sigma_{vis} \approx \frac{N^{vis}}{N_{BX}} \tag{3.2}$$

where N_{BX} are the number of bunch crossings in the same time interval in which N^{vis} are measured. On the other hand, when μ increases, the probability of two or more than two pp interactions in the same BX is no longer negligible, and the relation between μ_{vis} and N^{vis} is not linear anymore. Therefore, for high μ_{vis}, Poisson statistics must be taken into account. The detector algorithms are modified to take the Poisson distribution effects into account for the luminosity calculations.

There is another method for luminosity measurement which neither requires any prior knowledge of cross section nor depends on detector efficiencies. It is known as the van der Meer (vdM) scans method [65]. This technique only depends on the machine parameters and luminosity. The equation for the vdM scans method is written as

$$\mathcal{L} = \frac{n_b f_r n_1 n_2}{2\pi\Sigma_x\Sigma_y}, \tag{3.3}$$

where n_1 and n_2 are the number of protons in two colliding bunches, and Σ_x and Σ_y are the numbers measured from the horizontal and vertical beam

profiles scanned by vdM method. However, this method requires some dedicated runs and special setup to scan the beam profiles.

3.9 Triggers and Data Acquisition

The ATLAS trigger and data acquisition system is a three level online data refinery, and events which pass all the three levels are written out for the offline analysis. The Level-1 (L1) trigger takes information from sub detectors, reduces the event rate to about 75 kHz, and makes an initial selection. For example, it recognises muon p_T from the RPCs and TGCs, and accepts electrons, hadrons and jets from the calorimeter system. The latency of L1 is the time between pp collisions and the time at which the decision of L1 is available for the next level, Level-2 (L2), which is 2.5 μs. Therefore, in this small time L1 decides whether to send this information to L2 or not.

The selection criteria of L2 trigger are based on the information provided by L1, called Regions-of-Interest (RoIs). A RoI information can include various parameters such as p_T, missing transverse energy E_T^{miss}, and the positions of particles in (η,ϕ). Along with the L1-RoI, the L2 trigger uses some additional RoIs with some tighter cuts to process an event in less than 40 ms, and reduces the trigger rate to $\sim$ 3.5 kHz. The Event Filter (EF) is the last stage of the online trigger system, which also uses RoI. The EF reduces the event rate to 200 Hz and processes an event on the order of 1 s, and therefore has an ability to run a complex analysis on the data due to the longer processing time available. The EF is able to filter events with respect to different physics needs, for example events with high p_T jets are used for this analysis. Finally, these events are written out to mass storage for offline analysis.

Chapter 4

Analysis

In this chapter, the search for microscopic black holes in multijet final states for pp collisions with 8 TeV centre of mass energy at the LHC, using the ATLAS 2012 data, is presented. The study is mainly data-driven, but uses corrections derived from MC-simulations (MCs) of QCD. The black hole search in this analysis is based on low-scale gravity models which predict production of non-perturbative gravitational states, such as black holes in high energy particle collisions at the LHC [66].

4.1 Introduction

According to low-scale gravity models, the hierarchy problem (described in chapter 1) can be solved when the fundamental gravitational scale reduces to the order of the electroweak scale. As a consequence, the production of black holes or string balls may occur at the LHC with masses much higher than the fundamental gravitational scale. Once produced, the microscopic black holes at the LHC will act like classical thermal states and quickly decay to a large number of particles (high multiplicity) with high p_T. As discussed in sbusection 2.4.4 and section 2.5 that the black hole decay mainly leads to the production of jets of hadrons in the detector. Therefore, high p_T multijet final states are chosen as a potential signal for the microscopic black holes.

In this study, we look for high multiplicity multijet final states with high p_T. The suitable variable is the scalar sum of jet-p_T ($H_T = \sum p_T$). For different jet multiplicity bins, the shape of the H_T distribution is expected to be the same because initial state radiation (ISR) and final state radiation (FSR) are collinear in nature with respect to the incoming and outgoing partons. The assumption of the H_T shape invariance for the QCD-type events allows us to predict the QCD background for all the jet multiplicities. Since microscopic black holes are expected to decay to high jet multiplicities, the lowest multiplicity case of dijet is therefore chosen as the control region. The most invariant sub-region of H_T with multiplicity of the control region is defined as the normalisation region in the H_T distribution for all the jet multiplicities, where there are no black holes seen. By using the shape invariance assumption and a fit-based technique, the control region fits, along with the appropriate normalisation factors, are applied to jet multiplicities larger than two in order to estimate the background in the signal region. By considering all the possible uncertainties in the signal region, model-independent and model-dependent upper limits are derived for the inclusive jet multiplicities $N \geq 3, 4, ..., 7$. This analysis method is adopted from the previous studies for microscopic black hole searches in the ATLAS [67] and CMS [7–10] collaborations.

4.2 Monte Carlo Simulations

QCD multijet events constitute the dominant background in the search region. PYTHIA8 [68] and HERWIG++ [69] dijet MC samples are used to study the main background. All other background contributions from events such as $t\bar{t}$, Z+jets, W+jets, di-boson (ZZ, WW, WZ) and γ+jets are considerably small and can be ignored [7, 8, 10]. Detailed descriptions of generated dijet samples will be illustrated in next subsection.

All the MC samples are passed through a full simulation of the ATLAS detector [70] using GEANT4 [71]. All the MC simulated data samples used in this analysis have been produced centrally by the ATLAS collaboration for 8 TeV centre of mass energy in order to compare with the ATLAS 2012 data. The MC simulated data is also corrected with respect to pileup effects (described in Appendix E) in the 2012 data. Finally, the MC events are reconstructed and analyzed with the same procedures as used on the data.

4.2.1 QCD Background Samples

The baseline simulated QCD MC samples are generated using PYTHIA8 implementing leading-order (LO) perturbative QCD matrix elements for $2 \to 2$ processes and p_T-ordered parton showers calculated in a leading logarithmic approximation with the ATLAS AU2 tune [72] and the CT10 PDF set [73]. Effectively, these samples are generated for eight different leading jet p_T regions based on their cross sections covering the entire p_T spectrum accessible by the ATLAS detector. The PYTHIA8 MC samples produced for different leading jet p_T slices are named as $JZ0W, JZ1W, ..., JZ7W$, and also called J-samples. At the generator level, events are filtered by the p_T cut corresponding to each J-sample. The efficiency of this cut is known as the filter efficiency. The dataset identifiers (DSIDs), number of events, p_T ranges, cross sections and the filter efficiencies for all the J-samples are given in Table 4.1.

Similarly, HERWIG++ [69] is used to produce another type of baseline QCD events for $2 \to 2$ processes with the EE3 tune [74] and the CTEQ6L1 PDF set [75]. Different slices with corresponding DSIDs based on their cross sections and filter efficiencies are shown in Table 4.2. All the specifications of both the QCD MC events are also compared in Table 4.3.

DSID	Slice	Events	p_T [TeV]	Cross section [fb]	Filter Efficiency
147910	$JZ0W$	1500000	0-0.02	7.3×10^{13}	9.9×10^{-1}
147911	$JZ1W$	1599994	0.02-0.08	7.3×10^{13}	1.3×10^{-4}
147912	$JZ2W$	5999034	0.08-0.2	2.6×10^{10}	4.0×10^{-3}
147913	$JZ3W$	5977254	0.2-0.5	5.4×10^{8}	1.2×10^{-3}
147914	$JZ4W$	5997214	0.5-1.0	6.4×10^{6}	7.1×10^{-4}
147915	$JZ5W$	2996082	1.0-1.5	4.0×10^{4}	2.2×10^{-3}
147916	$JZ6W$	2993651	1.5-2.0	4.2×10^{2}	4.7×10^{-4}
147917	$JZ7W$	2991955	>2.0	4.1×10^{1}	1.5×10^{-2}

Table 4.1: PYTHIA8 dijet MC weighted samples with their corresponding dataset identifier (DSID), name of the sample (Slice), number of events, p_T range, cross section and the efficiency of the kinematic filter at the generator level (Filter Efficiency) are shown.

For both the PYTHIA8 and HERWIG++ MCs, all the J-samples (p_T slices) need to be properly weighted and combined together in order to obtain the whole p_T spectrum. A J-sample can be weighted corresponding to its filter efficiency ϵ_F, cross section σ, weight of each event and the total number of events as following

$$\text{Weight} = \frac{\epsilon_F \times \sigma \times \text{Event weight}}{\text{Number of events}}. \tag{4.1}$$

The above p_T slice weight is applied on an event by event basis for each J-sample. Finally, all the weighted samples are combined to obtain a full p_T distribution in order to compare it with the data distribution.

4.3 Trigger

The selection of a trigger is the starting point of an analysis, as it decides whether to reject an event or keep it for the analysis. Different types of triggers are designed based on objects (electrons, photons, muons, jets, etc.) and physics needs. Since H_T is the key variable of this analysis, and microscopic black hole signals are expected to lie in the high H_T region, a trigger requiring high p_T jets and high H_T would be suitable for this analysis. The

DSID	Slice	Events	Cross section [fb]	Filter Efficiency
159110	$JZ0W$	1399998	1.2×10^{8}	9.9×10^{-1}
159111	$JZ1W$	1399897	3.6×10^{12}	1.4×10^{-3}
159112	$JZ2W$	1399993	1.9×10^{10}	2.6×10^{-3}
159113	$JZ3W$	1399680	3.6×10^{8}	8.5×10^{-4}
159114	$JZ4W$	1399665	4.2×10^{6}	5.4×10^{-4}
159115	$JZ5W$	399490	8.3×10^{4}	5.5×10^{-4}
159116	$JZ6W$	1389845	5.8×10^{3}	2.0×10^{-4}
159117	$JZ7W$	1396932	6.5×10^{2}	5.7×10^{-4}

Table 4.2: HERWIG++ dijet MC weighted samples with their corresponding dataset identifier (DSID), name of the sample (Slice), number of events, cross section and the efficiency of the kinematic filter at the generator level (Filter Efficiency) are shown.

Generator	PYTHIA8	HERWIG++
Process	dijet	dijet
Matrix	PYTHIA8	HERWIG++
Hadronisation	PYTHIA8	HERWIG++
Underlying Event	PYTHIA8	HERWIG++
ATLAS Tune	AU2	EE3
PDF Set	CT10	CETQ6L1

Table 4.3: Matrix element generator, hadronisation generator, underlying event generator, ATLAS tune and parton distribution function (PDF) set is shown for both PYTHIA8 and HERWIG++ QCD dijet MC events.

EF_j170_a4tchad_ht700 trigger fulfills the need of this study by requiring at least one reconstructed hadronic jet of $p_T \geq 170$ GeV and $H_T \geq 700$ GeV at the EF level. The term a4tchad stands for a hadronic (had) jet, which is reconstructed from topological clusters (tc) [76] of calorimeters by using an anti-kt algorithm [77] with a distance parameter $R = 0.4$ (a4) [77, 78]. The trigger efficiency has been studied as a function of the leading jet p_T and H_T with respect to the reference trigger EF_j110_a4tchad. If the main trigger EF_j170_a4tchad_ht700 and the reference trigger EF_j110_a4tchad are represented as "A" and "B", respectively, then the trigger efficiency for a variable is calculated as

$$\text{Trigger Efficiency} = \frac{A \cap B}{B}. \tag{4.2}$$

The trigger efficiency as a function of the leading jet p_T and H_T is shown in Figure 4.1. The correlation between the two variables shows that the fully efficient region of the trigger can be obtained for $H_T > 0.9$ TeV. Furthermore, the trigger efficiency as a function of the leading jet p_T and H_T is shown independent of each other in Figure 4.2, which confirms the H_T threshold for the plateau region. Further details on the trigger efficiency are shown in Appendix B.

4.4 Data Selection

The analysis is performed over the full 2012 data set of pp collisions at $\sqrt{s} = 8$ TeV collected by the ATLAS detector, corresponding to an integrated luminosity of 20.3 fb^{-1}. The data for the year are divided into different data periods, e.g., period-A, period-B, and so on, corresponding to certain time spans of data-taking. A data period consists of the data runs which are made according to the stability of beam conditions at the LHC and detectors collecting the data. A run is further divided into lumi-blocks tagged with numbers called lumi-block numbers (lbn). The length

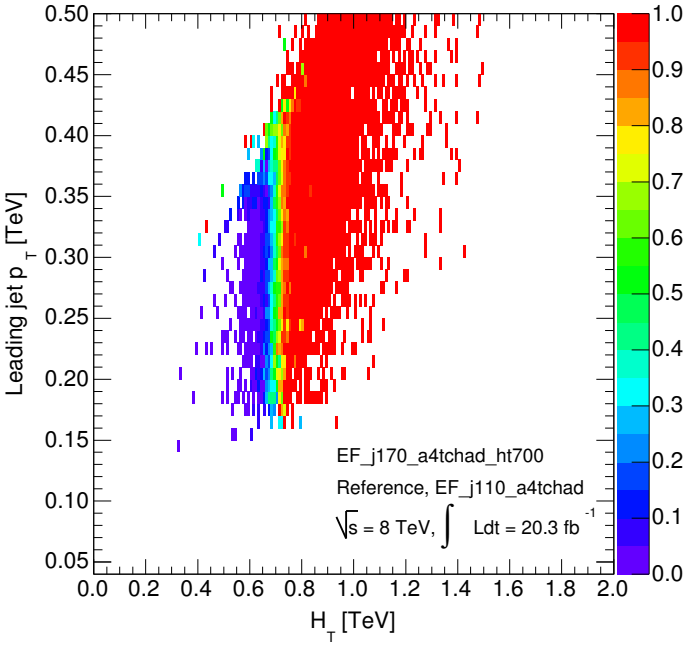

Figure 4.1: The EF_j170_a4tchad_ht700 trigger efficiency versus leading jet p_T and H_T, with respect to the reference EF_j110_a4tchad trigger.

of each lumi-block is on the order of a few minutes and contains several data events. The reason for dividing the data into runs and lumi-blocks is to create a computing ease to deal with the problematic parts of the data with respect to their time stamps while doing the offline analysis. These affected data may arise because of several factors while data-taking. For example, hardware issues in detectors because of the intense radiation environment or any other reason like electronic noise, non-collision and cosmic ray background, etc. can be sources of bad data collected during collisions. In order to discard the bad data, different physics groups in the ATLAS collaboration define good run lists according to their analysis requirements.

The data is then stored in different formats for offline analyses. The ATLAS physics groups make their own short formatted data sets by filtering the raw data according to their physics needs. Furthermore, the data events are filtered using standard event cleaning criteria.

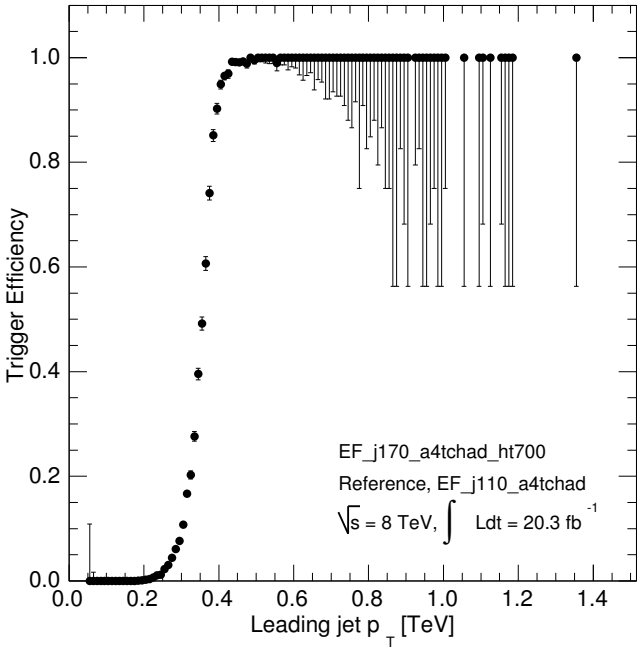

(a) The trigger efficiency as a function of the leading jet p_T.

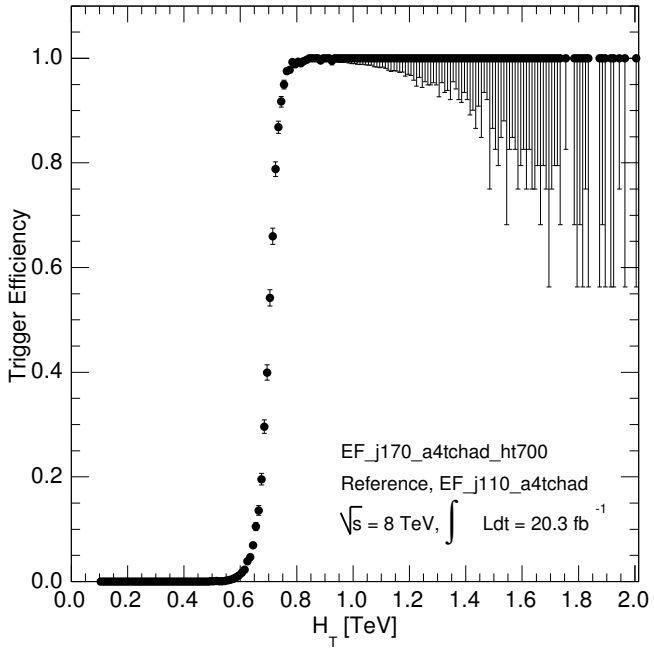

(b) The trigger efficiency as a function of the H_T.

Figure 4.2: The EF_j170_a4tchad_ht700 trigger efficiency with respect to the reference trigger EF_j110_a4tchad.

4.4.1 Event Selection

All the good runs and lumi-blocks for the ATLAS 2012 data are used. Events are required to have a reconstructed primary vertex associated with at least two tracks. The data events are only considered when the trigger system, tracking detectors, calorimeters and magnets were operating at the nominal conditions. More details on event selection can be found in Appendix C.

4.4.2 Jet Selection

This study is mainly focused on multijet final states. Well-reconstructed hadronic jets, along with the jets which are made due to photons and electrons, are used. Since microscopic black holes are expected to decay predominately to SM particles. By considering multijet final states most of the potential black hole signatures are taken into account. Moreover, since the jets from electrons and photons are not identified as different objects than the hadronic jets there is no concern for object double counting. Therefore, this multijet analysis that does not identify other objects considerably simplifies the search method.

In the ATLAS data, jets are reconstructed using the anti-kt clustering algorithm with different values of jet distance parameter [77, 78]. Anti-kt jets with a distance parameter $R = 0.4$ made up of topological calorimeter clusters with a positive energy are used. Furthermore, local cluster weighting (LCW) calibration is used for the jets, which can distinguish between electromagnetic and hadronic jets to apply the appropriate corrections accordingly, greatly improving the jet energy resolution. The jet p_T measurement is further improved by applying offline calibrations and corrections based on different factors such as pseudorapidity, transverse energy and momentum, event topology and event pileup effects [79]. All good

jets (shown in appendix C.1.4), defined by the percentage of tracks in the jet originating from the vertex, are used. Furthermore, jets with $p_T > 50$ GeV are selected to minimize pileup effects. The detailed description of the event pileup and choice of $p_T > 50$ GeV is mentioned in appendix E. In order to obtain the well-measured jets, only jets reconstructed in the central region of the ATLAS detector, i.e. $|\eta| < 2.8$, are chosen.

For different jet multiplicities ($N = 2, 3, ..., 7$) the jet p_T and η distributions are shown in Figures 4.3 and 4.4, respectively. Both the p_T and η distributions for the ATLAS 2012 data are compared with PYTHIA8 and HERWIG++ MCs. For a given jet multiplicity, the dijet MC distributions are normalized with respect to the area under the data curve. For the jet p_T, both PYTHIA8 and HERWIG++ MCs agree with the data to within 30% and are also in good agreement to each other. However, for the jet η, from the data to MC ratio at the bottom of each plot in Figure 4.4, the agreement of the data with PYTHIA8 MC is better than the data with HERWIG++ MC.

4.5 Data Characteristics

H_T is the main variable of this analysis, constructed from the scalar sum of p_T of jets with $p_T > 50$ GeV and pseudorapidity $|\eta| < 2.8$, summarized as

$$H_T = \sum p_T \qquad \text{for } p_T > 50 \text{ GeV and } |\eta| < 2.8. \tag{4.3}$$

The H_T variable is directly formed from the jet p_T which have good agreement between the data and the MCs, as shown in Figure 4.3. Therefore, the disagreement of the data and MCs for the η distributions, shown in Figure 4.4, does not affect the analysis strategy. Furthermore, some other jet kinematic variables, the leading jet p_T, the second leading jet p_T and the jet ϕ, are shown in appendix D.

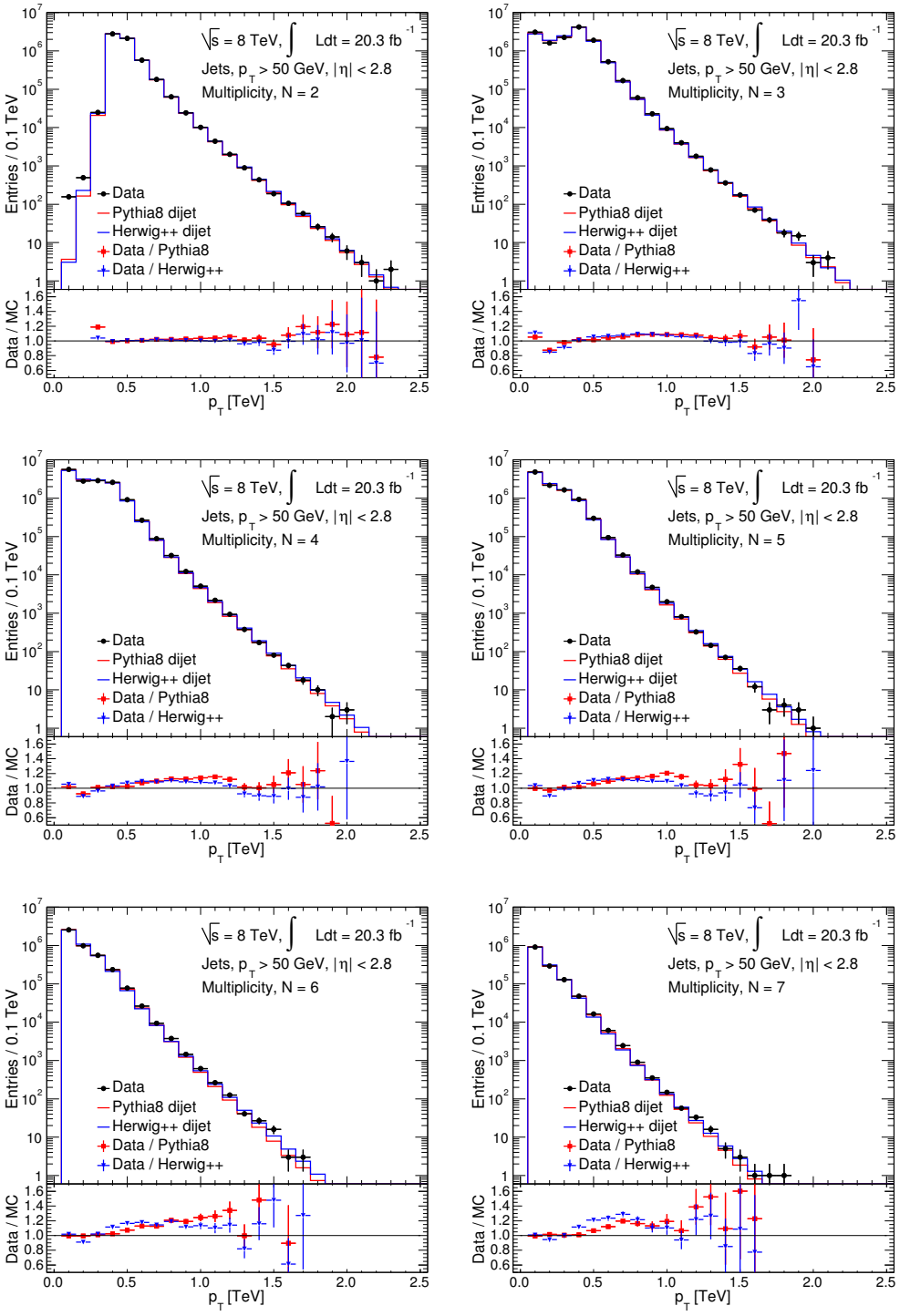

Figure 4.3: The jet p_T distributions for the exclusive jet multiplicities, $N = 2, 3, ..., 7$, for the ATLAS 2012 data, PYTHIA8 (red) and HERWIG++ (blue) MCs. At the bottom of each plot, the ratio of the data to the MC are shown for both the MCs.

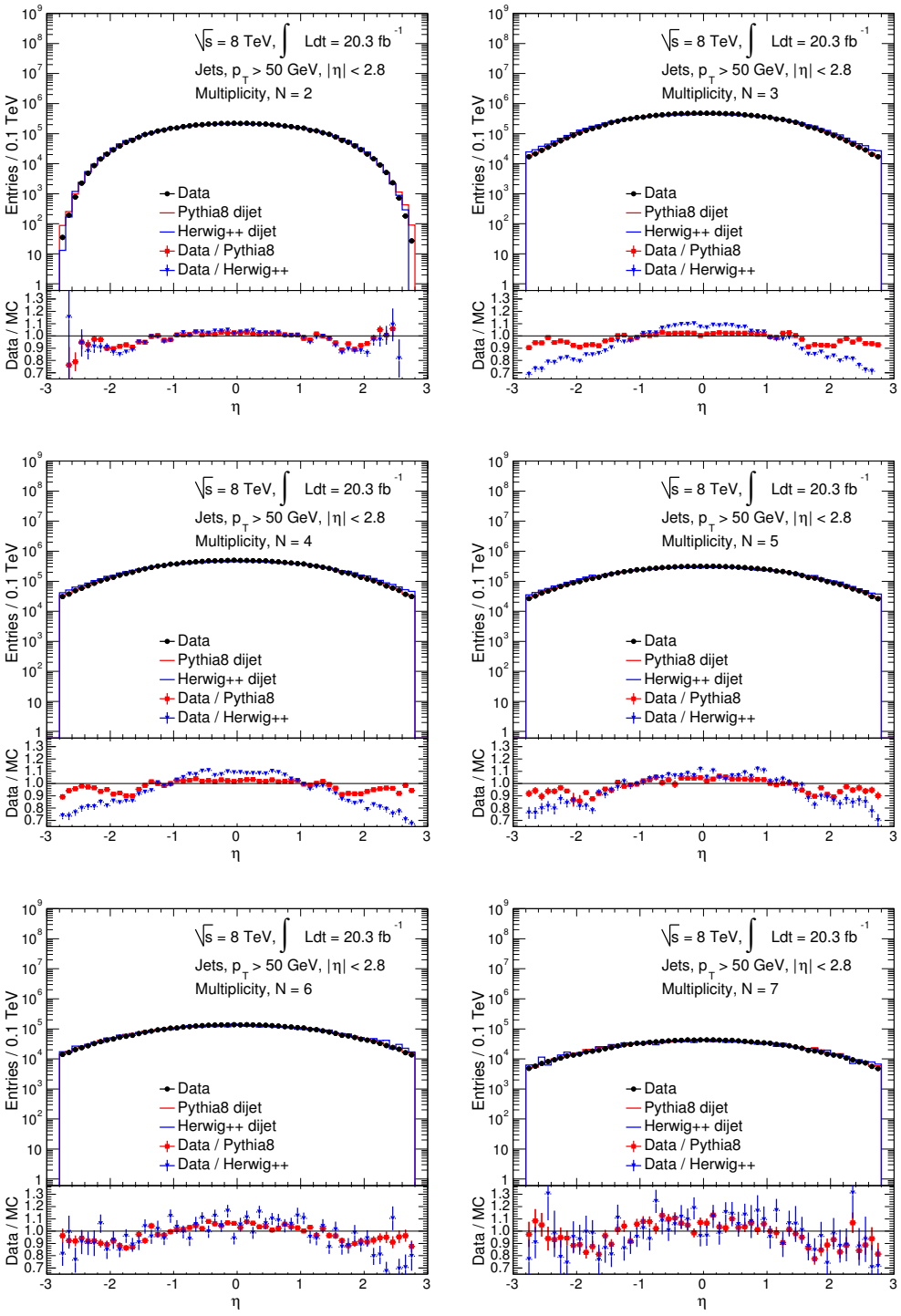

Figure 4.4: The η distributions of jets for the exclusive jet multiplicities, $N = 2, 3, ..., 7$, for the ATLAS 2012 data, PYTHIA8 (red) and HERWIG++ (blue) MCs. At the bottom of each plot, the ratio of the data to the MC are shown for both the MCs.

4.5.1 The H_T Distributions

In this multijet analysis searching for microscopic black hole, the H_T distributions play an important role. The comparison of the H_T distributions for the ATLAS 2012 data, PYTHIA8 and HERWIG++ MCs has been shown in Figures 4.5 and 4.6 for the exclusive jet multiplicities, $N = 2, 3, .., 7$, and inclusive jet multiplicities, $N \geq 2, 3, ..., 7$, respectively. From Figure 4.5, for the exclusive jet multiplicities, the data and the MCs are within 20% agreement, similar to the p_T distributions (Figure 4.3), whereas the agreement is improved for the inclusive jet multiplicities, as shown in Figure 4.6. Since for the inclusive jet multiplicities, many jet multiplicities are considered at once with a lower threshold on jet multiplicity, e.g., $N \geq 3$. The disagreements are therefore compensated to an extent in the H_T distributions.

The shapes of the H_T distributions are expected to be the same for all types of multijet final states and this is the key assumption to estimate the major QCD background in this study. The shape invariance of the H_T distributions for different jet multiplicities, both for the inclusive and exclusive multiplicity cases, will be examined in the next subsection.

4.5.2 Shape Invariance of Kinematic Distributions

The shape of the H_T distribution is considered to be invariant with the jet multiplicity. The shape invariance is expected above an H_T value set by the jet $p_T > 0.05$ TeV selection, i.e., $H_T > [N \times 0.05]$ TeV. The multiplicity-dependent onset for invariance can be observed if the H_T ratios of multiplicities $N > 2$ are inspected with respect to the case of two jets, i.e. $N = 2$, as shown in Figures 4.7 and 4.8. The reason of choosing dijet case as a benchmark case will be described at the end of this subsection. The onset for invariance is different for different multiplicities, but to keep the

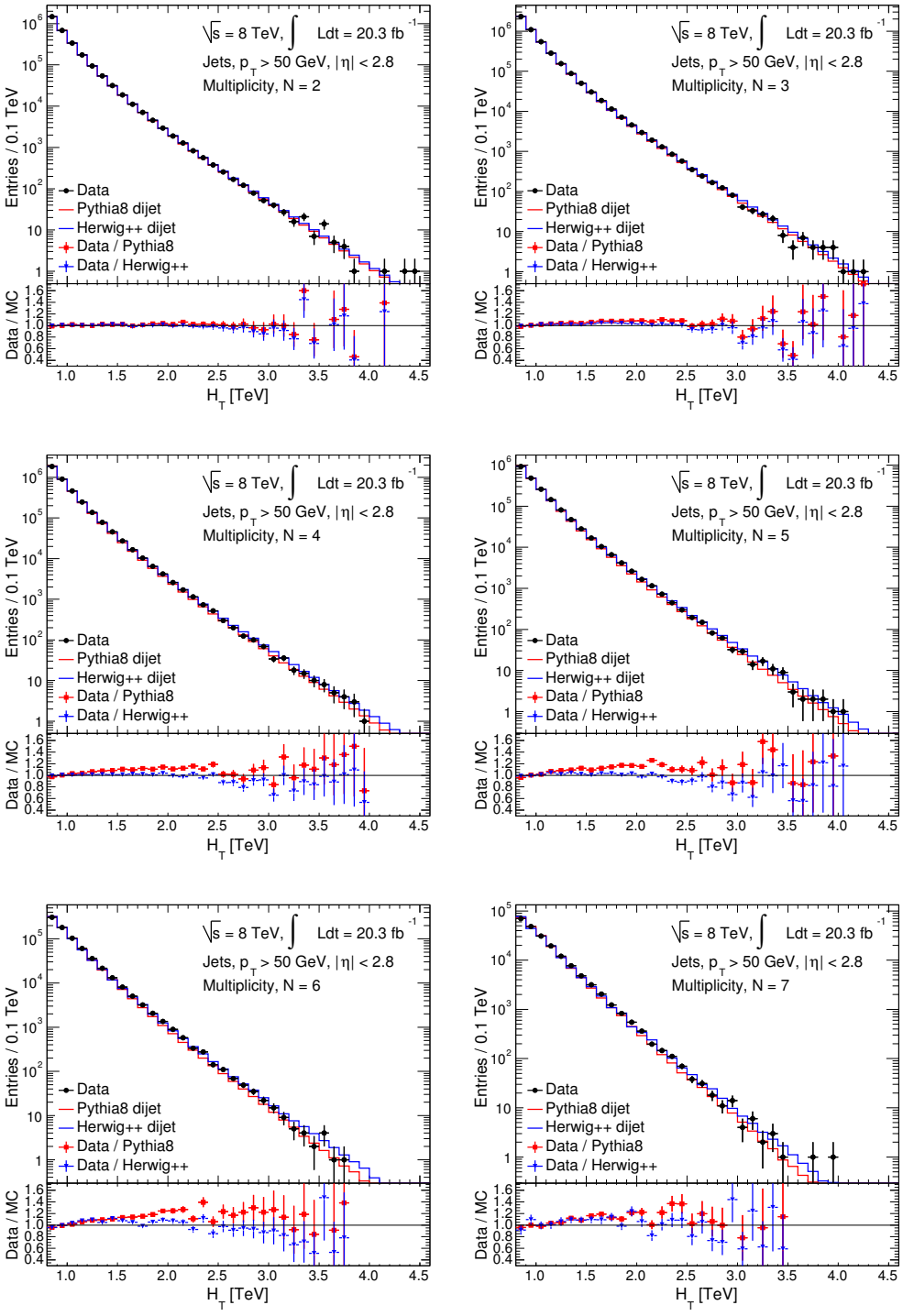

Figure 4.5: The H_T distributions for the exclusive jet multiplicity cases, $N = 2, 3, ..., 7$, for the ATLAS 2012 data, PYTHIA8 (red) and HERWIG++ (blue) MCs. At the bottom of each plot, the ratio of the data to the MC are shown for both the MCs.

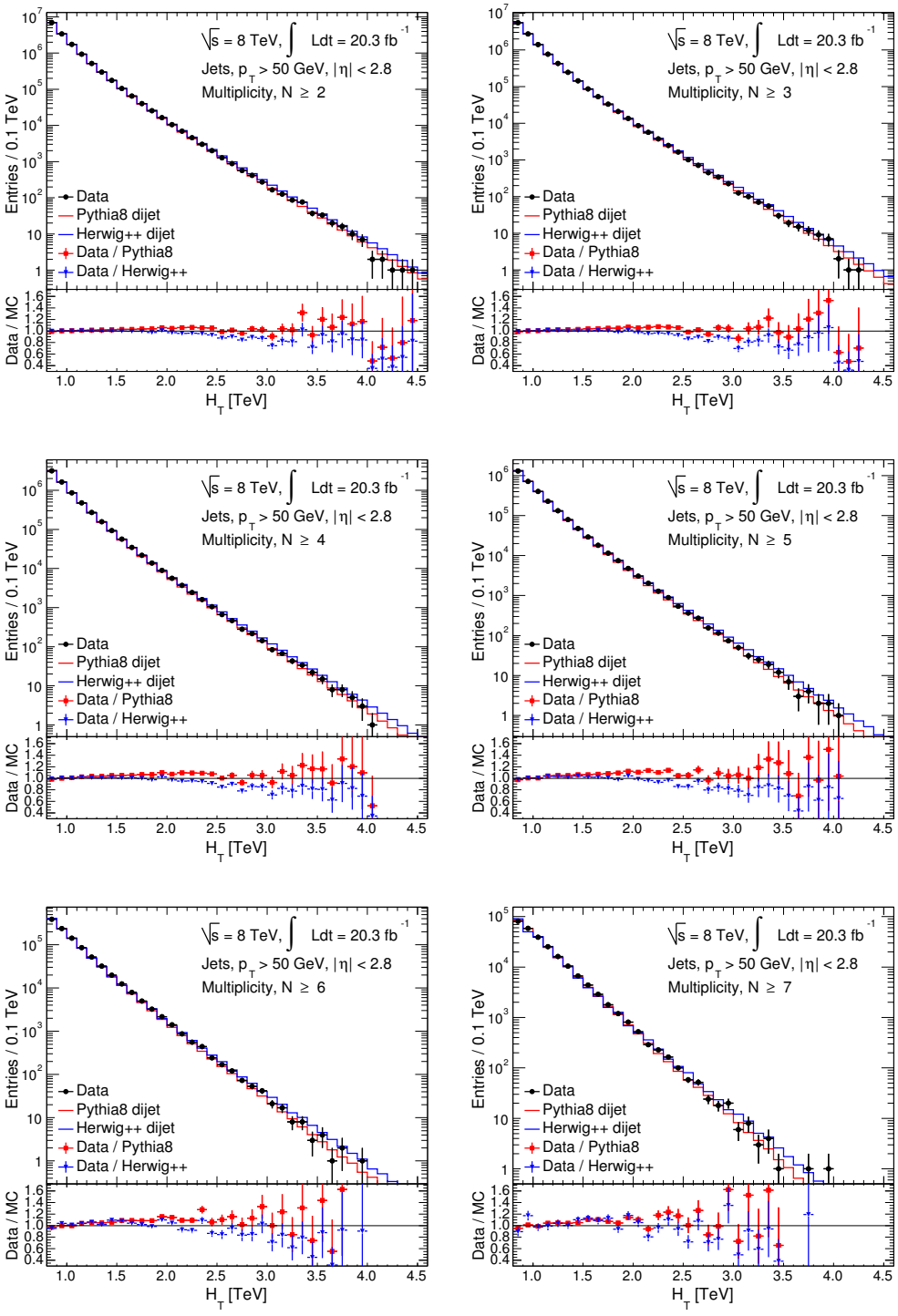

Figure 4.6: The H_T distributions for the inclusive jet multiplicity cases, $N \geq 2, 3, ..., 7$, for the ATLAS 2012 data, PYTHIA8 (red) and HERWIG++ (blue) MCs. At the bottom of each plot, the ratio of the data to the MC are shown for both the MCs.

background estimation procedure general, a common invariant region for all the jet multiplicities is defined. From Figures 4.7 and 4.8, by considering all multiplicity cases under observation, the $H_T > 1.7$ TeV region is chosen where the plateau is observed in the ratio plots. By ignoring the $H_T < 1.7$ TeV region, some kinematical effects can be removed, but still there are some non-invariance effects (negative slopes) for the $H_T > 1.7$ TeV region. These non-invariant effects can be minimized by applying corrections which will be discussed later in this section. After choosing the lower H_T threshold, different upper thresholds on the H_T ratios have been studied and the $1.7 < H_T < 2.4$ TeV region is chosen as the flattest region in the H_T ratios and is defined as the normalisation region.

In order to investigate the shape invariance of the H_T distribution, a detailed study is performed in the normalisation region based on the flatness of the ratio of the H_T distributions. The study of linear fitting and χ^2-tests of the ratios for both the data and the QCD simulated background events determine the flatness in the H_T ratio distributions. The linear fitting tests in the normalisation region, for the exclusive and inclusive jet multiplicities, are shown in Figures 4.9 and 4.10, respectively, for the ATLAS 2012 data, PYTHIA8 dijet and HERWIG++ dijet simulation samples.

The linear fits in the normalisation region shown in Figures 4.9 and 4.10 have different values of fitted slopes and chi-squares (χ^2) depending on the jet multiplicity, giving valuable information about the shape invariance. All the fit parameters are shown in Table 4.4 for the exclusive and inclusive jet multiplicities, corresponding to the data and the QCD background simulations. Ideally, the slope of the straight line fit over the ratio of the H_T distribution should exactly be consistent with zero for perfect shape invariance of the H_T distributions, independent of the jet multiplicity. In most cases, the fit slopes are not consistent with zero but very close to zero,

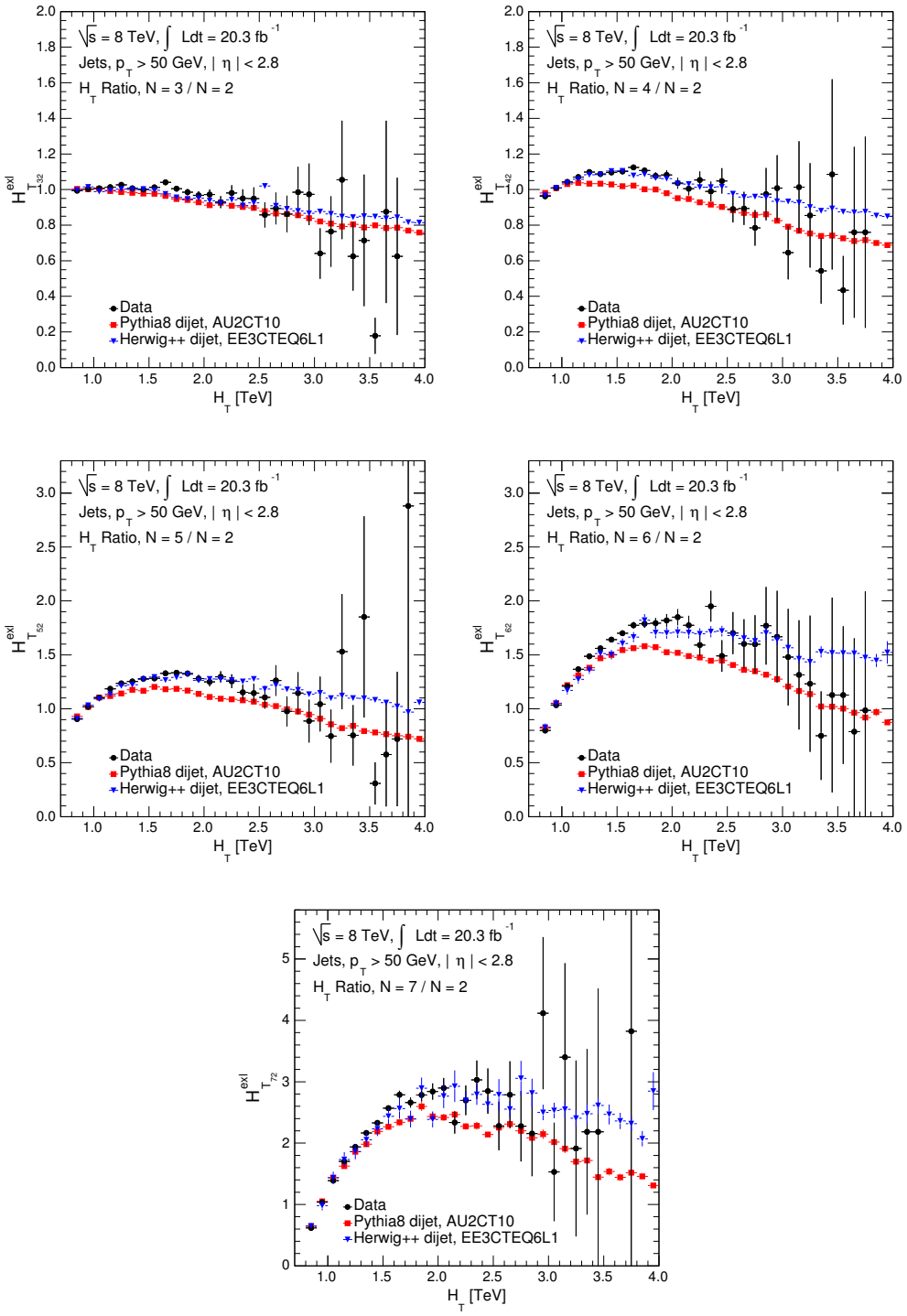

Figure 4.7: The $H_{T_{i2}}^{\mathrm{excl}}$ are the H_T ratios of the exclusive jet multiplicities $i = 3, 4, .., 7$ with respect to the reference jet multiplicity $N = 2$, shown for the ATLAS 2012 data, PYTHIA8 and HERWIG++ MCs.

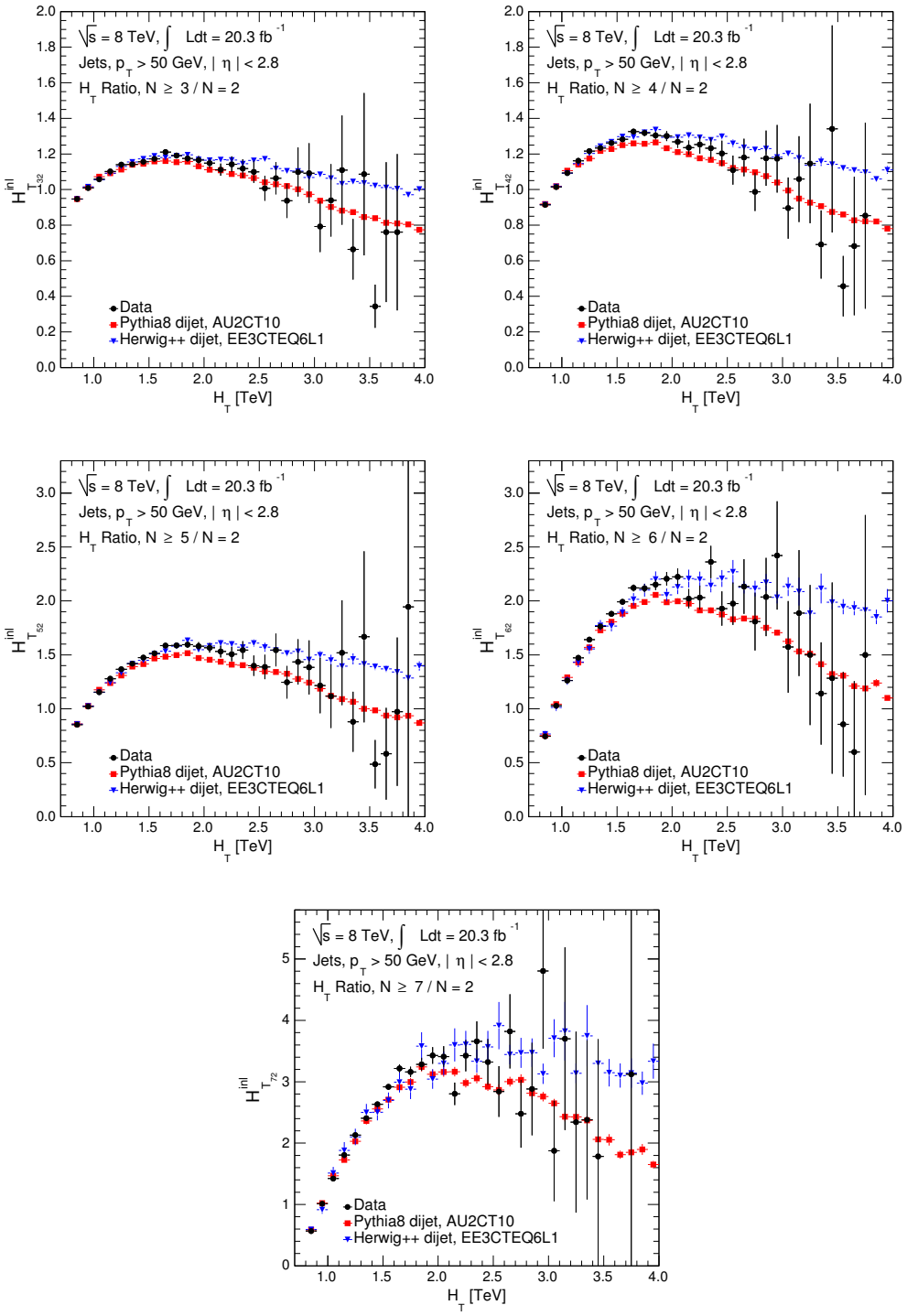

Figure 4.8: The $H_{T_{i2}}^{\text{inl}}$ are the H_T ratios of the inclusive jet multiplicities $i \geq 3, 4, .., 7$ with respect to the reference jet multiplicity $N = 2$, shown for the ATLAS 2012 data, PYTHIA8 and HERWIG++ MCs.

which indicates some non-invariant effects in the normalisation region, as shown in Figure 4.11. In this figure, the slope trends have been shown for the exclusive (top plot) and inclusive (bottom plot) jet multiplicities. The effects from non-invariance are compensated to some extent in the inclusive cases. This is one of the reasons that the model-independent limits calculated on the basis of shape invariance are more reliable for the inclusive jet multiplicities. In Figure 4.11, the slopes shown for the H_T ratios are computed from the jet multiplicities $N > 2$ with respect to the reference jet multiplicity $N = 2$, for the data and the background MCs. Similarly, the option of using the jet multiplicity $N = 3$ as the reference is also studied to check the invariance of the H_T distributions for $N \geq 3$, as shown in Figure 4.12. However, this search for microscopic black holes is more sensitive for higher jet multiplicities, i.e. the probability of a black hole signal is higher for $N = 3$ than $N = 2$. Moreover, the QCD background for dijet case is also very well studied and no resonance has been observed [80–82]. Therefore, it is better to use the dijet case as the benchmark multiplicity and apply non-invariance corrections to the estimated background in the signal region.

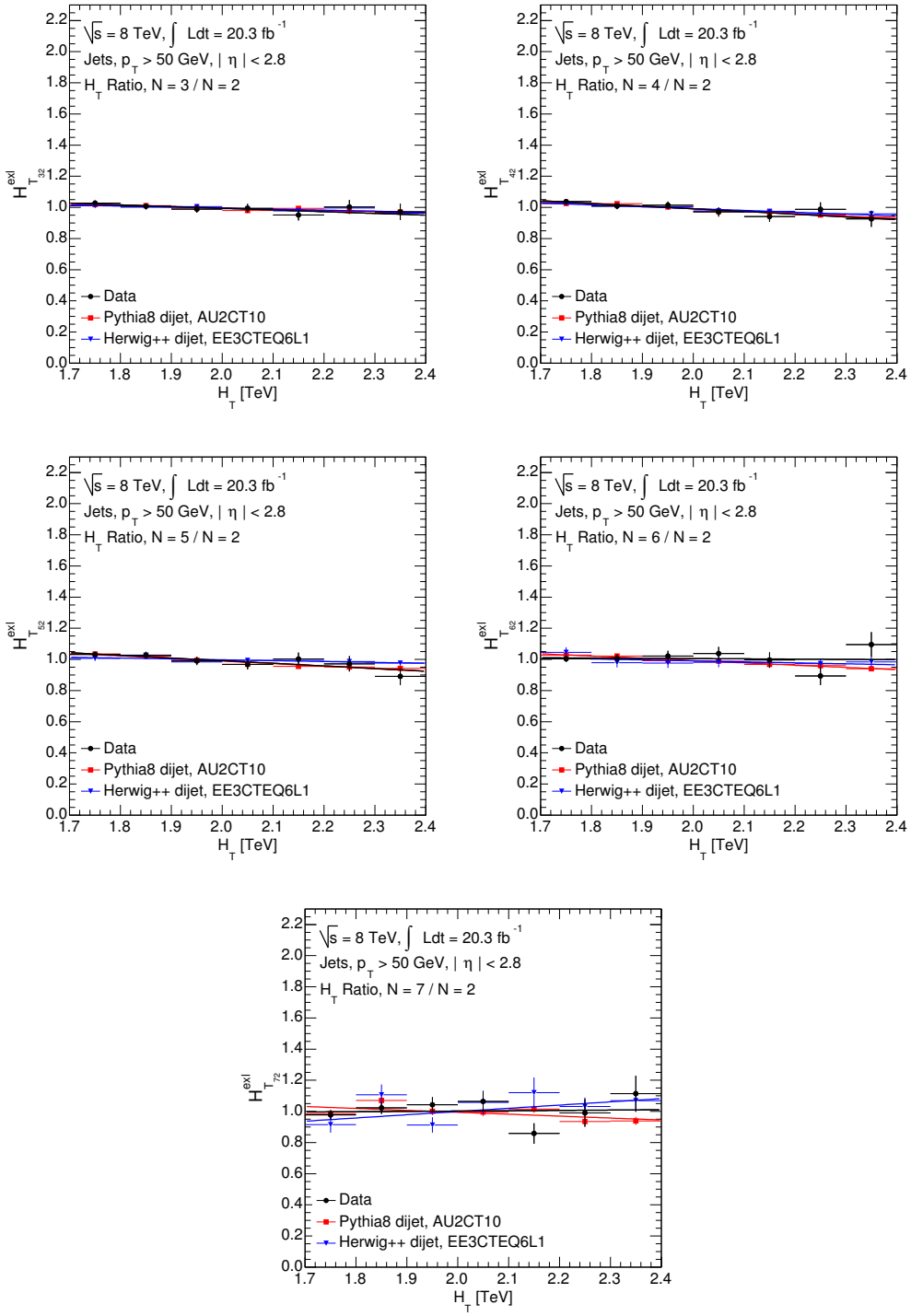

Figure 4.9: The H_{Ti2}^{excl} are the H_T ratios of the exclusive jet multiplicities $i = 3, 4, .., 7$ with respect to the reference jet multiplicity $N = 2$ in the normalisation region $1.7 < H_T < 2.4$ TeV, shown for the ATLAS 2012 data, PYTHIA8 and HERWIG++ MCs.

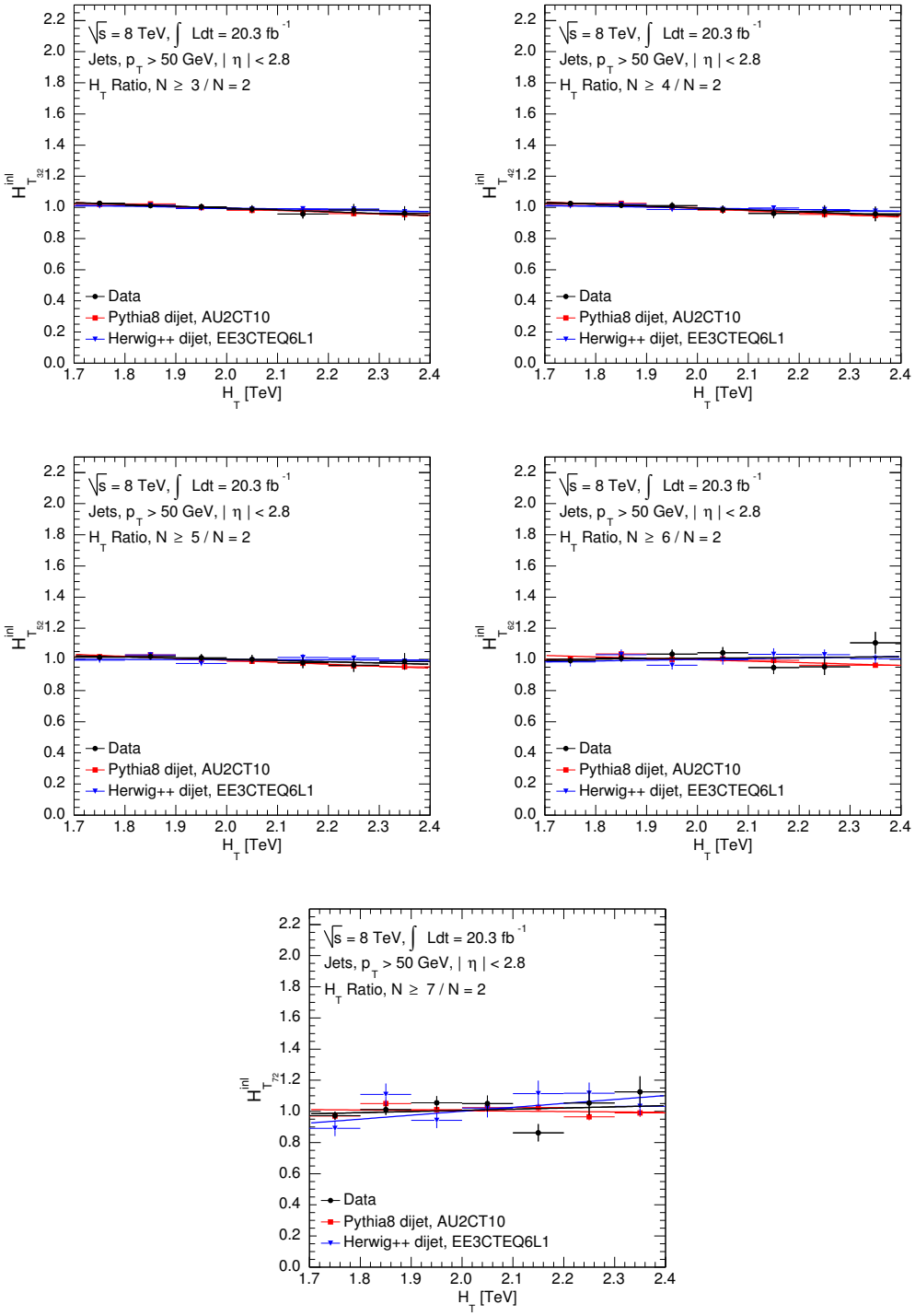

Figure 4.10: The $H_{T_{i2}}^{\text{inl}}$ are the H_T ratios of the inclusive jet multiplicities $i \geq 3, 4, .., 7$ with respect to the reference jet multiplicity $N = 2$ in the normalisation region $1.7 < H_T < 2.4$ TeV, shown for the ATLAS 2012 data, PYTHIA8 and HERWIG++ MCs.

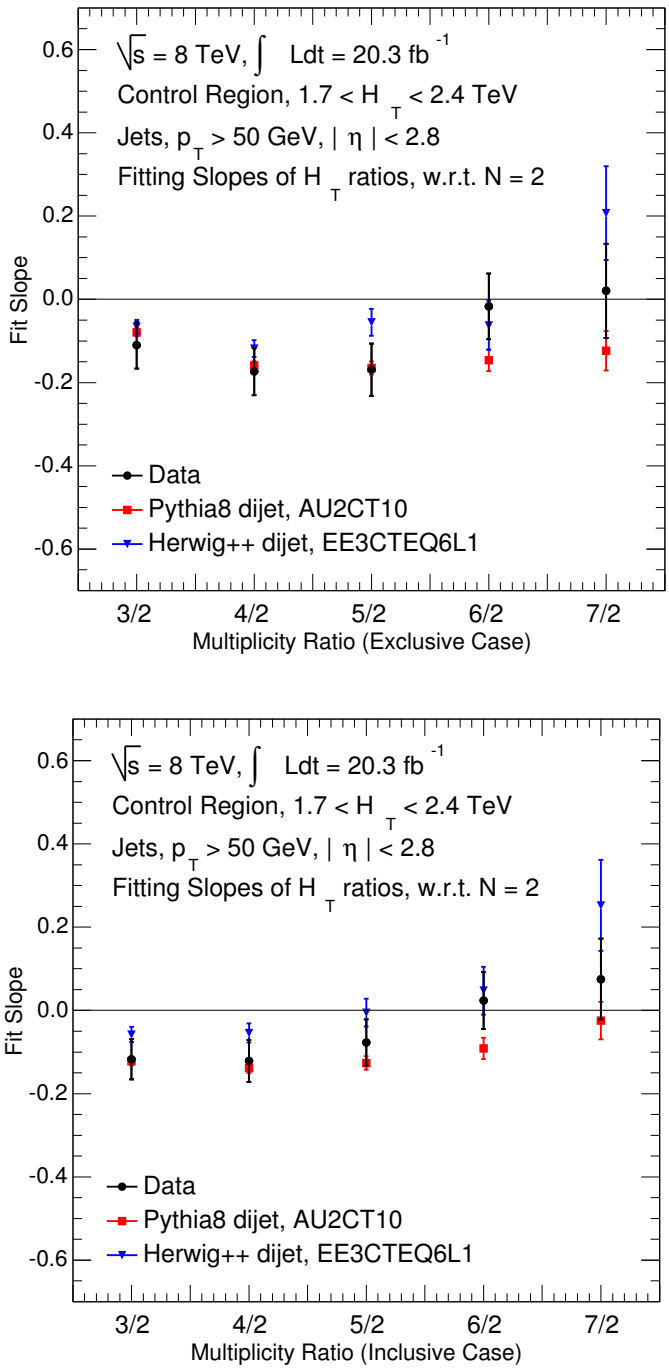

Figure 4.11: The slopes extracted from the straight line fit to the H_T ratios, for the ATLAS 2012 data, PYTHIA8 and HERWIG++ MCs in the normalisation region $1.7 < H_T < 2.4$ TeV. The top (bottom) plot shows the slopes for the exclusive (inclusive) jet multiplicity ratios of $N = 4, 5, .., 7$ ($N \geq 3, 4, ..., 7$) to $N = 2$.

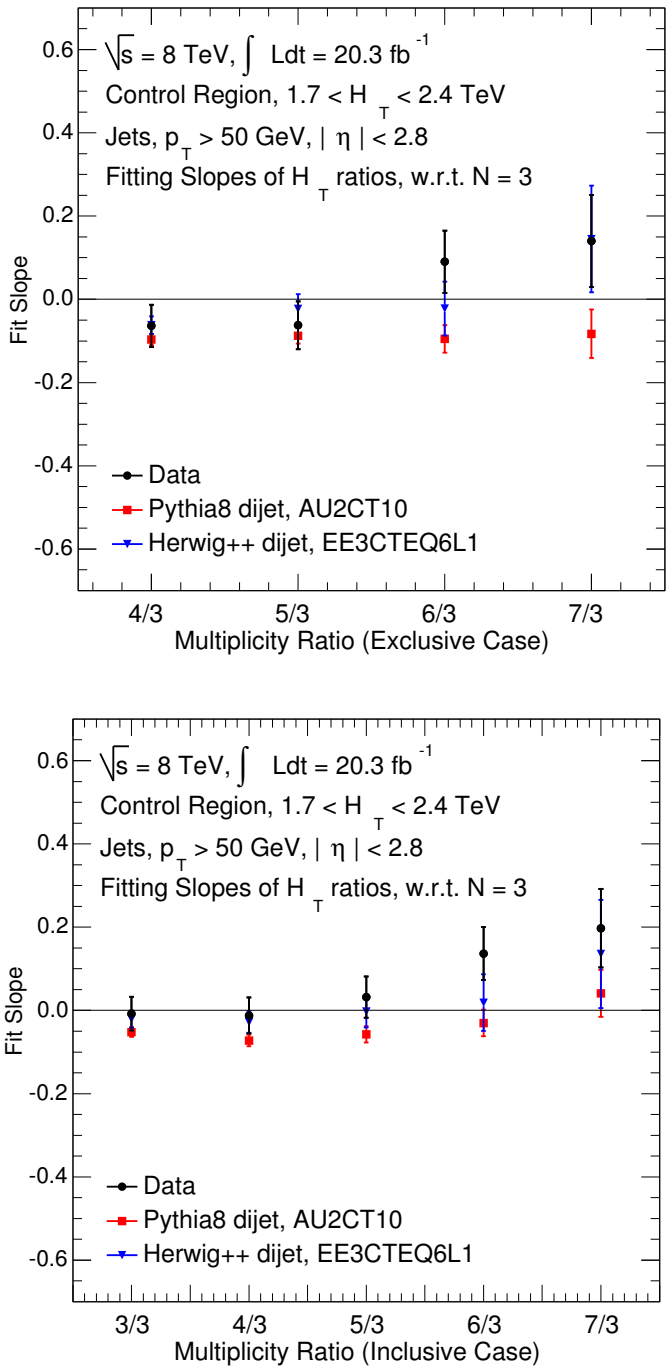

Figure 4.12: The slopes extracted from the straight line fit to the H_T ratios, for the ATLAS 2012 data, PYTHIA8 and HERWIG++ MCs in the normalisation region $1.7 < H_T < 2.4$ TeV. The top (bottom) plot shows the slopes for the exclusive (inclusive) jet multiplicity ratios of $N = 4, 5, .., 7$ ($N \geq 3, 4, ..., 7$) to $N = 3$.

H_T Ratio	Fit Slope			χ^2/NDF		
	Data	PYTHIA8	HERWIG++	Data	PYTHIA8	HERWIG++
$H^{\text{excl}}_{T_{32}}$	-0.11 ± 0.06	-0.08 ± 0.01	-0.07 ± 0.02	1.76/5 = 0.35	8.01/5 = 1.60	6.34/5 = 1.27
$H^{\text{excl}}_{T_{42}}$	-0.17 ± 0.06	-0.16 ± 0.01	-0.12 ± 0.02	1.92/5 = 0.38	7.39/5 = 1.48	1.95/5 = 0.39
$H^{\text{excl}}_{T_{52}}$	-0.17 ± 0.06	-0.16 ± 0.02	-0.06 ± 0.03	2.12/5 = 0.42	6.36/5 = 1.27	2.65/5 = 0.53
$H^{\text{excl}}_{T_{62}}$	-0.02 ± 0.08	-0.15 ± 0.03	-0.06 ± 0.06	5.81/5 = 1.16	0.88/5 = 0.18	2.50/5 = 0.50
$H^{\text{excl}}_{T_{72}}$	0.02 ± 0.11	-0.12 ± 0.05	0.21 ± 0.11	8.36/5 = 1.67	10.93/5 = 2.19	8.50/5 = 1.70
$H^{\text{inl}}_{T_{32}}$	-0.12 ± 0.05	-0.12 ± 0.01	-0.06 ± 0.02	0.75/5 = 0.15	7.47/5 = 1.49	2.48/5 = 0.50
$H^{\text{inl}}_{T_{42}}$	-0.12 ± 0.05	-0.14 ± 0.01	-0.05 ± 0.02	0.56/5 = 0.11	7.36/5 = 1.47	3.35/5 = 0.67
$H^{\text{inl}}_{T_{52}}$	-0.08 ± 0.06	-0.13 ± 0.02	-0.01 ± 0.03	0.63/5 = 0.13	5.04/5 = 1.01	5.76/5 = 1.15
$H^{\text{inl}}_{T_{62}}$	0.02 ± 0.07	-0.09 ± 0.03	0.05 ± 0.06	7.37/5 = 1.47	7.26/5 = 1.45	3.82/5 = 0.76
$H^{\text{inl}}_{T_{72}}$	0.07 ± 0.10	-0.02 ± 0.05	0.25 ± 0.11	11.28/5 = 2.26	10.02/5 = 2.00	8.40/5 = 1.68

Table 4.4: The $H^{\text{excl}}_{T_{32}}$ is the H_T ratio of the exclusive jet multiplicity $N = 3$ to the jet multiplicity $N = 2$. Similarly, $H^{\text{inl}}_{T_{32}}$ is the H_T ratio of the inclusive multiplicities $N \geq 3$ to the jet multiplicity $N = 2$, and so on. The slopes of straight line fits with errors and χ^2/NDF for the different H_T ratios are shown for the ATLAS 2012 data, PYTHIA8 and HERWIG++ MCs. All the values are extracted from the normalisation region $1.7 < H_T < 2.4$ TeV.

4.5.3 The Signal and the Control Regions

In this study, three mutually exclusive regions are defined: the control region, the normalisation region and the signal region with respect to the (N, H_T) variable space. The regions are defined as following:

- control region: $N = 2$ and $H_T > 1.7$ TeV.
  This region is well-described by SM processes, and no resonances or threshold enhancements have been observed at the LHC.

- normalisation region: $N \geq 2$ and $1.7 < H_T < 2.4$ TeV.
  In this region, the H_T distribution for any jet multiplicity $N > 2$ is normalized to the jet multiplicity $N = 2$.

- signal region: $N > 2$ and $H_T > 2.4$ TeV.
  Only this region is searched for possible signals.

In summary, the control region does not contain any threshold enhancement or resonance and the SM processes are dominant in the region. Moreover, microscopic black holes are expected to produce high multiplicity final states. Therefore, in the multijet study, the choice of the dijet case is safe for the control region. The flattest region in the H_T ratio is chosen as the normalisation region, the sub-region of the control region with best shape invariance. The flatness in the H_T ratio ensures the control region fit has a better background estimation for the signal region. To estimate the background for $N > 2$ a normalisation factor is determined from the normalisation region to normalize the control region fit. Finally, the signal region can be defined beyond the upper threshold of the normalisation region.

4.5.4 The Background Estimation

The QCD background is determined by using an ansatz fitting function,

$$f(x) = \frac{p_0(1-x)^{p_1}}{x^{p_2+p_3 \ln x}}, \tag{4.4}$$

where p_0, p_1, p_2 and p_3 are the fit parameters and $x \equiv H_T/\sqrt{s}$. The function is fit to the H_T distribution for the data instead of x. For a physical background estimation from the H_T distributions, the function should be continuously decreasing in an allowed range and have physical values at the tail. This function was already used in invariant mass study for the smooth SM dijet and γ+jet backgrounds in different experiments at both the Tevatron and LHC [80, 83, 84].

The parameter p_0 acts as a normalisation factor and does not affect the shape of the fit, but its value depends on the other fit parameters which are highly correlated with the x-dependent factors in equation (4.4). On the other hand, fits with the same shapes and different normalisation factors will have identical p_1, p_2 and p_3 but different p_0. Therefore, $p_0 > 0$ is required to fit any H_T distribution for a shape-dependent analysis.

The factor $(1-x)^{p_1}$ in the numerator of equation (4.4) controls the upper physical threshold of x. Assuming $p_1 > 0$, the function vanishes as $x \to 1$, since no event can be produced above $\sqrt{s}$ ($x > 1$). Hence, it is appropriate to require $p_1 > 0$ to maintain the continuously decreasing trend of the QCD background at high x. Furthermore, the function is not required to fit a resonance or increase with H_T due to a non-perturbative gravity signal. The function is designed to fit to the background only.

For the factor $x^{p_2+p_3 \ln x}$ in the denominator of equation (4.4), p_3 is the relevant parameter as $x \to 0$ because $\ln x \to -\infty$ as $x \to 0$. There are two possibilities[1] for the function as $x \to 0$ depending on the parameter p_3.

[1] The possibility of $p_3 = 0$ is ignored because the function to fit the data has four parameters, and requiring $p_3 = 0$ changes the function.

Fit parameters	$p_0 \pm \Delta p_0$	$p_1 \pm \Delta p_1$	$p_2 \pm \Delta p_2$	$p_3 \pm \Delta p_3$
	0.03 ± 0.00	4.72 ± 0.18	11.29 ± 0.06	1.57 ± 0.04

Table 4.5: The values of fit parameters (p_i) along with errors (Δp_i) for the function $f(x) = \frac{p_0(1-x)^{p_1}}{x^{p_2+p_3 \ln x}}$ fitted to the dijet H_T distribution for the ATLAS 2012 data.

The first possibility is that the function approaches infinity as $x \to 0$, which requires $p_3 < 0$. The value of the function becomes non-physical at $x = 0$, but it can be avoided by applying a small x cut-off in the experimental H_T distributions and the function remains physical in the measured x-range. The second possibility is to have a function maximum in the $0 < x < 1$ range and a decreasing trend as $x \to 0$ by requiring $p_3 > 0$. The requirement does not remain physical and intuitive if the function peak lies within the x-range under consideration. This possibility can only be taken into account if the peak of the function lies below the minimum x of the experimental H_T distributions. In conclusion, all the parameters are constrained to have a monotonically decreasing function trend with a negative slope for the x-range under consideration. The values of all the fit parameters are shown in the Table 4.5. In this study, the resulting experimental limits are for the particular choice of the ansatz function similar to the choice of a benchmark signal model.

The function in equation (4.4) is used to fit the control region only. The shape of the control region fit is normalized based on the H_T distributions in the normalisation region, which is used to determine the background shapes in the signal region. Using the observed number of events compared to the predicted number of SM background events in the signal region, upper limits are set on the production of new physics and microscopic black holes.

The background prediction along with three sigma uncertainty band

due to fit parameter errors is shown in Figures 4.13 and 4.14 for both the exclusive and inclusive jet multiplicities. The three sigma uncertainty band is shown because one and two sigma bands are too narrow to be seen clearly. In these figures, there is an overestimation of background for most of jet multiplicity cases in the signal region. In the next subsection, the source of this problem and correction to the background estimation is discussed.

4.5.5 Correction to the Background Estimation

From Figures 4.7 and 4.8, the QCD MCs show non-invariant effects in the H_T distributions. It can be concluded that the non-invariant effects are causing an overestimation of the data-driven background in the signal region. Therefore, correction factors are derived from both the PYTHIA8 and HERWIG++ MCs and applied to the data-driven background to compensate for the H_T non-invariance in the signal region. Any possible signal bias can be avoided by using correction factors derived from the QCD MCs. The H_T ratio for the MC distributions in the normalisation region can be written as

$$\left[\frac{1}{n_f^{\text{nom.}}}\frac{H_T^{N>2}}{H_T^{N=2}}\right]_{\text{MC}} = \left[ax^{'} + b\right]_{\text{MC}}, \tag{4.5}$$

where $x^{'} \equiv H_T$, $n_f^{\text{nom.}}$ is the normalisation factor measured in the nominal normalisation region, i.e. $1.7 < H_T < 2.4$ TeV, and a and b are the slope and intercept of the straight line, respectively. The straight line fit $[ax^{'} + b]_{\text{MC}}$ obtained from equation (4.5) is used as a correction factor and applied to the background estimation. For the $N > 2$ background estimation, by using the shape invariance assumption, the control region fit is multiplied by a normalisation factor (as described in subsection 4.5.4), i.e.

$$f^{N>2}(x) = n_f^{\text{nom.}} f(x) = n_f^{\text{nom.}} \frac{p_0(1-x)^{p_1}}{x^{p_2+p_3 \ln x}}, \tag{4.6}$$

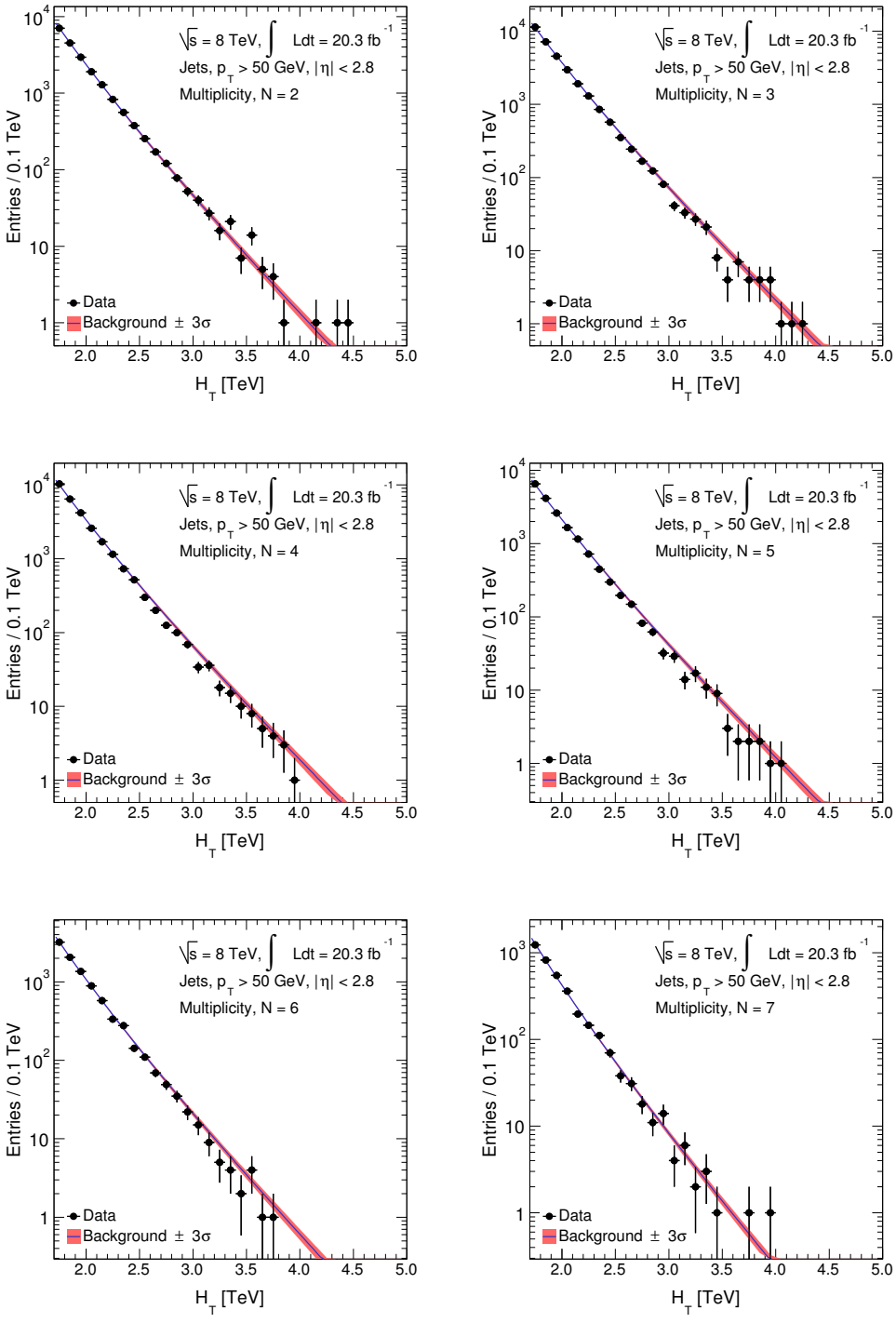

Figure 4.13: The background estimation for the H_T distributions with 3σ uncertainty, for the exclusive jet multiplicities $N = 2, 3, ..., 7$.

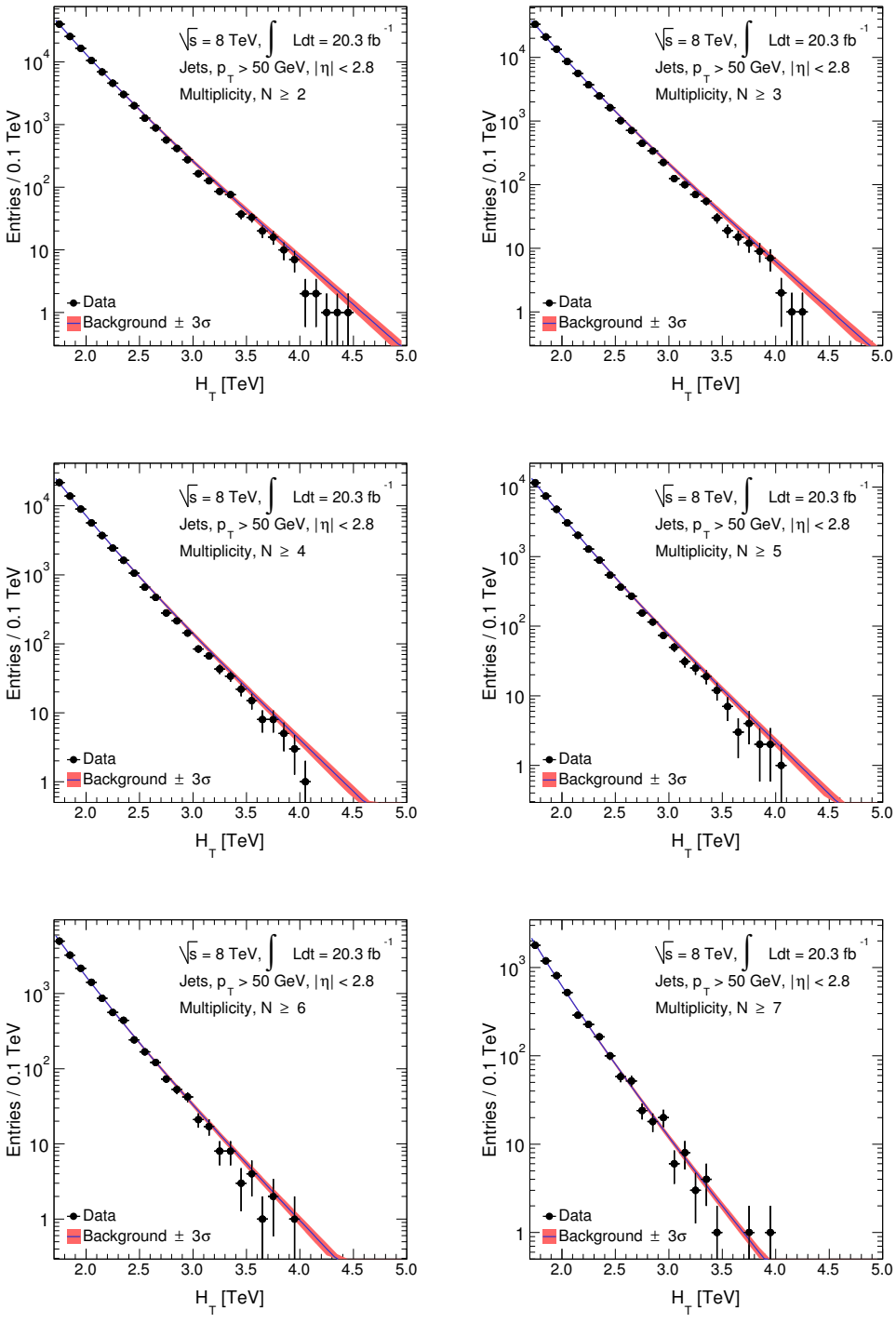

Figure 4.14: The background estimation for the H_T distributions with 3σ uncertainty, for the inclusive jet multiplicities $N \geq 2, 3, ..., 7$.

where $f(x)$ is the function described in equation (4.4) used to fit the dijet H_T distribution and $f^{N>2}(x)$ is the same function multiplied by a normalisation factor ($n_f^{\text{nom.}}$) used to determine the background for the jet multiplicities $N > 2$. Now the corrected function $f^{N>2}_{\text{corr.}}(x)$ can be written as

$$f^{N>2}_{\text{corr.}}(x) = f^{N>2}(x)\left[ax^{'} + b\right]_{\text{MC}} = \left[n_f^{\text{nom.}}\frac{p_0(1-x)^{p_1}}{x^{p_2+p_3\ln x}}\right]\left[ax^{'} + b\right]_{\text{MC}}, \quad (4.7)$$

where $x \equiv x^{'}/\sqrt{s} = H_T/\sqrt{s}$. Equation (4.7) illustrates that the data-driven background for all the H_T distributions other than $N = 2$ is corrected by the straight line parameters obtained from the H_T distributions for the QCD MCs. If the background is corrected by PYTHIA8, then the slope $a \equiv a_P$ and intercept $b \equiv b_P$ are extracted from the H_T distributions for the PYTHIA8 MC. Similarly, $a \equiv a_H$ and $b \equiv b_H$ are the slope and intercept corresponding to the straight line corrections based on HERWIG++ MC.

Finally, both the PYTHIA8 and HERWIG++ MCs are used to apply a final correction on the data-driven background in the signal region. The slope and intercept trends are averaged for both the MC distributions as $a \equiv (a_P + a_H)/2$ and $b \equiv (b_P + b_H)/2$. The uncorrected background ($\text{B}_{\text{uncorr.}}$), PYTHIA8 corrected background ($\text{B}^{\text{P}}_{\text{corr.}}$), HERWIG++ corrected background ($\text{B}^{\text{H}}_{\text{corr.}}$), and combined PYTHIA8 and HERWIG++ corrected background ($\text{B}^{\text{MC}}_{\text{corr.}}$) are shown in Figures 4.15 and 4.16, for the exclusive and inclusive jet multiplicity cases.

The uncorrected background ($\text{B}_{\text{uncorr.}}$) is corrected by multiplying a correction factor (CF) derived from the MC H_T distributions. The corrected background can be expressed in terms of correction factors based on PYTHIA8 MC, HERWIG++ MC and both the MCs as

$$\text{B}^{\text{P}}_{\text{corr.}} = \text{CF}^{\text{P}}\text{B}_{\text{uncorr.}},\ \text{B}^{\text{H}}_{\text{corr.}} = \text{CF}^{\text{H}}\text{B}_{\text{uncorr.}} \text{ and } \text{B}^{\text{MC}}_{\text{corr.}} = \text{CF}^{\text{MC}}\text{B}_{\text{uncorr.}}, \quad (4.8)$$

where CF^{P}, CF^{H} and CF^{MC} are the correction factors derived from PYTHIA8,

HERWIG++ and both the MCs, respectively. The uncertainty due to this correction will be discussed in the next section 4.6.

4.6 Systematic Uncertainties

In this multijet search for microscopic black holes, the main QCD background is directly estimated from the data on the basis of a shape invariance assumption using the ansatz fitting function described in subsection 4.5.4. The ansatz function used in this study is a choice to fit the data. There may be a different arbitrary function that fits the data as well. Therefore, a particular choice of an ansatz function may lead to a systematic uncertainty. There are two approaches to handle the systematic uncertainty due to the choice of a specific function. The first approach is to not consider this type of systematic uncertainty and understand the resulting experimental limits based on the particular function. This method is similar to choosing a benchmark signal model for a study, i.e. the ansatz of new physics. The second approach is to use two alternative functions, one that gives larger results while the other gives lower results when compared to the nominal function. This takes the uncertainty due to the choice of function into account. The amount of uncertainty depends again on the choice of the two alternative functions out of many arbitrary choices. In this analysis, the first approach is adopted.

The largest uncertainty involved in the background estimation arises due to the MC-based corrections to the non-invariant effects in the H_T distributions for different jet multiplicities. The background estimation in the signal region also has uncertainties related to the relative differences from the choice of the normalisation region. Different normalisation ranges will result in different values of normalisation factors and, hence, the background estimation.

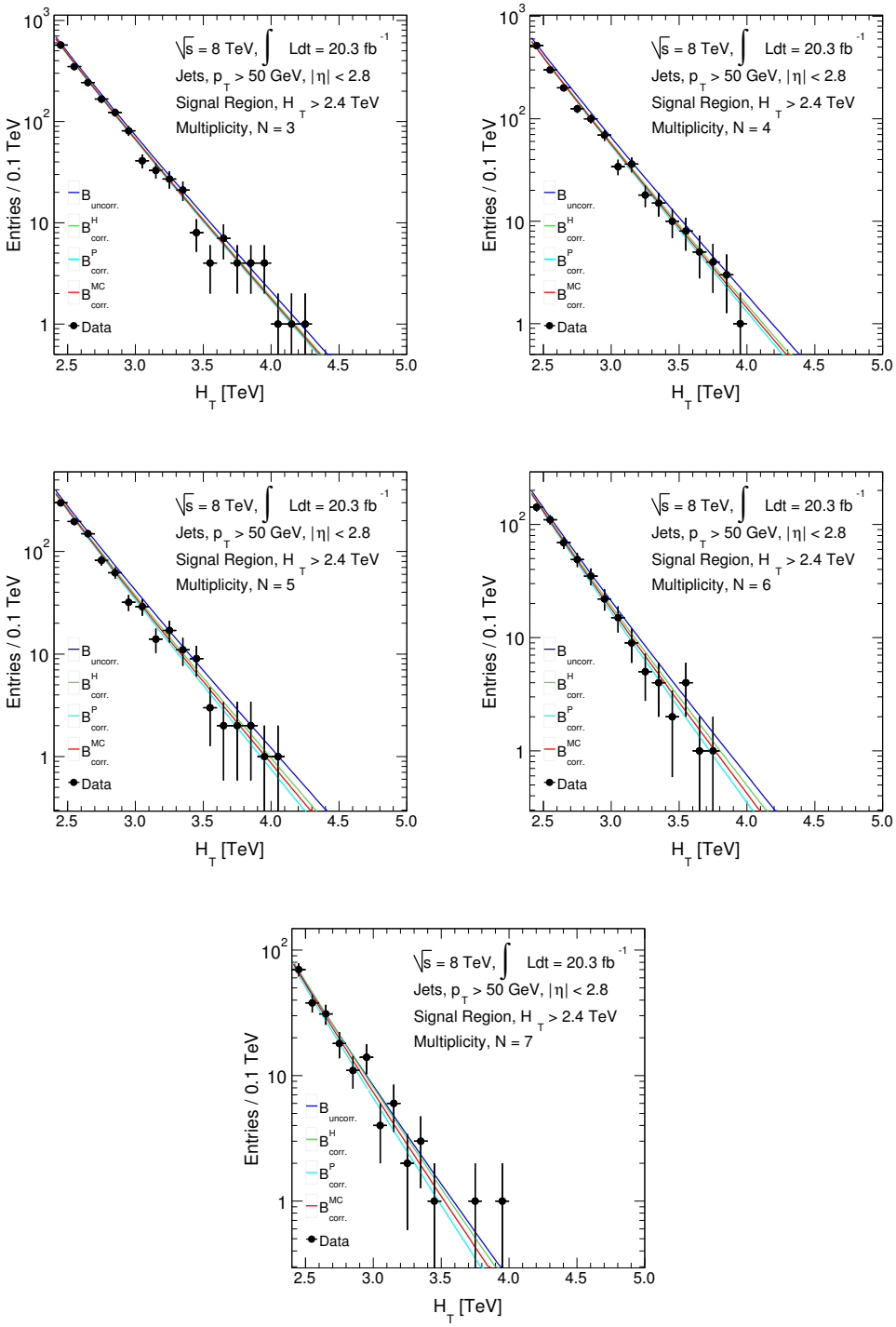

Figure 4.15: The H_T distributions in the signal region, for the exclusive jet multiplicities $N = 3, 4, .., 7$, and the background estimations from the uncorrected fit ($B_{uncorr.}$), HERWIG++ MC corrected fit ($B^{H}_{corr.}$), PYTHIA8 MC corrected fit ($B^{P}_{corr.}$) and the corrected fit based on both the MCs ($B^{MC}_{corr.}$), are shown for the ATLAS 2012 data.

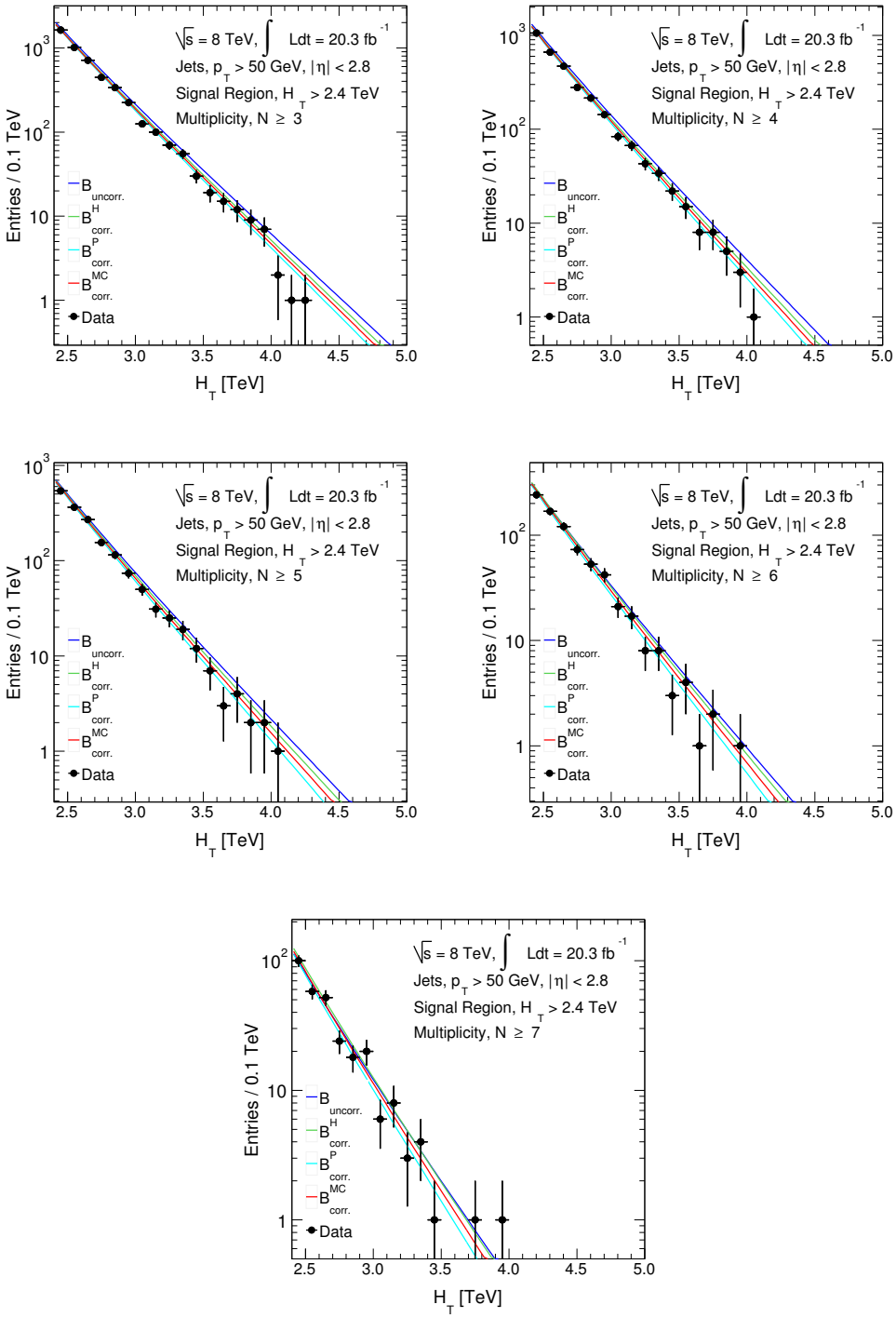

Figure 4.16: The H_T distributions in the signal region, for the inclusive jet multiplicities $N \geq 3, 4, .., 7$, and the background estimations from the uncorrected fit ($B_{uncorr.}$), HERWIG++ MC corrected fit ($B^{H}_{corr.}$), PYTHIA8 MC corrected fit ($B^{P}_{corr.}$) and the corrected fit based on both the MCs ($B^{MC}_{corr.}$), are shown for the ATLAS 2012 data.

Finally, the typical jet energy uncertainties due to the jet energy resolution (JER) [85] and the jet energy scale (JES) [86] also affect the background estimation. The jet energy uncertainties are comparatively smaller than the uncertainties due to corrections to the non-invariant H_T shapes and larger than the uncertainties due to the choice of the normalisation region. Overall, there are three types of systematic uncertainties involved in this study:

- Corrections to non-invariance,
- Choice of normalisation region, and
- Jet energy uncertainties.

By using all these systematic uncertainties, the model-independent and model-dependent limits are calculated, shown in the next section. Microscopic black holes are expected to produce a range of jet multiplicities instead of biasing towards any particular multiplicity. It is therefore more intuitive to consider the inclusive jet multiplicities only, i.e. $N \geq 3, 4, ..., 7$, for the limit calculations. Also, the large effect of jet migrations from one multiplicity bin to another due to the above-mentioned uncertainties can greatly be suppressed by using the inclusive jet multiplicities. Furthermore, the shape invariance in the normalisation region is better for the inclusive jet multiplicities, which results in reducing all the uncertainties. Therefore, the systematic uncertainties will be described in the following subsections only for the inclusive jet multiplicities.

4.6.1 Corrections to Non-Invariance

The MC-based corrections applied to the data-driven background, to compensate the non-invariant effects, introduce the largest uncertainty in this study. These corrections are derived from the straight line fits to the H_T

ratios in the signal region for the dijet MCs, as described in the subsection 4.5.5. The overall systematic uncertainty due to these corrections to the non-invariance would involve the statistical uncertainty measured from errors on fit parameters and the systematic uncertainty measured from the difference between the fit parameters of the straight lines for the two MCs. The systematic uncertainty due to corrections to the non-invariance ($\Delta B^{\rm syst.}_{\rm corr.}$) is the ratio of the difference between the straight line fits to the sum of the straight line fits of two MCs over all the H_T bins of the signal region, i.e.

$$\Delta B^{\rm syst.}_{\rm corr.} = \sum_{H_T \epsilon SR} \frac{\left|(a_P + b_P x^{'}) - (a_H + b_H x^{'})\right|}{(a_P + b_P x^{'}) + (a_H + b_H x^{'})}, \tag{4.9}$$

where $x^{'} \equiv H_T$ while $a_P(a_H)$ and $b_P(b_H)$ are the intercept and slope of the straight line fits corresponding to the PYTHIA8 (HERWIG++) MCs. The statistical uncertainty due to corrections to the non-invariance ($\Delta B^{\rm stat.}_{\rm corr.}$) from these fits is written as

$$\Delta B^{\rm stat.}_{\rm corr.} = \frac{1}{2} \sum_{H_T \epsilon SR} \sqrt{(\sigma_P)^2 + (\sigma_H)^2}, \tag{4.10}$$

where σ_P and σ_H are the one sigma fit errors corresponding to PYTHIA8 and HERWIG++, respectively. The total uncertainty on the estimated background due to corrections to the effects from non-invariance ($\Delta B^{\rm tot.}_{\rm corr.}$) derived from both the MCs in the signal regionsignal region, is written as

$$\Delta B^{\rm tot.}_{\rm corr.}(\%) = \sqrt{(\Delta B^{\rm stat.}_{\rm corr.})^2 + (\Delta B^{\rm syst.}_{\rm corr.})^2} \times 100. \tag{4.11}$$

For different lower thresholds ($H_T^{\rm min}$) of the signal regions, the number of entries for the data, uncorrected background ($\rm B_{uncorr.}$), PYTHIA8 correction factor ($\rm CF^P$), HERWIG++ correction factor ($\rm CF^H$), correction factor derived from both the MCs ($\rm CF^{MC}$), and the uncertainties ($\Delta \rm B^{stat.}_{corr.}$, $\Delta \rm B^{syst.}_{corr.}$ and $\Delta \rm B^{tot.}_{corr.}$) due to $\rm CF^{MC}$ shown in Tables 4.6 to 4.10 for the inclusive jet multiplicities $N \geq 3, 4, ..., 7$, respectively.

$H_T^{\min}$	Data	$B_{\text{uncorr.}}$	CF^{P}	CF^{H}	CF^{MC}	$\Delta B_{\text{corr.}}^{\text{stat.}}$ (%)	$\Delta B_{\text{corr.}}^{\text{syst.}}$ (%)	$\Delta B_{\text{corr.}}^{\text{tot.}}$ (%)
2.4	4812	5451.76	0.89	0.94	0.92	9.32	10.15	13.78
2.5	3181	3723.96	0.88	0.93	0.90	8.95	10.50	13.80
2.6	2168	2556.31	0.86	0.92	0.89	8.61	10.86	13.86
2.7	1455	1762.81	0.84	0.92	0.88	8.28	11.23	13.95
2.8	1008	1220.76	0.83	0.91	0.87	7.98	11.60	14.08
2.9	670	848.68	0.81	0.90	0.86	7.70	11.98	14.24
3.0	446	592.11	0.79	0.89	0.84	7.43	12.36	14.42
3.1	321	414.45	0.78	0.89	0.83	7.18	12.75	14.64
3.2	221	290.95	0.76	0.88	0.82	6.95	13.15	14.87
3.3	151	204.79	0.75	0.87	0.81	6.73	13.55	15.13
3.4	96	144.48	0.73	0.86	0.80	6.53	13.96	15.41
3.5	66	102.15	0.71	0.86	0.79	6.33	14.37	15.70
3.6	47	72.34	0.70	0.85	0.77	6.14	14.79	16.02
3.7	32	51.30	0.68	0.84	0.76	5.94	15.22	16.34
3.8	20	36.42	0.67	0.84	0.75	5.75	15.66	16.68
3.9	11	25.88	0.65	0.83	0.74	5.55	16.10	17.03
4.0	4	18.39	0.64	0.82	0.73	5.34	16.56	17.40
4.1	2	13.07	0.62	0.81	0.72	5.12	17.01	17.77
4.2	1	9.28	0.61	0.81	0.71	4.89	17.48	18.15
4.3	0	6.58	0.59	0.80	0.70	4.64	17.96	18.55
4.4	0	4.66	0.58	0.79	0.69	4.37	18.44	18.95
4.5	0	3.28	0.56	0.79	0.67	4.08	18.93	19.37
4.6	0	2.31	0.55	0.78	0.66	3.78	19.44	19.80
4.7	0	1.61	0.53	0.77	0.65	3.45	19.95	20.24
4.8	0	1.11	0.52	0.77	0.64	3.10	20.47	20.70
4.9	0	0.76	0.51	0.76	0.63	2.72	20.99	21.17
5.0	0	0.50	0.50	0.76	0.63	2.33	21.53	21.66

Table 4.6: Number of entries for the data and uncorrected background ($B_{\text{uncorr.}}$), are shown for the jet multiplicity $N \geq 3$. The correction factors based on PYTHIA8 MC (CF^{P}), HERWIG++ MC (CF^{H}) and both the MCs (CF^{MC}), are shown corresponding to the minimum H_T thresholds ($H_T^{\min}$). The uncertainties (statistical $\Delta B_{\text{corr.}}^{\text{stat.}}$, systematic $\Delta B_{\text{corr.}}^{\text{stat.}}$ and total $\Delta B_{\text{corr.}}^{\text{tot.}}$) due to the correction factor CF^{MC}, are also shown for each $H_T^{\min}$.

$H_T^{\min}$	Data	$B_{\text{uncorr.}}$	CF^{P}	CF^{H}	CF^{MC}	$\Delta B_{\text{corr.}}^{\text{stat.}}$ (%)	$\Delta B_{\text{corr.}}^{\text{syst.}}$ (%)	$\Delta B_{\text{corr.}}^{\text{tot.}}$ (%)
2.4	3121	3590.82	0.88	0.94	0.91	11.23	12.85	17.07
2.5	2061	2452.80	0.86	0.93	0.89	10.78	13.32	17.14
2.6	1398	1683.72	0.84	0.92	0.88	10.36	13.80	17.25
2.7	928	1161.08	0.82	0.91	0.87	9.96	14.28	17.42
2.8	648	804.06	0.80	0.90	0.85	9.59	14.78	17.62
2.9	433	558.98	0.78	0.90	0.84	9.25	15.28	17.86
3.0	290	389.99	0.77	0.89	0.83	8.92	15.80	18.14
3.1	206	272.98	0.75	0.88	0.81	8.62	16.32	18.46
3.2	139	191.63	0.73	0.87	0.80	8.34	16.86	18.81
3.3	96	134.89	0.71	0.86	0.79	8.07	17.40	19.18
3.4	62	95.17	0.69	0.85	0.77	7.81	17.96	19.58
3.5	40	67.28	0.67	0.85	0.76	7.57	18.52	20.01
3.6	25	47.65	0.65	0.84	0.75	7.33	19.10	20.46
3.7	17	33.79	0.64	0.83	0.73	7.09	19.69	20.93
3.8	9	23.99	0.62	0.82	0.72	6.85	20.30	21.42
3.9	4	17.04	0.60	0.81	0.71	6.61	20.91	21.93
4.0	1	12.11	0.58	0.81	0.69	6.36	21.54	22.46
4.1	0	8.61	0.56	0.80	0.68	6.09	22.18	23.00
4.2	0	6.11	0.54	0.79	0.67	5.81	22.84	23.56
4.3	0	4.33	0.53	0.78	0.65	5.51	23.50	24.14
4.4	0	3.07	0.51	0.77	0.64	5.19	24.19	24.74
4.5	0	2.16	0.49	0.77	0.63	4.85	24.89	25.36
4.6	0	1.52	0.48	0.76	0.62	4.48	25.60	25.99
4.7	0	1.06	0.46	0.75	0.61	4.09	26.34	26.65
4.8	0	0.73	0.44	0.74	0.59	3.67	27.08	27.33
4.9	0	0.50	0.43	0.74	0.58	3.23	27.85	28.04
5.0	0	0.33	0.42	0.73	0.57	2.76	28.63	28.77

Table 4.7: Number of entries for the data and uncorrected background ($B_{\text{uncorr.}}$), are shown for the jet multiplicity $N \geq 4$. The correction factors based on PYTHIA8 MC (CF^{P}), HERWIG++ MC (CF^{H}) and both the MCs (CF^{MC}), are shown corresponding to the minimum H_T thresholds ($H_T^{\min}$). The uncertainties (statistical $\Delta B_{\text{corr.}}^{\text{stat.}}$, systematic $\Delta B_{\text{corr.}}^{\text{stat.}}$ and total $\Delta B_{\text{corr.}}^{\text{tot.}}$) due to the correction factor CF^{MC}, are also shown for each $H_T^{\min}$.

$H_T^{\min}$	Data	$B_{\text{uncorr.}}$	CF^{P}	CF^{H}	CF^{MC}	$\Delta B_{\text{corr.}}^{\text{stat.}}$ (%)	$\Delta B_{\text{corr.}}^{\text{syst.}}$ (%)	$\Delta B_{\text{corr.}}^{\text{tot.}}$ (%)
2.4	1675	1915.29	0.88	0.96	0.92	14.44	16.25	21.74
2.5	1134	1308.28	0.86	0.95	0.90	13.86	16.85	21.82
2.6	770	898.07	0.84	0.94	0.89	13.31	17.46	21.96
2.7	500	619.30	0.81	0.93	0.87	12.80	18.09	22.16
2.8	345	428.87	0.79	0.92	0.86	12.31	18.73	22.41
2.9	230	298.15	0.77	0.91	0.84	11.86	19.38	22.72
3.0	156	208.02	0.75	0.90	0.83	11.43	20.04	23.07
3.1	106	145.60	0.73	0.89	0.81	11.03	20.73	23.48
3.2	75	102.21	0.71	0.89	0.80	10.65	21.42	23.93
3.3	50	71.95	0.68	0.88	0.78	10.30	22.13	24.41
3.4	31	50.76	0.66	0.87	0.77	9.96	22.86	24.94
3.5	19	35.89	0.64	0.86	0.75	9.63	23.61	25.50
3.6	12	25.41	0.62	0.85	0.74	9.32	24.37	26.09
3.7	9	18.02	0.60	0.84	0.72	9.01	25.15	26.72
3.8	5	12.80	0.58	0.83	0.71	8.70	25.96	27.37
3.9	3	9.09	0.56	0.82	0.69	8.38	26.78	28.06
4.0	1	6.46	0.54	0.82	0.68	8.05	27.62	28.77
4.1	0	4.59	0.52	0.81	0.66	7.71	28.48	29.50
4.2	0	3.26	0.50	0.80	0.65	7.34	29.36	30.27
4.3	0	2.31	0.48	0.79	0.63	6.96	30.27	31.06
4.4	0	1.64	0.46	0.78	0.62	6.55	31.20	31.88
4.5	0	1.15	0.44	0.77	0.61	6.12	32.15	32.73
4.6	0	0.81	0.42	0.77	0.59	5.65	33.13	33.61
4.7	0	0.56	0.40	0.76	0.58	5.16	34.14	34.52
4.8	0	0.39	0.38	0.75	0.57	4.63	35.17	35.47
4.9	0	0.27	0.36	0.74	0.55	4.07	36.23	36.46
5.0	0	0.18	0.35	0.74	0.54	3.48	37.32	37.49

Table 4.8: Number of entries for the data and uncorrected background ($B_{\text{uncorr.}}$), are shown for the jet multiplicity $N \geq 5$. The correction factors based on PYTHIA8 MC (CF^{P}), HERWIG++ MC (CF^{H}) and both the MCs (CF^{MC}), are shown corresponding to the minimum H_T thresholds ($H_T^{\min}$). The uncertainties (statistical $\Delta B_{\text{corr.}}^{\text{stat.}}$, systematic $\Delta B_{\text{corr.}}^{\text{stat.}}$ and total $\Delta B_{\text{corr.}}^{\text{tot.}}$) due to the correction factor CF^{MC}, are also shown for each $H_T^{\min}$.

$H_T^{\min}$	Data	$B_{\text{uncorr.}}$	CF^{P}	CF^{H}	CF^{MC}	$\Delta B_{\text{corr.}}^{\text{stat.}}$ (%)	$\Delta B_{\text{corr.}}^{\text{syst.}}$ (%)	$\Delta B_{\text{corr.}}^{\text{tot.}}$ (%)
2.4	764	845.88	0.89	0.99	0.94	21.67	19.62	29.23
2.5	522	577.80	0.87	0.98	0.93	20.77	20.35	29.08
2.6	354	396.63	0.84	0.97	0.91	19.93	21.09	29.02
2.7	233	273.51	0.82	0.96	0.89	19.14	21.85	29.05
2.8	160	189.41	0.79	0.96	0.87	18.39	22.63	29.16
2.9	107	131.68	0.77	0.95	0.86	17.68	23.43	29.35
3.0	65	91.87	0.74	0.94	0.84	17.02	24.25	29.62
3.1	44	64.30	0.72	0.93	0.82	16.40	25.08	29.97
3.2	27	45.14	0.70	0.92	0.81	15.82	25.94	30.38
3.3	19	31.77	0.67	0.91	0.79	15.27	26.82	30.86
3.4	11	22.42	0.65	0.90	0.77	14.74	27.73	31.40
3.5	8	15.85	0.62	0.89	0.76	14.24	28.65	32.00
3.6	4	11.22	0.60	0.88	0.74	13.76	29.61	32.65
3.7	3	7.96	0.58	0.87	0.72	13.28	30.58	33.34
3.8	1	5.65	0.55	0.86	0.71	12.81	31.59	34.08
3.9	1	4.02	0.53	0.85	0.69	12.33	32.62	34.87
4.0	0	2.85	0.51	0.84	0.67	11.83	33.68	35.70
4.1	0	2.03	0.48	0.83	0.66	11.32	34.77	36.57
4.2	0	1.44	0.46	0.82	0.64	10.79	35.89	37.48
4.3	0	1.02	0.44	0.81	0.62	10.22	37.05	38.43
4.4	0	0.72	0.41	0.80	0.61	9.62	38.24	39.43
4.5	0	0.51	0.39	0.80	0.59	8.98	39.46	40.47
4.6	0	0.36	0.37	0.79	0.58	8.30	40.73	41.56
4.7	0	0.25	0.35	0.78	0.56	7.57	42.03	42.71
4.8	0	0.17	0.33	0.77	0.55	6.80	43.37	43.90
4.9	0	0.12	0.31	0.76	0.54	5.98	44.76	45.16
5.0	0	0.08	0.29	0.76	0.52	5.11	46.19	46.47

Table 4.9: Number of entries for the data and uncorrected background ($B_{\text{uncorr.}}$), are shown for the jet multiplicity $N \geq 6$. The correction factors based on PYTHIA8 MC (CF^{P}), HERWIG++ MC (CF^{H}) and both the MCs (CF^{MC}), are shown corresponding to the minimum H_T thresholds ($H_T^{\min}$). The uncertainties (statistical $\Delta B_{\text{corr.}}^{\text{stat.}}$, systematic $\Delta B_{\text{corr.}}^{\text{stat.}}$ and total $\Delta B_{\text{corr.}}^{\text{tot.}}$) due to the correction factor CF^{MC}, are also shown for each $H_T^{\min}$.

$H_T^{\min}$	Data	$B_{\text{uncorr.}}$	CF^{P}	CF^{H}	CF^{MC}	$\Delta B_{\text{corr.}}^{\text{stat.}}$ (%)	$\Delta B_{\text{corr.}}^{\text{syst.}}$ (%)	$\Delta B_{\text{corr.}}^{\text{tot.}}$ (%)
2.4	296	308.81	0.92	1.07	0.99	36.96	23.02	43.54
2.5	196	210.94	0.89	1.06	0.98	35.37	23.82	42.64
2.6	138	144.80	0.86	1.05	0.96	33.87	24.64	41.88
2.7	86	99.85	0.84	1.04	0.94	32.45	25.48	41.26
2.8	62	69.15	0.81	1.03	0.92	31.11	26.35	40.77
2.9	44	48.07	0.78	1.01	0.90	29.85	27.23	40.41
3.0	24	33.54	0.76	1.00	0.88	28.67	28.14	40.18
3.1	18	23.48	0.73	0.99	0.86	27.56	29.08	40.06
3.2	10	16.48	0.70	0.98	0.84	26.51	30.04	40.06
3.3	7	11.60	0.68	0.97	0.82	25.52	31.02	40.17
3.4	3	8.18	0.65	0.96	0.80	24.59	32.04	40.39
3.5	2	5.79	0.62	0.95	0.79	23.70	33.08	40.69
3.6	2	4.10	0.60	0.94	0.77	22.84	34.15	41.09
3.7	2	2.91	0.57	0.93	0.75	22.01	35.26	41.56
3.8	1	2.06	0.55	0.92	0.73	21.19	36.39	42.11
3.9	1	1.47	0.52	0.90	0.71	20.37	37.57	42.73
4.0	0	1.04	0.49	0.89	0.69	19.53	38.77	43.42
4.1	0	0.74	0.47	0.88	0.68	18.67	40.02	44.16
4.2	0	0.53	0.44	0.87	0.66	17.78	41.30	44.97
4.3	0	0.37	0.42	0.86	0.64	16.84	42.63	45.83
4.4	0	0.26	0.39	0.85	0.62	15.85	43.99	46.76
4.5	0	0.19	0.37	0.84	0.61	14.79	45.41	47.76
4.6	0	0.13	0.35	0.83	0.59	13.67	46.87	48.82
4.7	0	0.09	0.32	0.82	0.57	12.48	48.38	49.96
4.8	0	0.06	0.30	0.81	0.56	11.21	49.94	51.19
4.9	0	0.04	0.28	0.81	0.54	9.86	51.56	52.50
5.0	0	0.03	0.26	0.80	0.53	8.44	53.24	53.90

Table 4.10: Number of entries for the data and uncorrected background ($B_{\text{uncorr.}}$), are shown for the jet multiplicity $N \geq 7$. The correction factors based on PYTHIA8 MC (CF^{P}), HERWIG++ MC (CF^{H}) and both the MCs (CF^{MC}), are shown corresponding to the minimum H_T thresholds ($H_T^{\min}$). The uncertainties (statistical $\Delta B_{\text{corr.}}^{\text{stat.}}$, systematic $\Delta B_{\text{corr.}}^{\text{stat.}}$ and total $\Delta B_{\text{corr.}}^{\text{tot.}}$) due to the correction factor CF^{MC}, are also shown for each $H_T^{\min}$.

4.6.2 Choice of Normalisation Region

The ansatz function $f(x)$ is only used for the baseline case of multiplicity two. For all other multiplicities, $N > 2$, the same function is normalized to determine the number of background events in the signal region, i.e. $f^{N>2}(x) = n_f^{\text{nom.}} f(x)$ (shown in equation 4.6). The nominal normalisation factor $n_f^{\text{nom.}}$ measured in the normalisation region is used to normalize the $f(x)$ to the $f^{N>2}(x)$. The sensitivity of the normalisation factor has been studied by sliding the upper and lower boundaries of the nominal normalisation region by 0.1 TeV on either side. The normalisation factor n_f is measured in different normalisation ranges and compared with the $n_f^{\text{nom.}}$. The normalisation factor n_f corresponding to any normalisation region is defined as

$$n_f = \frac{n_f^{\text{num.}}}{n_f^{\text{den.}}}, \tag{4.12}$$

where $n_f^{\text{num.}}$ and $n_f^{\text{den.}}$ are the numerator and denominator of n_f corresponding to any normalisation region (NR) and defined as

$$n_f^{\text{num.}} = \sum_{H_T \epsilon NR}^{N>2} H_T \quad \text{and} \quad n_f^{\text{den.}} = \sum_{H_T \epsilon NR}^{N=2} H_T. \tag{4.13}$$

The statistical uncertainty ($\Delta n_f^{\text{stat.}}$) for the normalisation factor n_f can be written as

$$\Delta n_f^{\text{stat.}} = n_f \sqrt{\frac{1}{n_f^{\text{num.}}} + \frac{1}{n_f^{\text{den.}}}}, \tag{4.14}$$

whereas the systematic uncertainty ($\Delta n_f^{\text{syst.}}$) corresponding to n_f is written as

$$\Delta n_f^{\text{syst.}} = \left| n_f^{\text{nom.}} - n_f \right|. \tag{4.15}$$

The total uncertainty due to the choice of the normalisation region can be written as

$$\Delta n_f(\%) = \frac{1}{n_f^{\text{nom.}}} \left[\sqrt{(\Delta n_f^{\text{stat.}})^2 + (\Delta n_f^{\text{syst.}})^2} \right] \times 100. \tag{4.16}$$

In Table 4.11, the statistical uncertainty $\Delta n_f^{\text{stat.}}$, systematic uncertainty $\Delta n_f^{\text{syst.}}$ and the total uncertainty (Δn_f) due to the choice of the normalisation region are shown for inclusive jet multiplicities. In order to compensate the uncertainties from all the possible choices of the normalisation region, the maximum Δn_f is chosen for the limit calculations. Typically this uncertainty remains less than 3%.

4.6.3 Jet Energy Uncertainties

The jet energy measured in the ATLAS calorimeters is corrected because of the non-compensating response of the calorimeters [87] and energy losses in the bad calorimeter regions (as discussed in Appendix A). The correction is called as jet energy scale (JES) [86]. Due to limited resolution of the detector, the effect of jet energy resolution (JER) is also measured by using some dedicated analyses, as discussed in Ref. [85]. The uncertainties on the JES and JER are also calculated in Ref. [85, 86]. In this analysis, the uncertainties due to the JES and JER uncertainties are measured and collectively referred to as the jet energy uncertainties. The JER uncertainty depends on pseudorapidity, transverse momentum, transverse energy and azimuthal angle. The JES uncertainty also depends on the same variables but, in addition, it uses the number of primary vertices (NPV) and average number of interactions per bunch crossing (μ) variables in order to take the pileup uncertainty effects into account. The effects of both uncertainties on the H_T distributions are computed using data, for each jet multiplicity and as a function of H_T^{min}.

In order to estimate the effect of the JES uncertainty, the p_T of all the jets are modified by the JES uncertainty and the H_T distribution is recomputed. Since the exclusion limits in this study are calculated on the basis of counting experiments[2], the effects of JES uncertainty in the

[2] The number of data events are counted for each H_T^{min}.

H_T Ratio	$n_f^{\text{nom.}}$	normalisation region (NR) [TeV]	n_f	$\Delta n_f^{\text{stat.}}$	$\Delta n_f^{\text{syst.}}$	$\Delta n_f^{\text{total}}(\%)$
$H_{T_{32}}^{\text{inl}}$	4.606	1.6 − 2.3	4.672	0.030	0.065	1.559
		1.6 − 2.4	4.668	0.029	0.061	1.477
		1.6 − 2.5	4.662	0.029	0.056	1.364
		1.7 − 2.3	4.612	0.037	0.005	0.807
		1.7 − 2.5	4.598	0.036	0.008	0.804
		1.8 − 2.3	4.561	0.046	0.045	1.395
		1.8 − 2.4	4.554	0.045	0.052	1.491
		1.8 − 2.5	4.543	0.045	0.063	1.684
$H_{T_{42}}^{\text{inl}}$	3.034	1.6 − 2.3	3.064	0.020	0.030	1.205
		1.6 − 2.4	3.061	0.020	0.027	1.122
		1.6 − 2.5	3.058	0.020	0.024	1.021
		1.7 − 2.3	3.038	0.025	0.004	0.847
		1.7 − 2.5	3.028	0.025	0.006	0.840
		1.8 − 2.3	3.008	0.032	0.026	1.347
		1.8 − 2.4	3.002	0.031	0.032	1.461
		1.8 − 2.5	2.994	0.031	0.040	1.654
$H_{T_{52}}^{\text{inl}}$	1.618	1.6 − 2.3	1.625	0.012	0.006	0.833
		1.6 − 2.4	1.622	0.012	0.004	0.771
		1.6 − 2.5	1.621	0.012	0.003	0.741
		1.7 − 2.3	1.622	0.015	0.004	0.948
		1.7 − 2.5	1.616	0.015	0.002	0.917
		1.8 − 2.3	1.615	0.019	0.003	1.170
		1.8 − 2.4	1.610	0.018	0.008	1.243
		1.8 − 2.5	1.606	0.018	0.012	1.339
$H_{T_{62}}^{\text{inl}}$	0.715	1.6 − 2.3	0.713	0.006	0.002	0.925
		1.6 − 2.4	0.712	0.006	0.003	0.959
		1.6 − 2.5	0.712	0.006	0.003	0.981
		1.7 − 2.3	0.716	0.008	0.001	1.139
		1.7 − 2.5	0.714	0.008	0.001	1.107
		1.8 − 2.3	0.722	0.010	0.007	1.728
		1.8 − 2.4	0.719	0.010	0.005	1.541
		1.8 − 2.5	0.718	0.010	0.003	1.462
$H_{T_{72}}^{\text{inl}}$	0.261	1.6 − 2.3	0.260	0.003	0.001	1.355
		1.6 − 2.4	0.260	0.003	0.001	1.337
		1.6 − 2.5	0.259	0.003	0.001	1.371
		1.7 − 2.3	0.261	0.004	0.000	1.591
		1.7 − 2.5	0.260	0.004	0.000	1.572
		1.8 − 2.3	0.265	0.005	0.004	2.658
		1.8 − 2.4	0.265	0.005	0.005	2.639
		1.8 − 2.5	0.265	0.005	0.004	2.438

Table 4.11: Statistical uncertainty ($\Delta n_f^{\text{stat.}}$), systematic uncertainty ($\Delta n_f^{\text{syst.}}$) and total uncertainty (Δn_f) due to the choice of the normalisation region for inclusive H_T ratios ($H_{T_{i2}}^{\text{inl}}$), i.e. the ratios of the inclusive multiplicities $i = N \geq 3, 4, ..., 7$ with respect to the reference jet multiplicity $N = 2$. The normalisation factor ($n_f^{\text{nom.}}$) corresponds to the nominal normalisation range, $1.7 < H_T < 2.4$ TeV.

jet p_T are assumed to be propagated in the modified H_T. For each bin of $H_T^{\rm min}$, the difference between the modified H_T distribution ($H_T^{\rm JES}$) and the nominal H_T distribution ($H_T^{\rm nom}$) is used to define the systematic uncertainty (ΔJES), i.e.,

$$\Delta\text{JES} = \frac{H_T^{\rm JES} - H_T^{\rm nom}}{H_T^{\rm nom}}. \tag{4.17}$$

To quantify the effects of the JER uncertainty on the H_T distribution, the jet p_T resolution is smeared according to the JER uncertainty by generating five hundred pseudo datasets. The difference between the H_T distributions constructed from the datasets ($H_T^{\rm JER_1}, H_T^{\rm JER_2}, ..., H_T^{\rm JER_{500}}$) and the $H_T^{\rm nom}$, on bin-by-bin basis, is used to define quantities ΔJER_1, ΔJER_2,...,ΔJER_{500}, i.e.,

$$\Delta\text{JER}_i = \frac{H_T^{\rm JER_i} - H_T^{\rm nom}}{H_T^{\rm nom}}, \tag{4.18}$$

where $i = 1, 2, ..., 500$ is an integer index corresponding to the dataset number. The final systematic uncertainty due to effects of JER uncertainty is defined from the mean and root mean square values of the gaussian distribution of ΔJER_i. The ΔJER_i gaussian distributions in different $H_T^{\rm min}$ bins, for the jet multiplicity $N \geq 3$, are shown as representative cases in Figure 4.17.

Typically, the effect of JER uncertainty is $1 - 3\%$, whereas the effect of JES uncertainty remains $3 - 5\%$, depending on the $H_T^{\rm min}$ for the signal region and the jet multiplicity. The overall jet energy uncertainty is obtained by adding JER and JES uncertainties in quadrature. The effect of jet energy uncertainties on the background estimation remains smaller as compared to the uncertainty due to corrections to non-invariance in H_T with jet multiplicity.

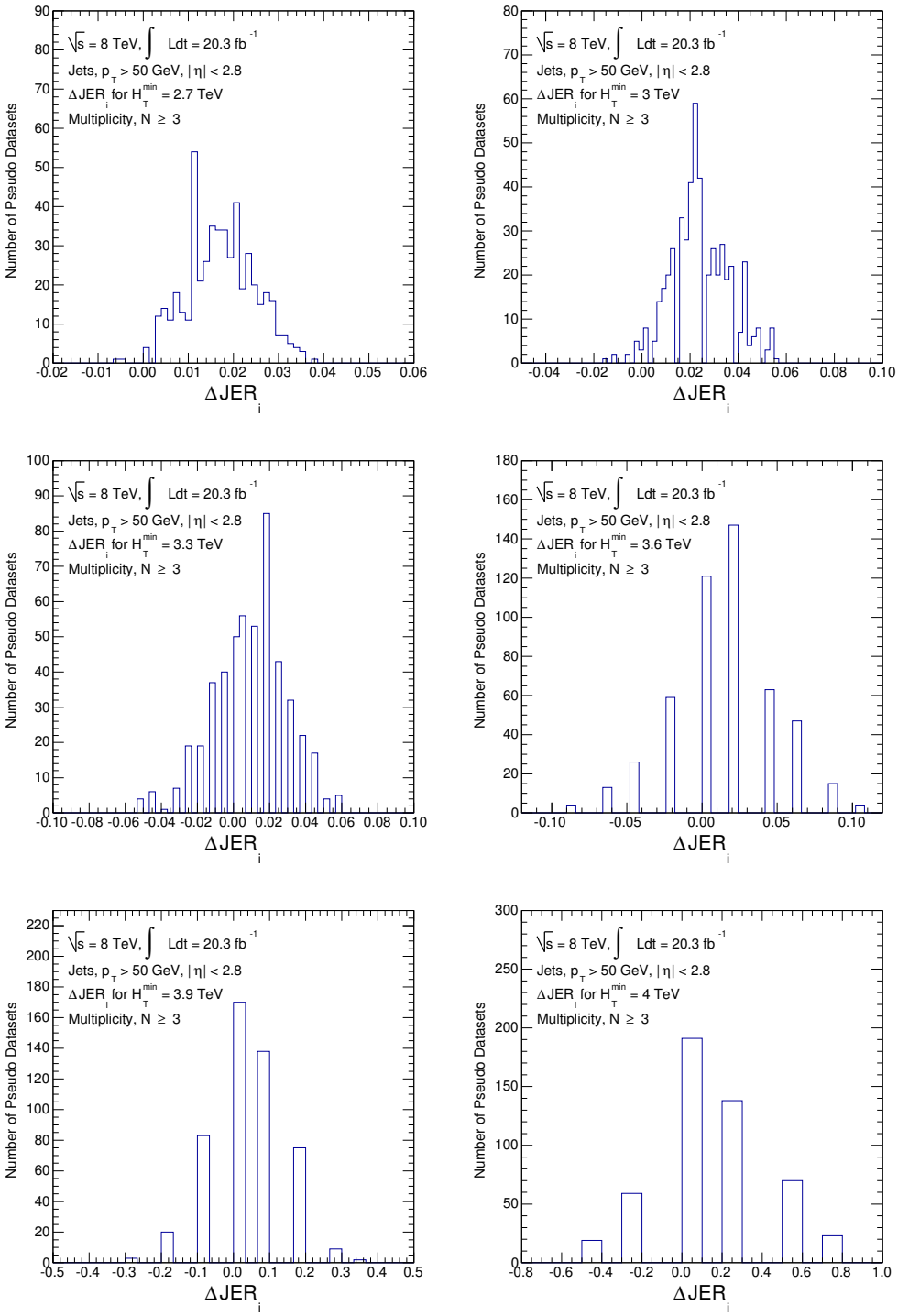

Figure 4.17: The $\Delta\text{JER}_i = \frac{H_T^{\text{JER}_i} - H_T^{\text{nom}}}{H_T^{\text{nom}}}$ gaussian distributions of five hundred pseudo datasets, i.e., $i = 1, 2, .., 500$, corresponding to $H_T^{\text{min}} = 2.7, 3.0, 3.3, 3.6, 3.9, 4.0$ TeV, for the jet multiplicities $N \geq 3$, are shown for the ATLAS 2012 data. For a given pseudo dataset i, the H_T distribution with the effect of jet energy resolution (JER) uncertainty is defined as $H_T^{\text{JER}_i}$, whereas the nominal H_T distribution is defined as H_T^{nom}.

4.6.4 Summary of Systematics

In this subsection, all the systematic uncertainties described in the previous three subsections are summarized. For the inclusive jet multiplicities $N \geq 3, 4, ..., 7$, the data and estimated background along with the total uncertainty are shown in Figure 4.18, as a function of $H_T^{\min}$. For each multiplicity, the uncertainty band due to all the systematics, at the each $H_T^{\min}$, is obtained by adding all the uncertainties in quadrature. The different uncertainties may increase or decrease the estimated background, producing an asymmetric uncertainty band, as shown in Figure 4.18.

From Figure 4.18, the total uncertainty to the background estimation increases with the decreasing statistics with decreasing $H_T^{\min}$ and from one inclusive multiplicity case to the higher one. Therefore, the lowest statistics case, i.e. $N \geq 7$ (the highest inclusive multiplicity in this study), has larger uncertainties than the other multiplicities corresponding to the same $H_T^{\min}$ values. The shape invariance is also affected by statistics, therefore, the contribution of uncertainty due to non-invariance is dominant in the low statistics region. As a result, the larger overestimation of the background is observed in the high $H_T^{\min}$ region. Similarly, for a given $H_T^{\min}$, the overestimation of the background increases from a lower multiplicity to the higher one. The uncertainty due to the choice of the normalisation region has a constant effect along the whole range of the $H_T^{\min}$ (as discussed in subsection 4.6.2), for any inclusive multiplicity. Finally, the jet energy uncertainties contribute significantly in the overall band of total uncertainty, and also increase with the increase in $H_T^{\min}$.

For $N \geq 3$, $N \geq 4$ and $N \geq 5$, the amount of total uncertainty typically remains in the 15-35% and 35-70% ranges, in the $2.4 < H_T^{\min} \leq 3.5$ TeV and $3.6 < H_T^{\min} \leq 4.5$ TeV regions, respectively. For higher inclusive cases, i.e. $N \geq 6$ and $N \geq 7$, the amount of total uncertainties typically

lies in the 30-50% and 50-70% ranges, in the $2.4 < H_T^{\min} \leq 3.5$ TeV and $3.6 < H_T^{\min} \leq 4.5$ TeV regions, respectively. For the $H_T^{\min} > 4.5$ TeV region, all the multiplicities have a total uncertainty in the 75-100% range.

The plots in Figure 4.18 as a function of $H_T^{\min}$ indicate an accumulative representation of the data and estimated background from the plots shown in Figure 4.16. The data points, from Figure 4.16, fluctuate above and below the estimated background whereas they are always below the estimated background in Figure 4.18. Therefore, another way to visualize the data and estimated background, as a function of $H_T^{\min}$, is shown in Figure 4.19. In this figure, the accumulated background shown for different inclusive multiplicities is estimated by excluding the background from the empty data-bins. In this representation, the data and background agreement is improved as compared to shown in Figure 4.18.

There is no excess of data events found above the estimated background, therefore, model-inpedent and mode-dependent exclusion limits are set at the 95% confidence level (CL). The data and background shown in Figure 4.18 are within one sigma uncertainty. The one sigma agreement can also be seen later from the model-independent exclusion limits. Moreover, the exclusion limits are set in the high H_T region, i.e., including the region with empty data bins, therefore, the results obtained from Figure 4.18 are used for calculating limits.

4.7 Exclusion Limits

The exclusion limits are calculated as a function of $H_T^{\min}$ for the inclusive jet multiplicities. In the signal region, different $H_T > H_T^{\min}$ values are chosen and counting experiments are performed as a function of $H_T^{\min}$. The upper limits are calculated by using a frequentist CL_s method [88, 89]. Exclusion limits on the production of new physics and black holes are set by taking

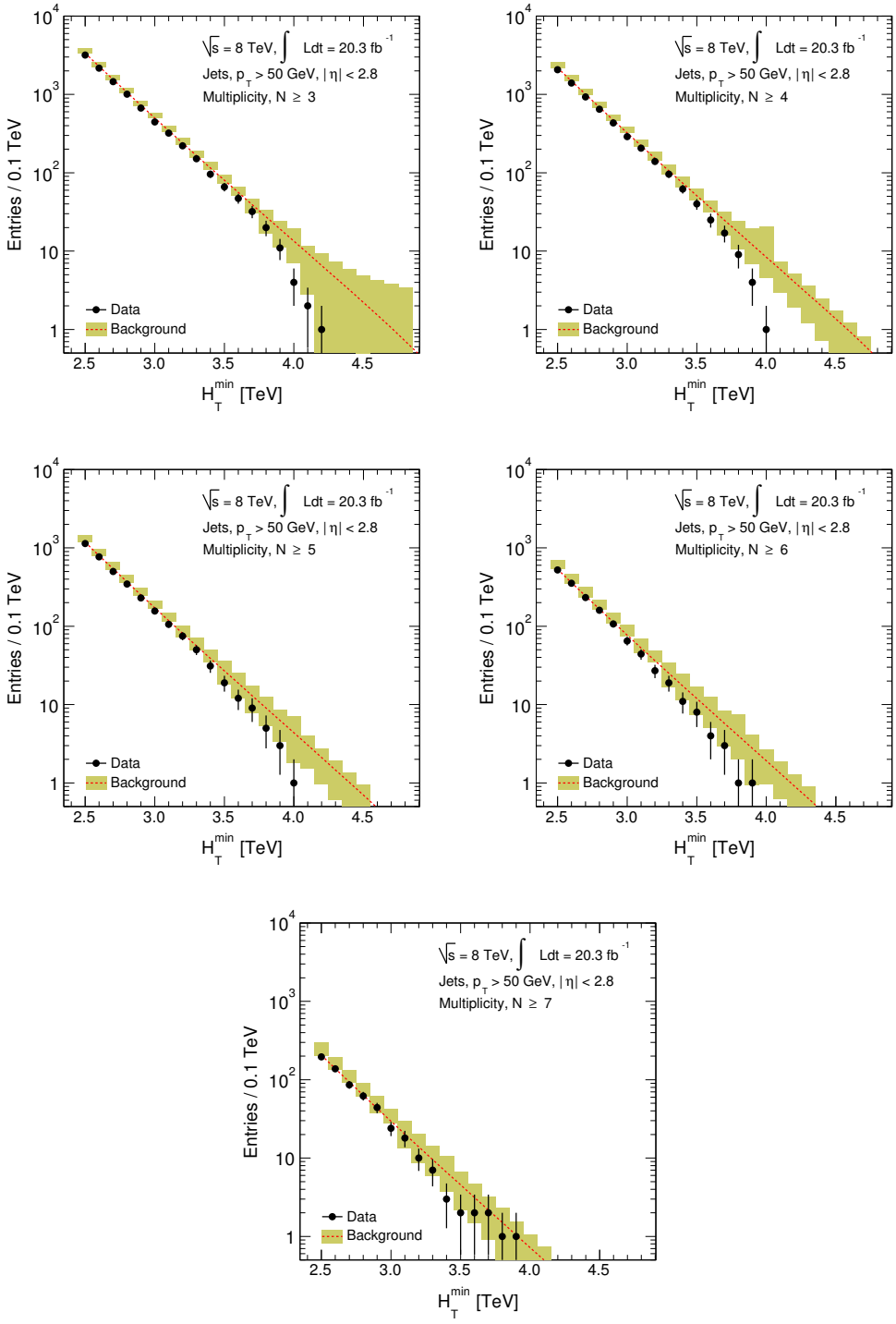

Figure 4.18: The $H_T^{\min}$ distributions, for the inclusive jet multiplicities $N \geq 3, 4, ..., 7$, are shown for the ATLAS 2012 data and predicted background along with total uncertainty.

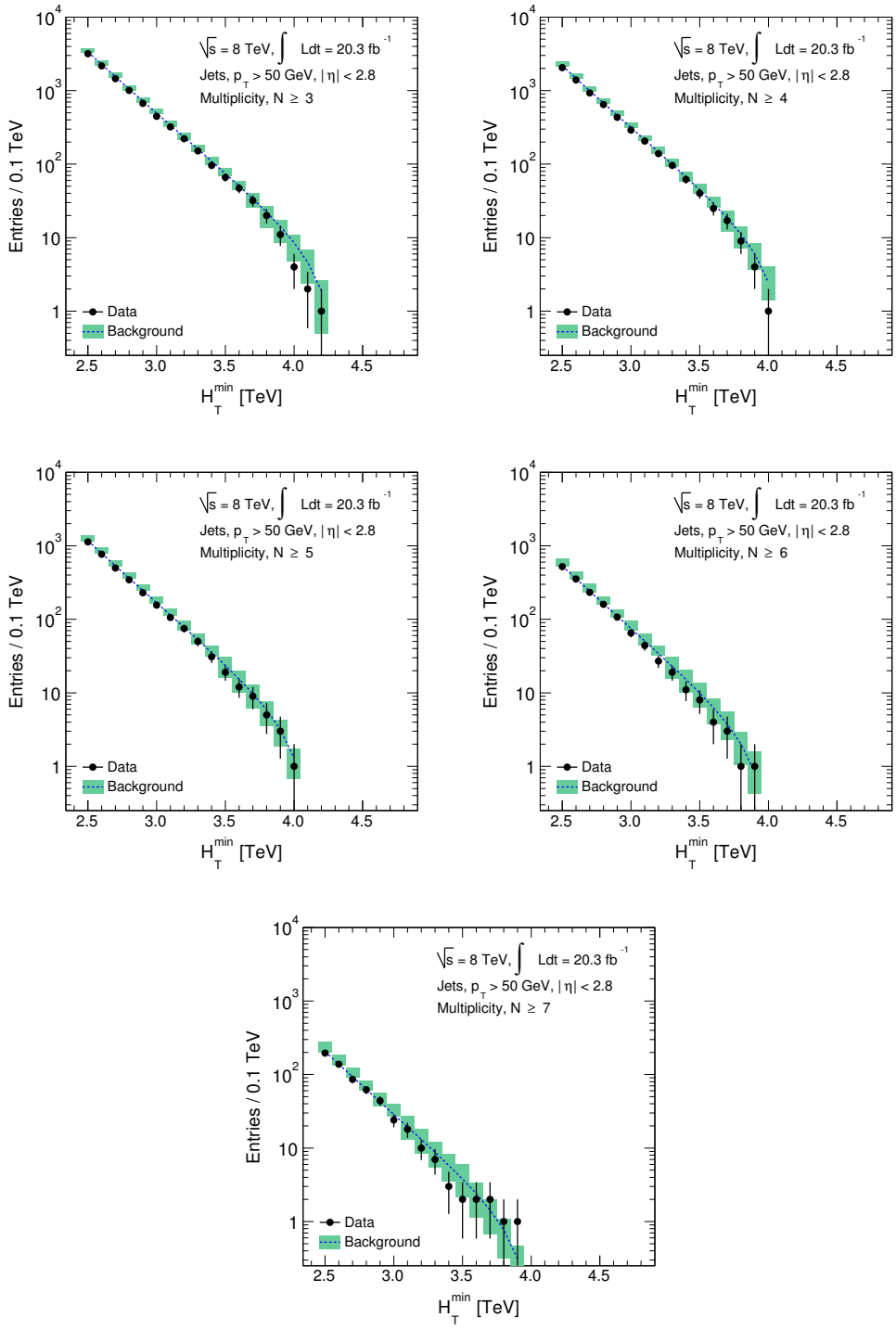

Figure 4.19: The $H_T^{\min}$ distributions, for the inclusive jet multiplicities $N \geq 3, 4, ..., 7$, are shown for the ATLAS 2012 data and predicted background along with total uncertainty. The background is estimated by dropping the empty data bins in the H_T distributions.

all the three types of systematic uncertainties described in section 4.6 into account. The 2.8% luminosity uncertainty is also used in the upper limit calculations. The model-independent upper limits are shown in the next subsection.

4.7.1 Model-Independent Limits

Model-independent upper limits are calculated at the 95% CL on cross section times the acceptance for new physics production in the high H_T inclusive multijet final states for $N \geq 2, 3, ..., 7$, as shown in Figure 4.20. These figures show the observed and expected limits along with the one and two standard deviation bands for the expected limits. The observed limits are obtained from the data, whereas the expected limit is the median of the distribution of the limits at the 95% CL generated by pseudo datasets. The pseudo datasets assume a background-only model and are generated by randomly fluctuating the predicted background value. A total of 2500 pseudo datasets are used in this study and an upper limit is calculated for each one of them. Finally, the expected limit is computed by determining the median of the distribution of the upper limits obtained from all the pseudo datasets. The one and two sigma bands are the 68% and 95% confidence intervals around the median value.

The observed limits typically lie below the expected limits within one sigma uncertainty. The exclusion limit on the cross section times acceptance times efficiency[3] is 0.29 fb to 0.14 fb for $N \geq 3$ to $N \geq 7$ for the high-H_T, i.e. $H_T > 4.0$ TeV. The limits as a function of the $H_T^{\min}$ and jet multiplicity are shown in Table 4.12. In order to observe variation of exclusion limits with H_T and multijet final states, upper limits on cross section times acceptance times efficiency at the 95% CL as a function of the inclusive jet multiplicities for fixed $H_T^{\min}$ values, are also shown in Fig-

[3] These are the acceptance and efficiency of the detector.

ure 4.21. For $H_T^{\min} = 2.5, 3.0$ and 3.5 TeV, limits decrease with the increase in jet multiplicity. The $H_T^{\min} = 4.0$ TeV case looks almost flat for $N \geq 4$ and beyond, whereas the $H_T^{\min} = 4.5$ and 5 TeV cases are flat for all the inclusive multijet final states because no data events are in the $H_T > 4.5$ TeV region. Moreover, exclusion limits drop quickly with increasing $H_T^{\min}$ and then are flat for $H_T^{\min} > 4$ TeV. The exclusion limits reported in this study are improved limits as compared to the CMS study for the microscopic black hole searches at $\sqrt{s} = 8$ TeV [9, 10], as shown in Table 4.13[4].

4.7.2 Model-Dependent Limits

The ADD-type of black hole signal samples simulated by the CHARYBDIS2 black hole event generator are used to calculate model-dependent limits. A brief description of the CHARYBDIS2 samples is given below.

CHARYBDIS2 Black Hole Samples

The black hole event generator CHARYBDIS2 version 1.0.4 is used to simulate the production and decay of microscopic black holes in *pp* collisions by using a semi-classical approach in models with flat extra dimensions and TeV-scale gravity. The black hole production is assumed to be a classically-dominated phenomena that occurs at energies well above the fundamental Planck scale. On the other hand, black hole decay is considered to be dominated by quantum effects with the emission of Hawking radiation. The decay process is required to conserve charge and baryon number. The generator is interfaced with PYTHIA8 to incorporate the effects of parton showering, hadronisation and underlying events.

The black hole samples are generated as a function of three parameters, n, M_D and a lower mass threshold to produce black hole (M_{th}). Any two parameters can be fixed to observe the sensitivity of the third param-

[4] In CMS papers, efficiency of detector is merged in the definition of acceptance.

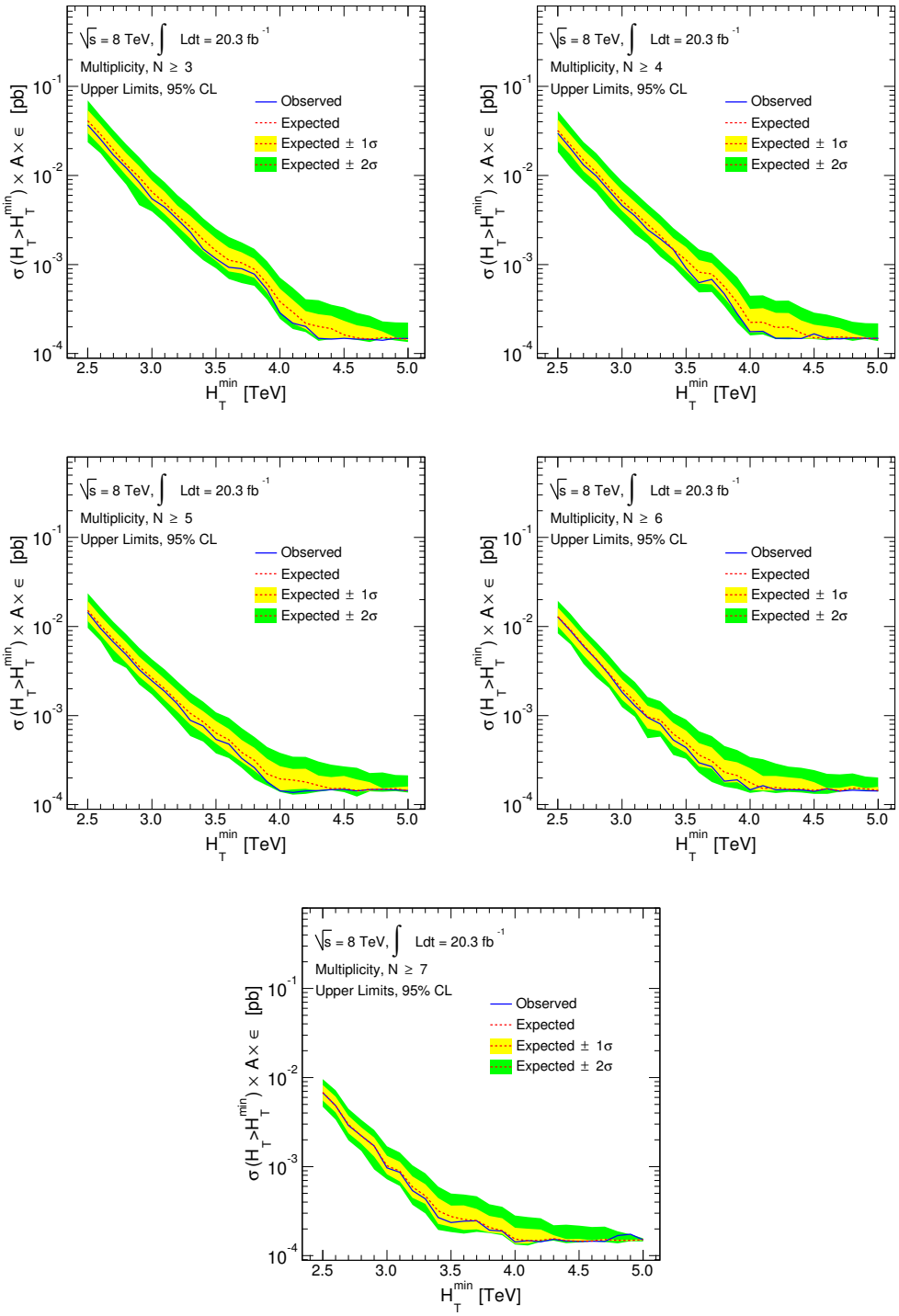

Figure 4.20: Model-independent limits using ATLAS 2012 data, on upper cross section (σ) times acceptance (A) times efficiency (ϵ) at the 95% confidence level (CL) for counting experiments with $H_T > H_T^{\min}$, as a function of $H_T^{\min}$ for inclusive jet multiplicities $N \geq 3, 4, ..., 7$. The blue solid (red dotted) lines correspond to an observed (expected) limit. The yellow and green bands represent one and two sigma standard deviations from the expected limits.

$H_T^{\min}$ (TeV)	Limit (fb)	$N \geq 3$	$N \geq 4$	$N \geq 5$	$N \geq 6$	$N \geq 7$
2.5	obs	36.95	29.84	20.96	12.78	6.77
	exp	41.16	31.95	21.74	12.91	6.83
2.6	obs	25.45	20.02	14.42	8.93	4.84
	exp	28.95	21.81	15.17	9.13	4.83
2.7	obs	16.93	13.10	9.53	6.00	2.91
	exp	19.44	14.86	10.32	6.18	2.97
2.8	obs	12.14	9.86	6.69	4.25	2.22
	exp	13.19	10.85	7.18	4.32	2.21
2.9	obs	8.37	6.74	4.83	2.89	1.71
	exp	9.63	7.37	5.19	2.96	1.70
3.0	obs	5.48	4.61	3.29	1.83	0.97
	exp	6.56	5.18	3.57	1.99	1.02
3.1	obs	4.40	3.53	2.46	1.29	0.86
	exp	4.89	3.82	2.65	1.44	0.89
3.2	obs	3.23	2.47	1.87	0.95	0.54
	exp	3.55	2.83	1.99	0.96	0.59
3.3	obs	2.31	1.94	1.35	0.80	0.44
	exp	2.65	2.11	1.44	0.89	0.47
3.4	obs	1.50	1.48	0.88	0.53	0.27
	exp	1.91	1.48	1.06	0.62	0.32
3.5	obs	1.16	0.91	0.76	0.44	0.24
	exp	1.43	1.13	0.85	0.49	0.27
3.6	obs	0.93	0.63	0.54	0.30	0.24
	exp	1.12	0.82	0.64	0.36	0.26
3.7	obs	0.90	0.68	0.48	0.27	0.25
	exp	1.04	0.78	0.53	0.31	0.25
3.8	obs	0.78	0.47	0.33	0.18	0.19
	exp	0.89	0.56	0.39	0.23	0.21
3.9	obs	0.52	0.28	0.26	0.19	0.19
	exp	0.61	0.38	0.32	0.21	0.19
4.0	obs	0.29	0.18	0.18	0.15	0.14
	exp	0.38	0.22	0.22	0.18	0.15
4.1	obs	0.22	0.18	0.14	0.16	0.15
	exp	0.29	0.23	0.19	0.15	0.15
4.2	obs	0.20	0.15	0.14	0.15	0.14
	exp	0.22	0.20	0.19	0.16	0.15
4.3	obs	0.15	0.15	0.14	0.15	0.15
	exp	0.20	0.20	0.18	0.15	0.16
4.4	obs	0.15	0.15	0.14	0.15	0.15
	exp	0.19	0.17	0.16	0.15	0.15
4.5	obs	0.15	0.17	0.15	0.14	0.14
	exp	0.16	0.15	0.15	0.14	0.15
4.6	obs	0.15	0.15	0.15	0.15	0.15
	exp	0.15	0.15	0.15	0.15	0.15
4.7	obs	0.14	0.15	0.14	0.14	0.14
	exp	0.15	0.15	0.14	0.14	0.15
4.8	obs	0.14	0.15	0.15	0.15	0.17
	exp	0.15	0.15	0.15	0.15	0.15
4.9	obs	0.15	0.15	0.15	0.14	0.17
	exp	0.15	0.15	0.15	0.15	0.15
5.0	obs	0.15	0.15	0.15	0.14	0.15
	exp	0.15	0.15	0.15	0.14	0.15

Table 4.12: Model-independent observed (obs) and expected (exp) upper limits using ATLAS 2012 data, on cross section times acceptance times efficiency at the 95% confidence level (CL) for counting experiments with $H_T > H_T^{\min}$, as a function of $H_T^{\min}$ for inclusive jet multiplicities $N \geq 3, 4, ..., 7$.

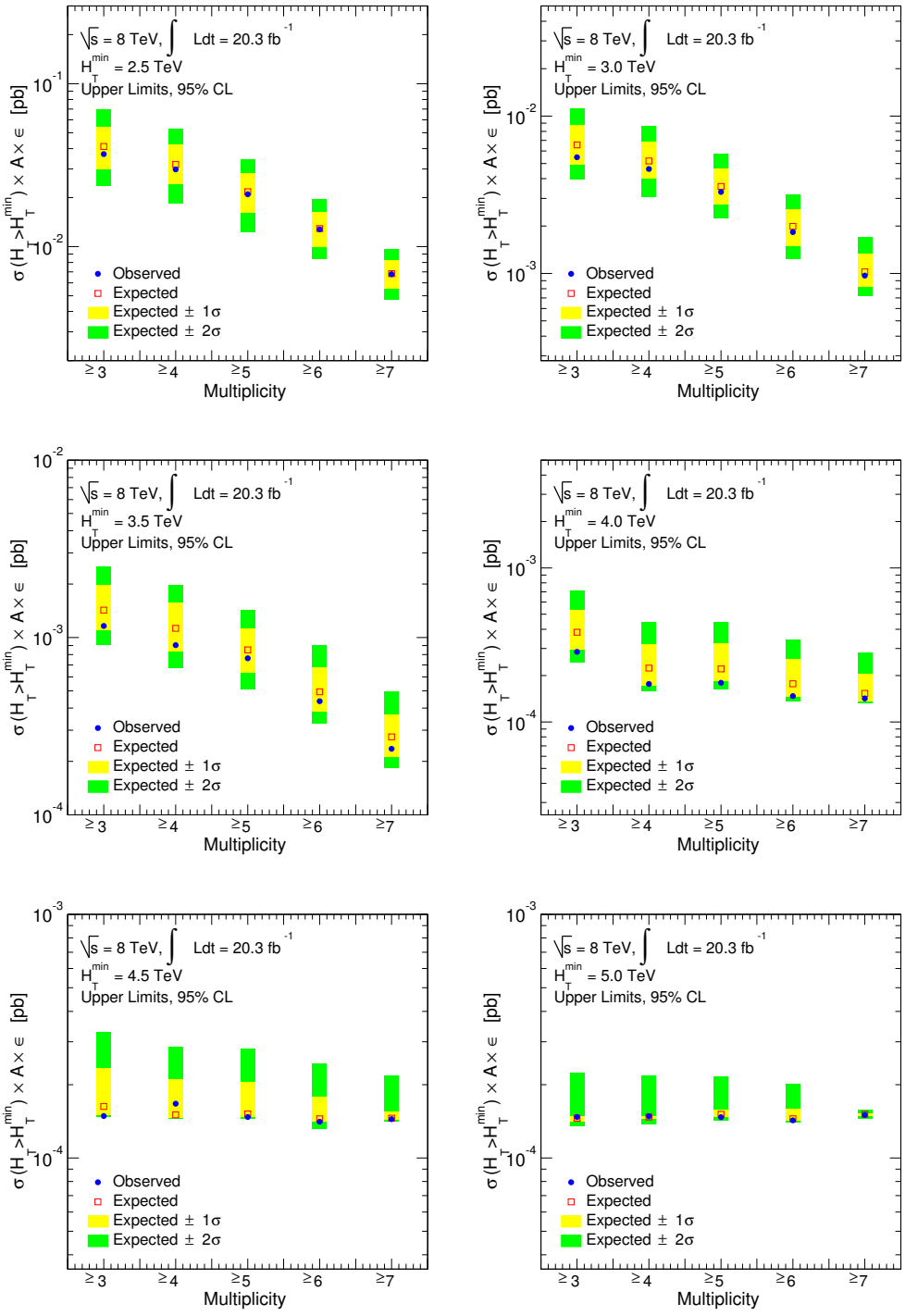

Figure 4.21: Model-independent limits using ATLAS 2012 data, on upper cross section (σ) times acceptance (A) times efficiency (ϵ) with 95% confidence level for counting experiments with $H_T > H_T^{\min}$, as a function of inclusive jet multiplicity corresponding to $H_T^{\min} = 2.5, 3.0, 3.5, 4.0, 4.5$ and 5.0 TeV. The solid blue dots (the empty red squares) correspond to an observed (expected) limit. The yellow and green bands represent one and two sigma standard deviations from the expected limits.

Model-independent upper Limit on $\sigma \times A \times \epsilon$ (fb)		
CMS (for 3.7 fb^{-1})	CMS (for 12.1 fb^{-1})	ATLAS (for 20.3 fb^{-1})
0.70	0.20	0.15

Table 4.13: Model-independent upper limits at the 95% confidence level on cross section (σ) times acceptance (A) times efficiency (ϵ), for the CMS [9, 10] and ATLAS (this study) 2012 data. The limits are shown for the high H_T region, i.e. $H_T > 4.5$ TeV.

eter. As an indicative case, the black hole samples for $M_D = 1.5$ TeV, $M_{\rm th} = 5.5$ TeV and different numbers of extra dimensions n for inclusive jet multiplicities are shown in Figure 4.22. Similarly, the black hole simulations for $M_D = 1.5$ TeV, $n = 6$ and different black hole mass thresholds $M_{\rm th}$ are shown in Figure 4.23.

Limits on Models

The upper limits have been calculated for a variety of models corresponding to different values of n, M_D and $M_{\rm th}$. In order to obtain the upper limits for a signal model, the entire analysis is repeated for that model and the number of signal events are measured as a function of $H_T^{\rm min}$. The uncertainties due to the jet energy uncertainties on the signal MC are very small compared to the uncertainties discussed in subsection 4.6.3 and can be ignored. In addition to the inputs used to calculate the model-independent limits, the number of signal events obtained from a model are used to compute the observed model-dependent upper limits. The upper limits are computed by using the same frequentist CL$_s$ method. The acceptance and efficiency of the detector are already taken into account when a signal sample is passed through all the selection criteria of the analysis, therefore, the model-dependent upper limits are set on cross section σ only. In Figure 4.24, the theoretical values of cross section are also shown with the dotted lines, whereas the experimental values of the upper limits are shown

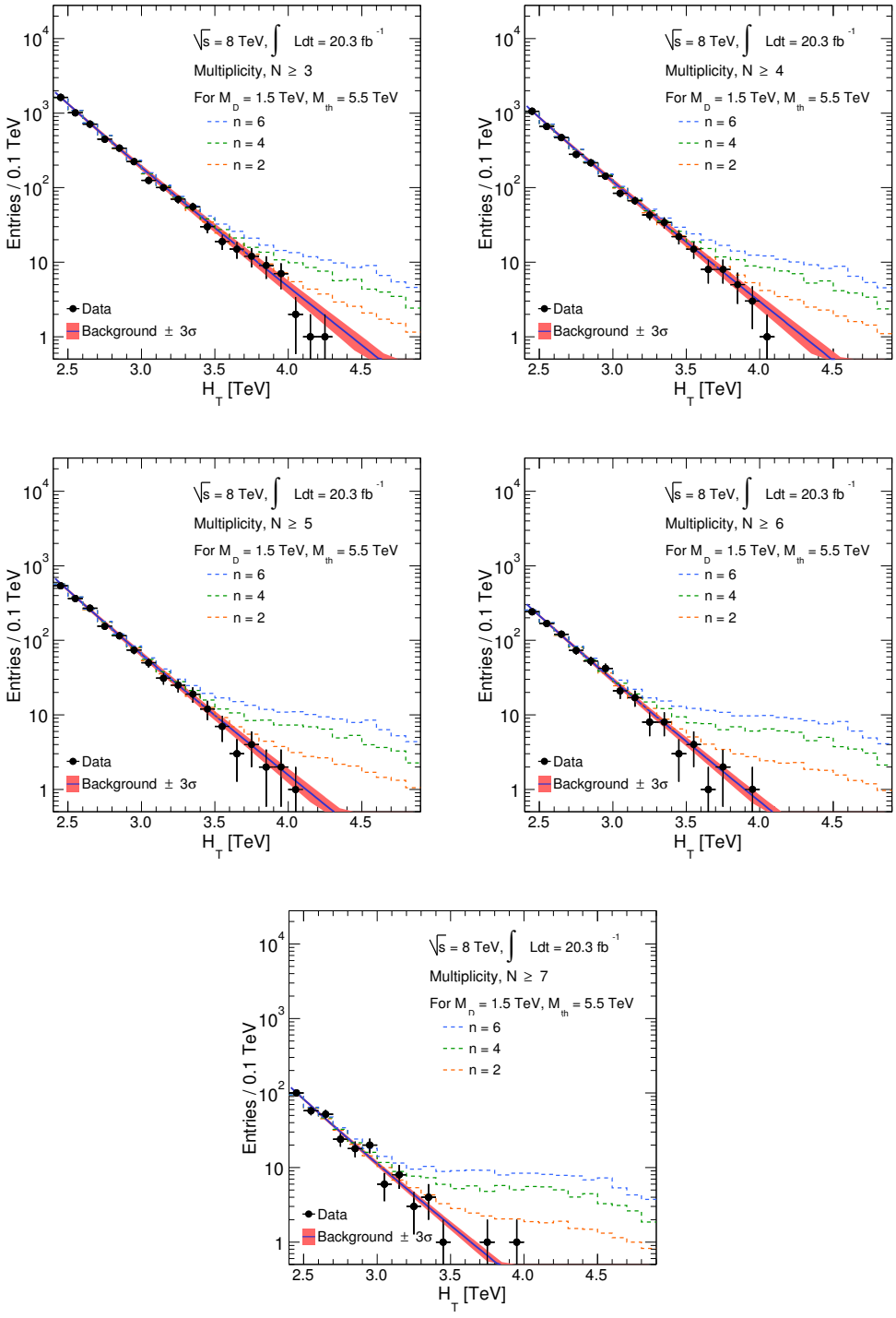

Figure 4.22: CHARYBDIS2 black hole samples generated for fundamental Planck scale $M_D = 1.5$ TeV, black hole mass threshold $M_{\text{th}} = 5.5$ TeV and different numbers of extra dimensions n, shown with the ATLAS 2012 data and the estimated background along with the three sigma uncertainty band for inclusive jet multiplicities $N \geq 3, 4, .., 7$.

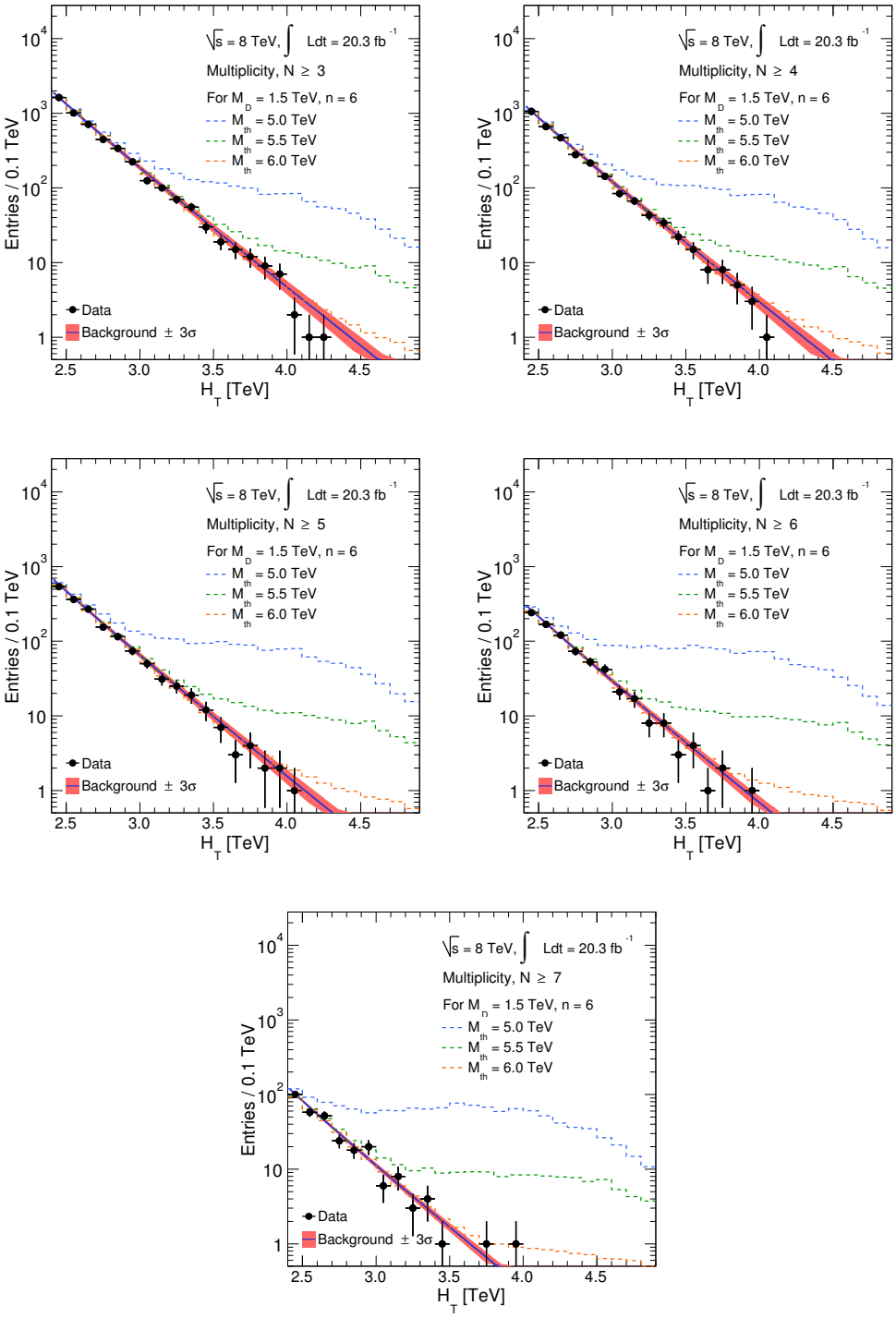

Figure 4.23: CHARYBDIS2 black hole samples generated for fundamental Planck scale $M_D = 1.5$ TeV, number of extra dimensions $n = 6$ and different black hole mass thresholds M_{th}, shown with the ATLAS 2012 data and the estimated background along with the three sigma uncertainty band for inclusive jet multiplicities $N \geq 3, 4, .., 7$.

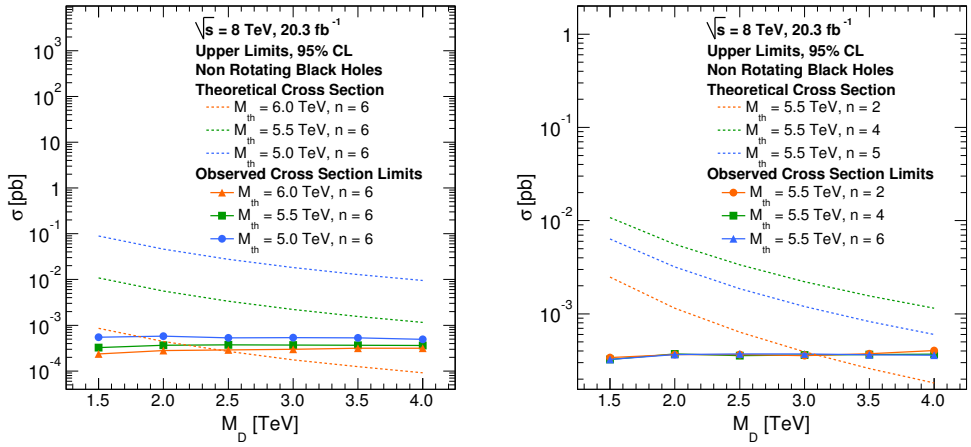

Figure 4.24: The upper limit on the cross section (σ) at the 95% confidence level (CL) (solid lines) for the three sets of the number of extra dimensions (n) and minimum black hole mass (M_{th}) compared with the signal production cross sections from the CHARYBDIS2 black hole generator (dotted lines), as a function of fundamental Planck scale (M_D). The sensitivity of M_{th} and n is observed for the fixed n (left) and M_{th} (right), respectively, as a function of M_D.

with the solid lines. Each colour in Figure 4.24 indicates the trend of the black hole samples, for fixed n and M_{th} values, as a function of M_D. For a given set of (n, M_{th}), the models with specific M_D values can be excluded on the basis of the crossing point of the theoretical and experimental curves.

In Figure 4.24 (left), the case where the theory and experiment curves cross corresponds to $n = 6$ and $M_{\text{th}} = 6$ TeV. The dotted orange curve lies above the solid orange curve until $M_D = 2.4$ TeV, therefore, for this set of parameters ($n = 6$, $M_{\text{th}} = 6$ TeV), the $M_D = 2.4$ TeV is the lower limit and the $M_D < 2.4$ TeV region can be excluded for microscopic black hole production. The other two types of curves (green and blue) do not have any crossing point, therefore, the models in these curves are completely excluded. Similarly, in Figure 4.24 (right), the orange curves have a crossing point around $M_D = 3$ TeV. Therefore, the models corresponding to $n = 2$ and $M_{\text{th}} = 5.5$ TeV have a lower limit $M_D = 3$ TeV. The models

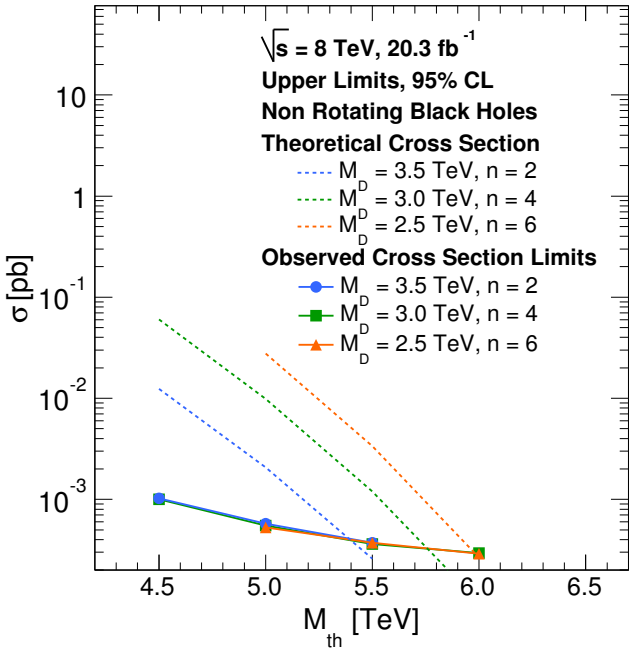

Figure 4.25: The upper limit on cross section (σ) at the 95% confidence level (CL) (solid lines) for the three sets of the number of extra dimension (n) and fundamental Planck scale M_D compared with the signal production cross sections from the CHARYBDIS2 black hole generator (dotted lines), as a function of minimum black hole mass (M_{th}).

corresponding to the set of parameters in the blue and green curves are completely excluded due to same reason described earlier.

A lower limit on M_{th} can also be set for a fixed set of the other two parameters (n, M_D) by using the same method shown in Figure 4.24. For example, the cross section curves for the theory and experiment for three sets of (n, M_D) as a function of M_{th} are shown in Figure 4.25. The lower limits from these curves at the 95% confidence level are shown in Table 4.14 along with a comparison to the CMS results [9, 10]. The lower limits on M_{th} in this study improve upon those published by CMS.

n	M_D (TeV)	Model-dependent lower limits on M_{th} (TeV)		
		CMS (for 3.7 fb^{-1})	CMS (for 12.1 fb^{-1})	ATLAS (for 20.3 fb^{-1})
2	3.5	4.9	5.2	5.4
4	3.0	5.4	5.6	5.8
6	2.5	5.7	5.9	6.0

Table 4.14: Model-dependent lower limits at the 95% confidence level on black hole mass threshold M_{th} for the CMS [9, 10] and ATLAS (this study) 2012 data, for three different sets of extra dimension (n) and fundamental Planck scale (M_D), obtained from CHARBDIS2 non-rotating black hole simulations.

Chapter 5

Summary

In this study, a search for microscopic black holes in multijet final states is conducted with the ATLAS 2012 data using 8 TeV centre of mass energy of pp collisions at the LHC. The data corresponds to an integrated luminosity of 20.3 fb^{-1}. The analysis is based on the QCD H_T shape invariance in jet multiplicity for multijet final states. Given that the microscopic black holes are expected to decay into the high (N,H_T) region, and dedicated ATLAS studies on dijet events [80–82] have not found any resonance or threshold enhancement, the dijet case is chosen as the reference multiplicity to estimate the QCD background. In particular, the $N = 2$ and $H_T > 1.7$ TeV region is considered as the control region. The shape invariance hypothesis allows the estimation of the QCD multijet background in the higher multiplicity states, i.e. $N > 2$, on the basis of function fitting for the dijet multiplicity, i.e. $N = 2$. In order to apply the normalisation region fit to the higher multiplicities, the $N > 2$ and $1.7 < H_T < 2.4$ TeV region is defined as the normalisation region. Finally, $N > 2$ and $H_T > 2.4$ TeV is taken as the signal region.

The QCD multijet background is estimated from the data. However, corrections to the data-driven background estimate due to non-invariance in the H_T distributions using QCD MCs are applied. The effects due to non-invariance cause an overestimation of background in the high-H_T region.

The data characteristics, kinematic variables, function fitting and the H_T shape invariance are studied for both the exclusive jet multiplicities $N = 2, 3, ..., 7$ and the inclusive jet multiplicities $N \geq 2, 3, ..., 7$. The exclusive jet multiplicities are useful to study in order to verify the analysis strategy, but the inclusive jet multiplicities are chosen for the model-independent limits. Since microscopic black holes are expected to produce a range of jet multiplicities instead of decaying into a particular jet multiplicity, it is more useful to use the inclusive multiplicities for the final results. Moreover, the analysis method works better for the inclusive multiplicity cases because the effects of jet migration due to selection thresholds from one multiplicity to another multiplicity state are minimized in the inclusive multijet analysis.

In order to calculate model-independent limits, a counting experiment is performed for $H_T > H_T^{\min}$ as a function of $H_T^{\min}$ values in the signal region. Therefore, uncertainties are also studied as a function of $H_T^{\min}$. The uncertainty due to the correction to non-invariance in the H_T distributions contributes as the major uncertainty in the limit calculations. The uncertainty arising due to corrections to non-invariance remains about 5 - 25% in the $2.4 < H_T^{\min} < 3.5$ TeV region, about 25 - 40% in the $3.6 < H_T^{\min} < 4.5$ TeV region and about 35 - 50% in the $H_T^{\min} > 4.5$ TeV region for the jet multiplicities $N \geq 3, 4, ..., 7$. The uncertainty gradually increases as the statistics decrease with increasing $H_T^{\min}$. Beside the uncertainty due to corrections, the uncertainty due to the choice of the normalisation region and the uncertainties due to jet energy scale (JES) and the jet energy resolution (JER) are also calculated in this analysis. The uncertainty due to the choice of the signal region varies as 1 - 3% increasing with jet multiplicity. The JER uncertainties lies in the band of 1 - 3%, whereas the JES uncertainty remains around 3 - 5%, depending on

$H_T^{\min}$ and the jet multiplicity. The jet energy uncertainties increase with decreasing statistics, i.e. increasing $H_T^{\min}$ and jet multiplicity.

The study is concluded by calculating exclusion limits at the 95% CL for the ATLAS 2012 data on the production of new physics and black holes. The model-independent exclusion limits on cross section times acceptance times efficiency as function of $H_T^{\min}$ fall rapidly at low $H_T^{\min}$ and are flat at high $H_T^{\min}$. The upper limit on the cross section times acceptance times efficiency is 0.29 fb to 0.14 fb for $N \geq 3$ to $N \geq 7$ for $H_T > 4.0$ TeV. Finally the limits on the model parameters are also calculated by using CHARYBDIS2 black hole simulations. Both the model-independent and model-dependent limits have improved values as compared to the CMS results [9, 10].

Appendices

Appendix A

Other Contribution to the ATLAS Experiment

Beside the main analysis shown in chapter 4, I have performed service work for one year to qualify as an author of the ATLAS collaboration. The three types of major tasks as part of my service work are listed as following:

- Bad Calorimeter Regions in the ATLAS 2011 Data: In this study, the problematic regions of the calorimeters were studied in the ATLAS 2011 data. In 2011 data-taking, some of the calorimeter portions were electronically dead during certain data-runs. The study was concluded by suggesting a treatment to avoid the bad data from such problematic regions.

- Jet Cleaning for the ATLAS 2012 Data: The process of filtering fake and badly measured jets is called jet cleaning. The fake jets may appear because of the hardware problems, beam conditions and cosmic ray showers. The study was conducted in order to improve the 2011 jet cleaning. The efficiency of different cleaning criteria was studied in 2012 ATLAS data and compared with the 2011 results.

- Tile HotSpot in the ATLAS 2012 Data: In this study, some electronic noise bursts produced in few runs in a particular $\eta - \phi$ region of tile calorimeter were analyzed. The tile region for these infected runs is

named as the HotSpot region.

All the above studies have played a key role in deciding the official recommendations to deal with these issues, for all the physics groups working in the ATLAS collaboration.

The ATLAS-Alberta group also plays an important role in providing the general services for the ATLAS experiment. As a part of this effort, I have also performed the following tasks:

- ATLAS Control Room Shifts: These shifts are performed inside ATLAS control room by monitoring the performance of different sub-detectors during data-taking. In these shifts, all the minor and major problems are put into an electronic records for the later use. All the major problems are immediately reported to the related experts, and a team of experts decides whether to continue or stop the ongoing data-run.

- Data Quality Shifts: The quality of data is regularly checked after recording the data. The response of different sub-detectors is cross checked. In case of any problem, the data-runs are tagged with different labels in order to take the problems into account for the later analyses.

Appendix B

Trigger Study

In this appendix, further details of the EF_j170_a4tchad_ht700 trigger efficiency are presented. In this multijet analysis, the data events are analyzed in different jet multiplicity bins, therefore it is important to study the trigger efficiency as a function of jet multiplicity. The trigger efficiency as a function of H_T and jet multiplicity is shown in Figure B.1. The efficiency plateau with 40% error always remains true for $H_T > 0.9$ TeV.

The trigger efficiency may also be affected by the pileup effects (described in appendix E). In order to investigate the pileup effects, the trigger efficiency is studied as a function of number of primary vertices (NPV), average number of beam interactions (μ) and H_T. In both the cases, the trigger remains fully efficient for $H_T > 0.9$ TeV, as shown in Figure B.2. Since the H_T variable is constructed from the high-p_T (> 50 GeV) jets, the pileup effects on the trigger efficiency are suppressed. The trigger study is repeated with another reference EF_j145_a4tchad trigger, and all the results stay the same. The EF_j110_a4tchad trigger is preferred as a reference because there may be a biasing from the threshold of the EF_j145_a4tchad trigger, which is very close to the threshold of the trigger used in this study. The trigger efficiency is also studied for PYTHIA8 and HERWIG++ MC samples. The results are similar to those presented for the ATLAS 2012 data.

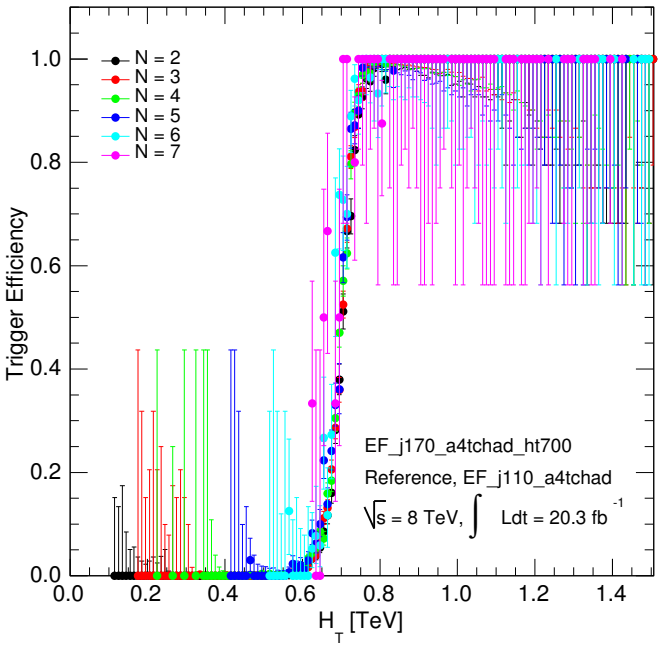

Figure B.1: The EF_j170_a4tchad_ht700 trigger efficiency as a function of H_T, for multiplicities $N = 2, 3, ..., 7$, with respect to the reference trigger EF_j110_a4tchad.

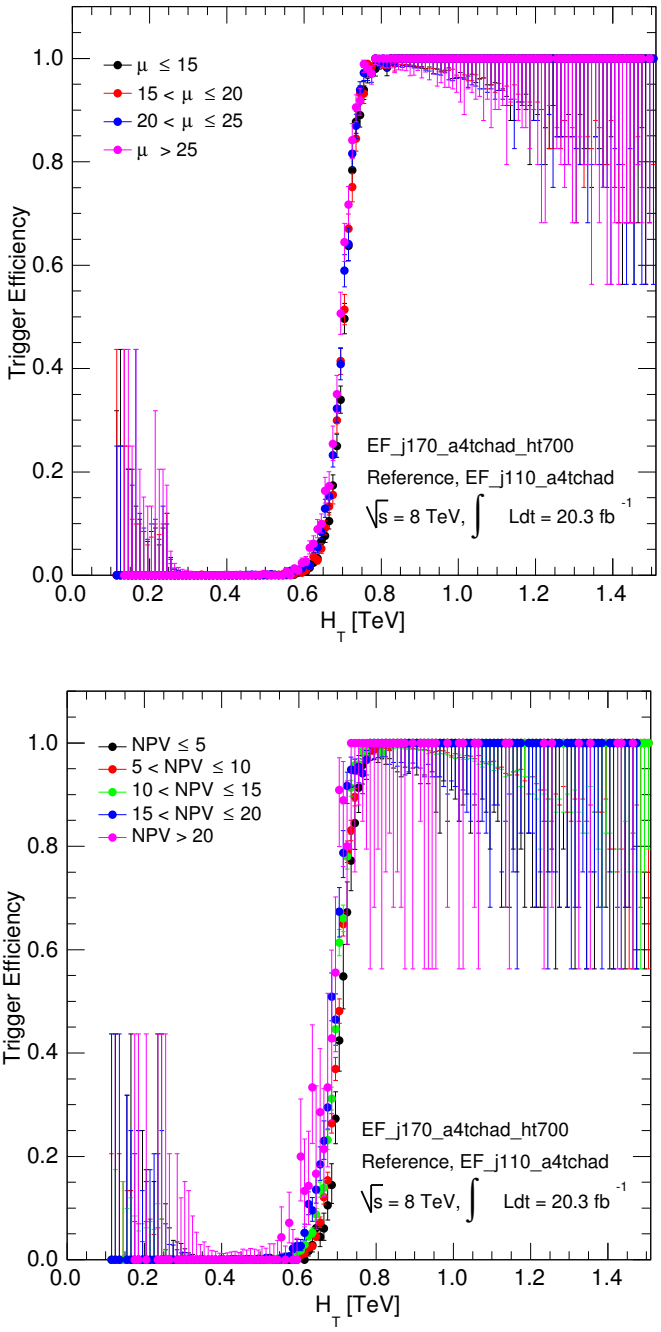

Figure B.2: The EF_j170_a4tchad_ht700 trigger efficiency as a function of H_T, for different μ (number of interactions per bunch crossing) and NPV (number of primary vertices) bins, with respect to the reference EF_j110_a4tchad trigger.

Appendix C

Event Selection

In this appendix, the event selection criteria used in the analysis are described. The standard and analysis-based event cleaning are described in the first section. The sequential cut flow for the data and dijet MC events is shown in the second section.

C.1 Event Cleaning

The recommended event cleaning for all the physics analyses in the ATLAS collaboration requires to have good quality data by removing bad and incomplete data events.

C.1.1 Data Quality

In order to remove bad data runs and bad lumi-blocks a standard good run list (GRL) is used, which is officially produced by the data quality team of the ATLAS collaboration. The GRL used in this study is

- data12_8TeV.periodAllYear_DetStatus-v58-pro14-01_DQDefects-00-00-33_PHYS_StandardGRL_All_Good.xml

The above GRL corresponds to the ATLAS data with good data runs for the whole year of 2012 with the latest tags of detector status (DetStatus) and data quality defects (DQDefects). After applying the GRL filter to

the data, some other standard cuts are applied to remove the bad and incomplete events.

C.1.2 Bad and Corrupt Events

The data events are vetoed by four types of criteria:

- larError: The variable "larError" in D3PDs is used to point out dramatic problems related to various detectors and particularly events with the noise bursts and data integrity errors in the LAr calorimeter. Such type of problematic events in the data can be removed by this flag.

- tileError: Similar to above larError variable this variable removes tile corrupted events which may correspond to any type of noise or problem appeared in tile calorimeter.

- coreFlags: In 2012 data-taking there may be some incomplete events where some detector information is missing from the event. This variable is used to remove all such events from our analysis.

- Tile HotSpot: It is officially recommended to remove the HotSpot region (described in appendix A) from all the physics analyses.

C.1.3 Vertex Requirement

Events in the data are required to have a primary vertex with two or more than two associated tracks. The events with no primary vertex or vertices with less than two associated tracks may come from the pileup effects. The vertex requirement removes some portion of the pileup effects.

C.1.4 Jet Quality

Jet quality is required by removing events with bad and ugly jets with jet $p_T > 20$ GeV. The bad and ugly jets are described as following:

- Bad jets: The "bad" jets correspond to fake energy depositions in the calorimeters which may arise from various sources, such as hardware problems, LHC beam conditions, and cosmic-ray showers. There are different variables to remove the bad jets and we use "isBadLooseMinus" variable to remove such fake jets appearing from calorimeter noises, non-collision and cosmic backgrounds. Since our trigger requires only high-p_T jets and therefore loose criteria of removing bad jets is enough for our analysis.

- Ugly jets: The "ugly" jets correspond to real energy depositions in calorimeter regions but their energy measurement is not accurate because of problematic (or dead) cells or the transition region between barrel and end-caps.

Jet cleaning ensures to have good jets in this study.

C.1.5 Analysis Requirements

After applying standard cleaning cuts, further selection cuts based on the analysis are applied:

- At least 2 jets: As this analysis is based on the assumption of the the H_T shape invariance for different jet multiplicities, a function is fitted on a baseline H_T distribution and applied to the shapes of higher jet multiplicities. In this study, the well studied QCD dijet events [80–82] are chosen as the baseline distribution, therefore, all the monojet events are filtered out.

- $p_T > 50$ GeV: The jet p_T cut is applied to reject the event pileup effects. The pileup effects and the choice of the jet p_T are described in detail in appendix E.

Selection	ATLAS data 2012		PYTHIA8		HERWIG++	
	Events	Cumulative (%)	Events	Cumulative (%)	Events	Cumulative (%)
Trigger	33259733	100.00	18343546	100.00	6403931	100.00
GRL	32056724	96.38	18343546	100.00	6403931	100.00
larError	31936940	96.02	18343546	100.00	6403931	100.00
tileError	31936938	96.02	18343546	100.00	6403931	100.00
coreFlags	31936878	96.02	18343546	100.00	6403931	100.00
Vertex	31932861	96.01	18343545	100.00	6403931	100.00
Jet Quality[1]	31642401	95.14	18184117	99.13	6348673	99.14
At least 2 jets [2]	31638794	95.13	18184117	99.13	6348673	94.14

Table C.1: Cut flow for the ATLAS data 2012, PYTHIA8 and HERWIG++ MCs. Number of events and cumulative percentages corresponding to the selection cuts, are shown for the data and MCs.

- $|\eta| < 2.8$: This cut is based on the detector configuration in order to avoid the forward detector regions where the measurements are comparatively difficult and dedicated studies are required for the forward physics.

C.2 CutFlow

The event cleaning variables described in previous section are sequentially applied to the data and the MC distributions. The event survival for the ATLAS 2012 data, PYTHIA8 MC and HERWIG++ MC after applying each cleaning cut is shown in Table C.1. The 2012 data-taking is performed in the ten data periods, Table C.2 shows cut flow corresponding to each data period.

[1] The removal of jets in the HotSpot region is also included in the jet quality criteria. Same definition is valid for the next table

[2] At least two jets with $p_T > 50$ GeV and $|\eta| < 2.8$. Same definition is valid for the next table.

Period	Trigger	GRL	larError	tileError	coreFlags	Vertex	JetQuality	At least 2 jets	$H_T > 0.9$ TeV
A	1324372	1236133	1233570	1233570	1233570	1233406	1222298	1222034	568192
B	8175261	7953998	7914386	7914385	7914362	7913088	7841907	7840916	3573215
C	2318068	2246480	2240777	2240776	2240761	2240562	2220833	2220568	995256
D	5389454	5273567	5253150	5253150	5253144	5252754	5205995	5205572	2323204
E	4262874	4083010	4069707	4069707	4069695	4069196	4031640	4031307	1791521
G	2072213	2029595	2025730	2025730	2025726	2025432	2006408	2006061	901100
H	2332681	2230169	2224149	2224149	2224149	2223898	2202918	2202426	1025997
I	1729785	1614597	1607303	1607303	1607303	1607073	1592397	1592261	719134
J	4246887	4062695	4046434	4046434	4046434	4045814	4008829	4008552	1833614
L	1408138	1326480	1321734	1321734	1321734	1321638	1309176	1309097	599834

Table C.2: The number of events survived corresponding to each selection criteria, for all the ATLAS 2012 data periods of pp collisions.

Appendix D

Jet Kinematic Distributions

The jet ϕ, the first leading jet p_T and the second leading jet p_T distributions, for the exclusive jet multiplicities i.e. $N = 2, 3, ..., 7$, are shown in Figures D.1, D.2 and D.3, respectively. The distributions are shown for the ATLAS 2012 data, PYTHIA8 and HERWIG++ MCs. The distributions for both the MCs show good compatibility with the data, and with each other.

From Figure D.1, the jet ϕ distributions for the data and MCs are in agreement within 10% for the most of jet multiplicity cases. There are also some fluctuations around $\phi = 1.6$, especially in low jet multiplicities. These fluctuations are not reproduced by the MC distributions, which come from known detector problems.

From Figures D.2 and D.3, the first and second leading jet p_T distributions for the data and MCs have the reasonable shapes and good agreement to each other. Most of distributions are within 20% agreement which remains almost the same when all the jets ($p_T > 50$ GeV and $|\eta| < 2.8$) in an event are used to construct the H_T distributions shown in Figures 4.5 and 4.6. Both the PYTHIA8 and HERWIG++ distributions show almost the same shapes for the jet p_T distributions especially for the low multiplicities.

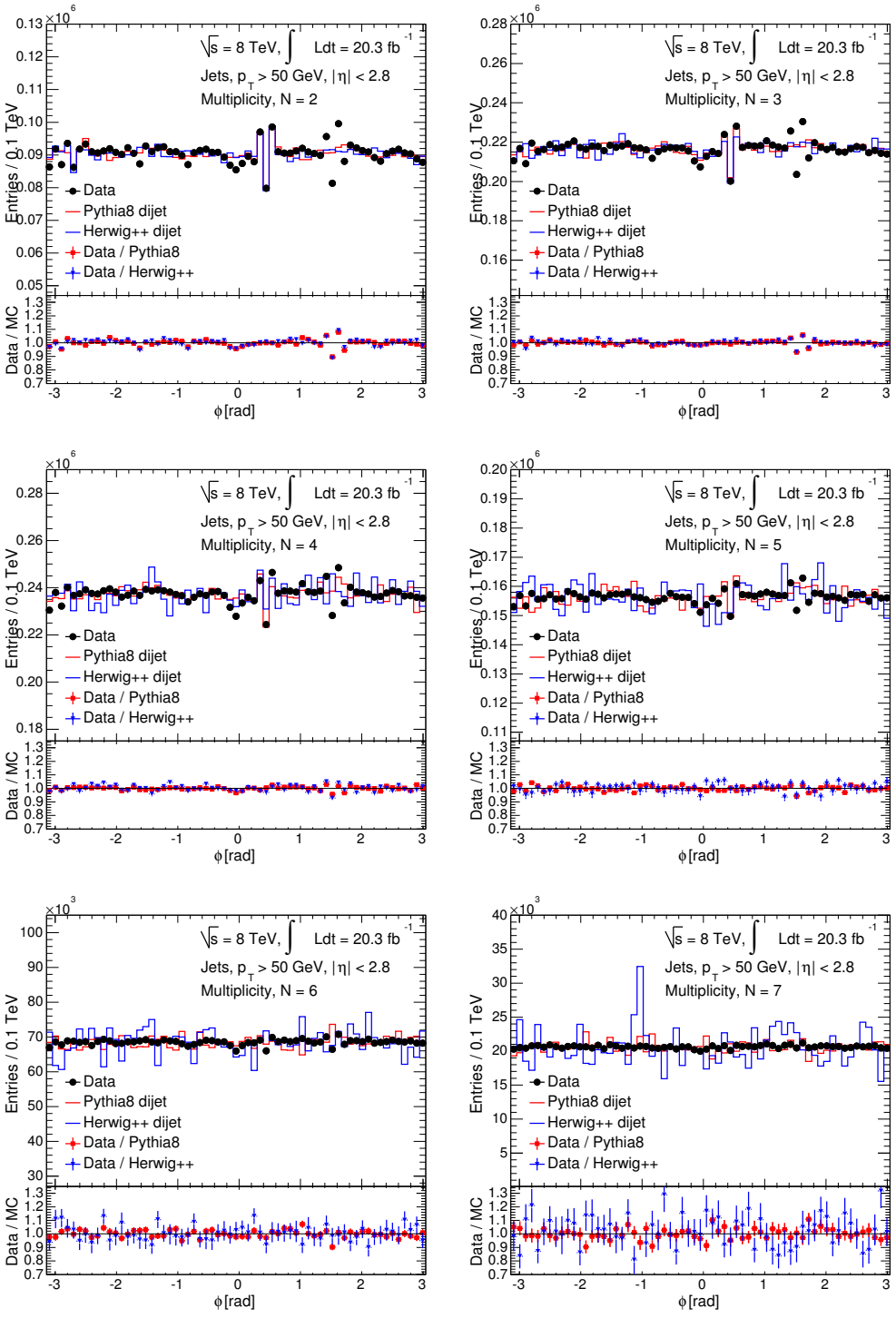

Figure D.1: The ϕ distributions of jets for the exclusive jet multiplicities, $N = 2, 3, ..., 7$, shown for the ATLAS 2012 data, PYTHIA8 (red) and HERWIG++ (blue) MCs. At the bottom of each plot, the ratio of the data to MC has been shown for both the MCs.

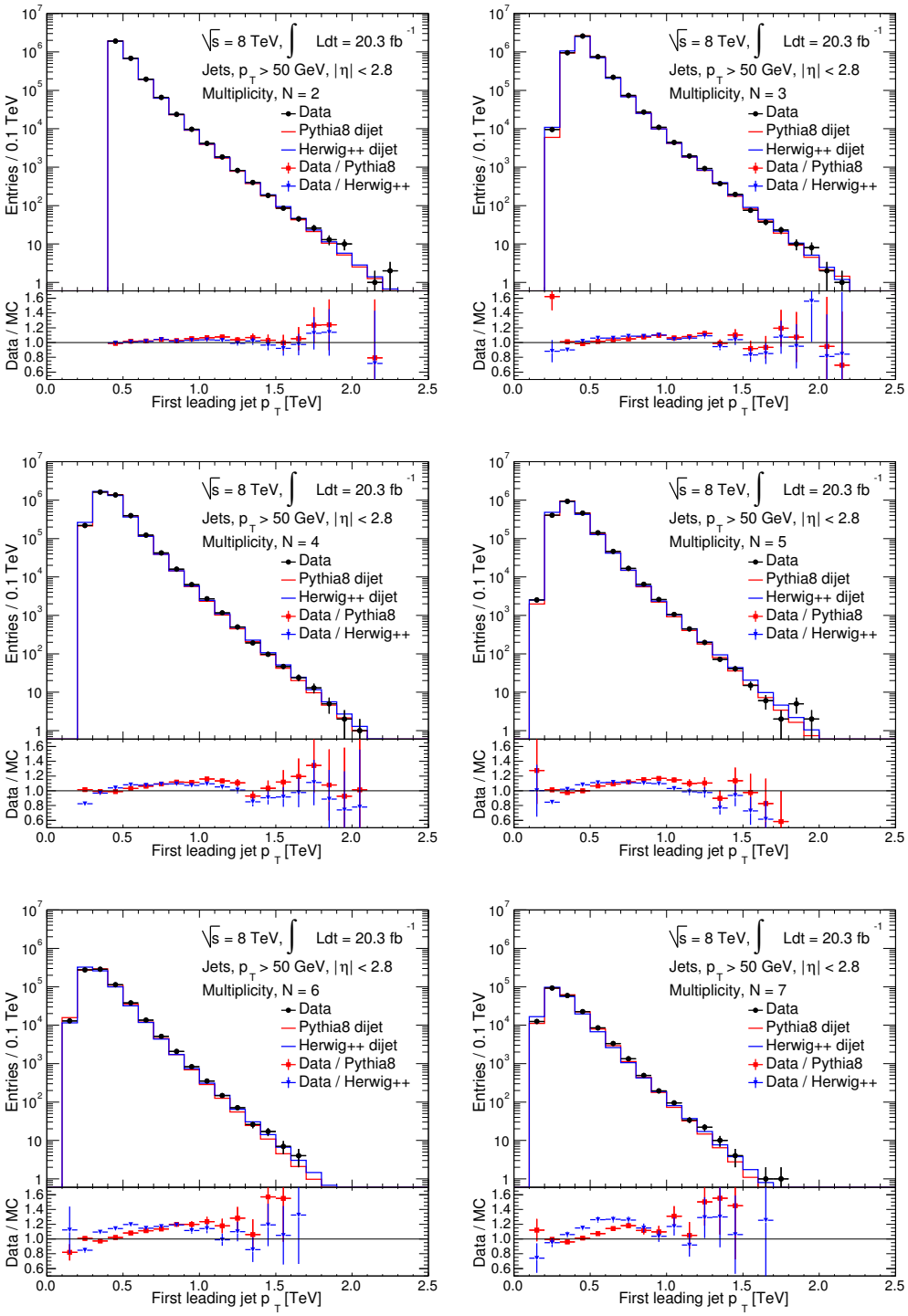

Figure D.2: The first leading jet p_T distributions for the exclusive jet multiplicities, $N = 2, 3, ..., 7$, shown for the ATLAS 2012 data, PYTHIA8 (red) and HERWIG++ (blue) MCs. At the bottom of each plot, the ratio of the data to MC has been shown for both the MCs.

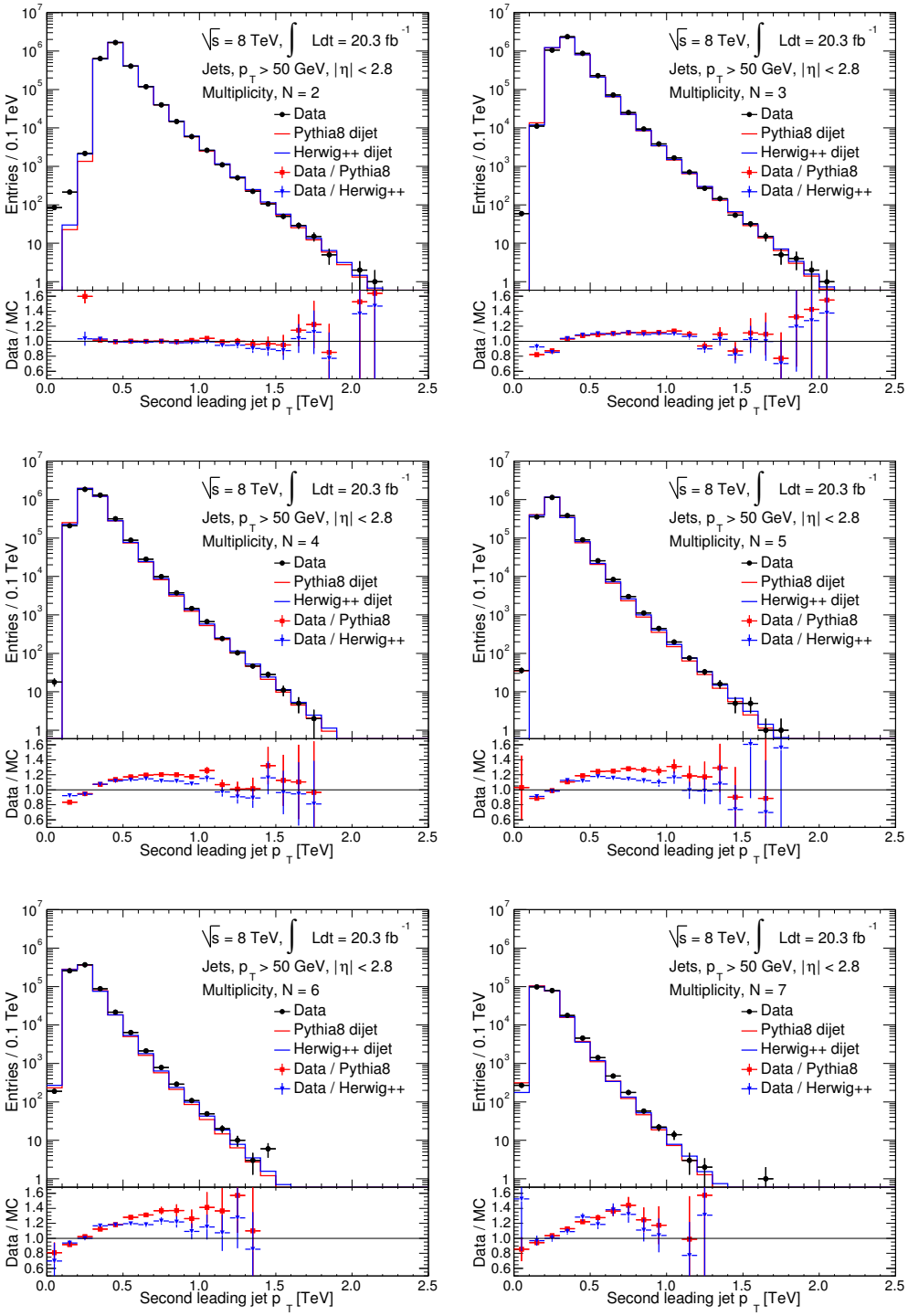

Figure D.3: The second leading jet p_T distributions for the exclusive jet multiplicities, $N = 2, 3, ..., 7$, shown for the ATLAS 2012 data, PYTHIA8 (red) and HERWIG++ (blue) MCs. At the bottom of each plot, the ratio of the data to MC has been shown for both the MCs.

Appendix E

Pileup Study

In pp collisions at the LHC, the proton beams are in the form of bunches. During a bunch crossing, there may be more than one pp interaction due to increased per-bunch luminosity, varying bunch configuration and reduced bunch spacing. All these additional interactions are often referred to as the pileup effects. Due to reduced bunch spacing and high luminosity in 2012 as compared to pp collisions in years 2011 and 2010 at the LHC, the effects of event pileup on jets are significantly different.

The average amount of pileup can be described by the number of reconstructed primary vertices in an event, i.e. NPV, and average number of interactions per bunch crossing, i.e. μ. In the next two subsections, the study of these two variables as a function of the jet p_T thresholds is presented, to find a suitable jet-p_T threshold to minimize the pileup effects. After selecting an appropriate jet-p_T threshold, the pileup effects are cross checked for the H_T distributions at the end of this appendix.

E.0.1 Number of Primary Vertices (NPV)

In this study, the events with at least one primary vertex with two or more tracks are chosen, with a very low inefficiency ($< 1\%$). An average jet multiplicity $\langle N \rangle$ in different bins of NPV is computed for different lower thresholds of the jet p_T. The five NPV bins are defined as

NPV	Average jet multiplicity $\langle N \rangle$ for different jet p_T cuts of					
	20 GeV	30 GeV	40 GeV	50 GeV	60 GeV	70 GeV
0-5	5.29	4.39	3.94	3.63	3.40	3.22
5-10	5.36	4.36	3.89	3.58	3.35	3.18
10-15	5.60	4.38	3.88	3.56	3.33	3.16
15-20	6.03	4.44	3.88	3.56	3.33	3.15
> 20	6.72	4.57	3.91	3.57	3.33	3.15

Table E.1: The five NPV (average number of interactions per bunch crossing) bins, $0 < \text{NPV} < 5$, $5 < \text{NPV} < 10$, $10 < \text{NPV} < 15$, $15 < \text{NPV} < 20$ and $\text{NPV} > 20$, corresponding to average jet multiplicity $\langle N \rangle$, are shown for jets with $p_T > 20$, 30, ..., 70 GeV, for the ATLAS 2012 data.

- $0 < \text{NPV} < 5$
- $5 < \text{NPV} < 10$
- $10 < \text{NPV} < 15$
- $15 < \text{NPV} < 20$, and
- $\text{NPV} > 20$.

For these NPV-bins, the values of average multiplicity $\langle N \rangle$ are shown in Table E.1 for jet $p_T > 20$, 30,..., 70 GeV, which are also plotted in Figure E.1. The pileup effects would be prominent if average jet multiplicity $\langle N \rangle$ increases with increase in NPV otherwise a constant trend in $\langle N \rangle$ corresponds to the minimum pileup effects. From Figure E.1, the maximum pileup effects can be seen for the jets with $p_T > 20$ GeV case and these effects decrease with increasing jet p_T threshold. A tradeoff is set here by choosing a threshold of jet p_T to have minimal pileup effects and reasonable statistics. Therefore, the jets with $p_T > 50$ GeV are chosen where the pileup effects are minimized and statistics are reasonably high.

Both in Table E.1 and Figure E.1, no errors are being shown on $\langle N \rangle$ because the error on mean multiplicity $\langle N \rangle_{\text{error}}$ is always very small as

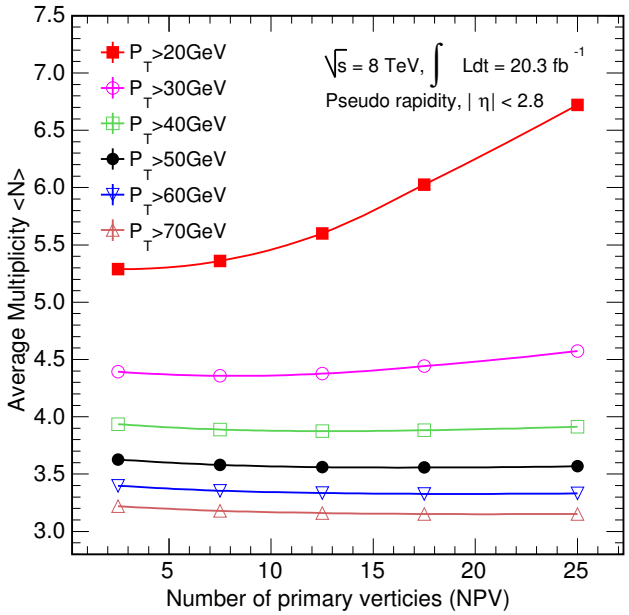

Figure E.1: Average jet multiplicity $\langle N \rangle$ as a function of number of primary vertices (NPV) and jet p_T thresholds, is shown for the ATLAS 2012 data. The five points in each p_T curve correspond to five NPV-bins, i.e. $0 < \text{NPV} < 5$, $5 < \text{NPV} < 10$, $10 < \text{NPV} < 15$, $15 < \text{NPV} < 20$ and $\text{NPV} > 20$.

compared to $\langle N \rangle$ and can be ignored, as it is defined as

$$\langle N \rangle_{\text{error}} = \frac{1}{N_{\text{events}}} \sum_i \sqrt{(N_i - \langle N \rangle)^2} \simeq 10^{-4}, \tag{E.1}$$

where N_{events} are the total number of entries in a NPV-bin, $\langle N \rangle$ are the average number of jets or mean jet multiplicity in a NPV-bin and N_i are the total number of jets in an event i. The error on $\langle N \rangle_{\text{error}}$ remains very small for all the NPV-bins, typically of the order of 10^{-4}, and can be neglected.

E.0.2 Average Interactions per Beam Crossing (μ)

Similar to NPV study, an average jet multiplicity $\langle N \rangle$ is also computed in different μ-bins for different jet-p_T thresholds. The four μ-bins are defined so that each bin can have almost the same statistics. The μ-bins are

- $0 < \mu < 15$
- $15 < \mu < 20$
- $20 < \mu < 25$, and
- $\mu > 25$.

The average jet multiplicity $\langle N \rangle$ as a function of jet p_T and μ-bins are shown in Table E.2 and Figure E.2. Again, the pileup effects are dominant for jet $p_T > 20$ GeV. The choice of $p_T > 50$ GeV looks reasonable in order to minimize the pileup effects[1].

The errors for $\langle N \rangle$ are very small, typically of the order of 10^{-4}, and can be ignored.

E.0.3 Choice of jet $p_T > 50$ GeV

From the study of NPV and μ variables, the jet $p_T > 50$ GeV is chosen to minimize the pileup effects.

[1] As compared to $p_T > 20$ GeV, the choice of $p_T > 50$ GeV removes the low p_T jets, i.e. $20 < p_T < 50$, which are more sensitive to the pileup effects.

μ	Average jet multiplicity $\langle N \rangle$ for different jet p_T cuts of					
	20 GeV	30 GeV	40 GeV	50 GeV	60 GeV	70 GeV
0-15	5.29	4.34	3.88	3.57	3.35	3.17
15-20	5.44	4.36	3.88	3.57	3.35	3.17
20-25	5.62	4.39	3.89	3.57	3.34	3.17
>25	5.88	4.43	3.90	3.57	3.34	3.17

Table E.2: The four μ (average number of interactions per bunch crossing) bins, $0 < \mu < 15$, $15 < \mu < 20$, $20 < \mu < 25$ and $\mu > 25$, corresponding to average jet multiplicity $\langle N \rangle$ values are shown for jet $p_T > 20$, 30, ..., 70 GeV, for the ATLAS 2012 data.

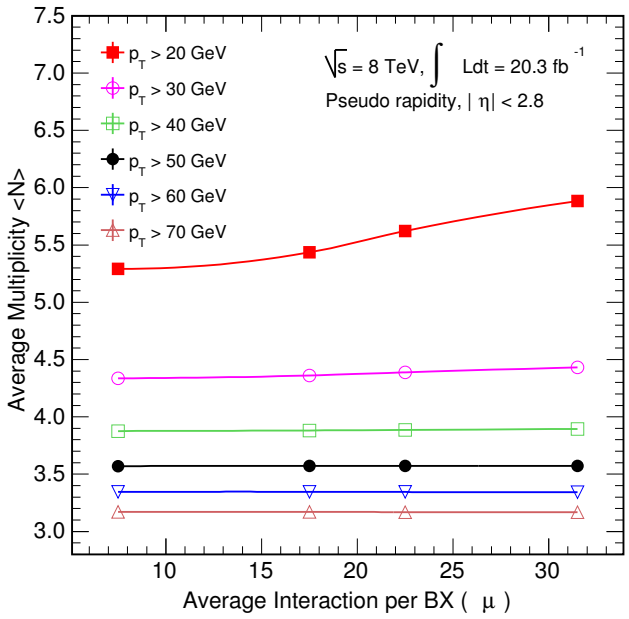

Figure E.2: Average jet multiplicity $\langle N \rangle$ as a function of average number of interactions per bunch crossing (BX), denoted as μ, and jet p_T is shown for ATLAS 2012 data. The four points in p_T curve correspond to four μ-bins, i.e. $0 < \mu < 15$, $15 < \mu < 20$, $20 < \mu < 25$ and $\mu > 25$.

Jet vertex fraction (JVF) is another variable used to study pileup effects. The JVF estimates the fraction of tracks transverse momentum associated to a jet from the hard-scattering interaction, therefore it discriminates the jets produced in the hard-scattering and those due to the pileup effects. The choice of jet $p_T > 50$ GeV eliminates the need of JVF cut because it is recommended for the low-p_T jets.

In this section, the pileup effects for the H_T distributions are cross checked for the choice of $p_T > 50$ GeV. In earlier sections, different NPV and μ-bins are defined to investigate the pileup effects, the same bins are used to study the pileup effect in the H_T distributions. If the pileup effects in the H_T distributions are minimized then the H_T distribution in one NPV-bin should match to the H_T distribution in any other NPV-bin and similarly true for the μ-bins. The H_T ratios for four NPV-bins, $0 < \text{NPV} < 5$, $5 < \text{NPV} < 10$, $15 < \text{NPV} < 20$ and $\text{NPV} > 20$ are calculated with respect to a NPV-bin, $10 < \text{NPV} < 15$. For the jet $p_T > 50$ GeV, the flat trend of the H_T ratio as a function of NPV shows that the pileup effects are minimal (Figure E.3). The NPV-bin $15 < \text{NPV} < 20$ is the highest statistics bin and used as the reference. Any NPV-bin can be used as the reference but the choice of the highest statistics bin is more generic to investigate the flatness in the H_T ratios.

Similarly, the H_T ratios of three μ-bins, $0 < \mu < 15$, $20 < \mu < 25$ and $\mu > 25$ with respect to the H_T in $15 < \mu < 20$ are shown in Figure E.4. The H_T ratio for each μ-bin shows the flat trend. Therefore, the pileup effects are minimized for the H_T distributions constructed from the jets with $p_T > 50$ GeV.

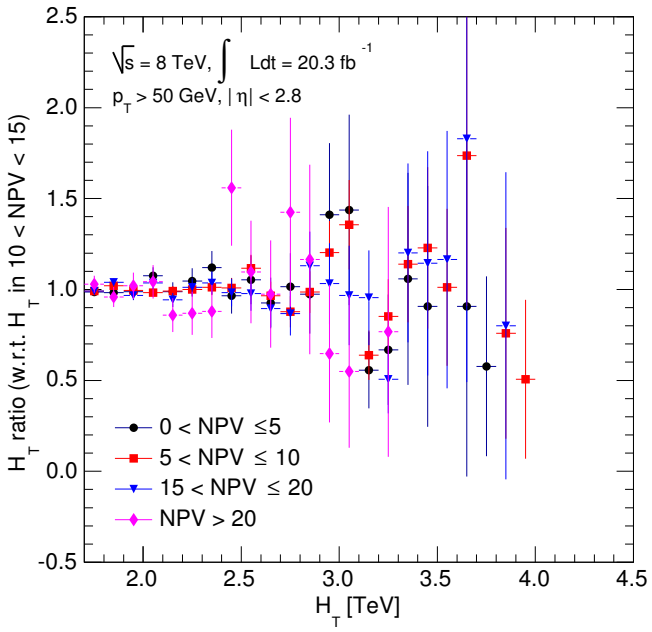

Figure E.3: The ratios of the H_T in NPV-bins, $0 < \text{NPV} < 5$, $5 < \text{NPV} < 10$, $15 < \text{NPV} < 20$ and $\text{NPV} > 20$ to the H_T in $10 < \text{NPV} < 15$, for the ATLAS 2012 data.

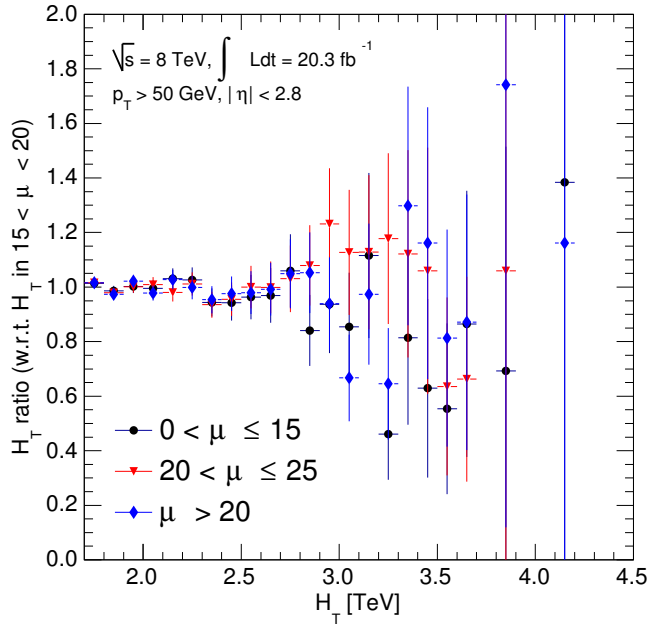

Figure E.4: The ratios of the H_T in μ-bins, $0 < \mu < 15$, $20 < \mu < 25$ and $\mu > 25$ to the H_T in $15 < \mu < 20$, for the ATLAS 2012 data.

Bibliography

[1] I. Antoniadis, N. Arkani-Hamed, S. Dimopoulos, and G. Dvali, "New dimensions at a millimeter to a fermi and superstrings at a TeV," Physics Letters B 436 no. 3-4, (1998) 257–263, arXiv:hep-ph/9804398 [hep-ph]. http://www.sciencedirect.com/science/article/pii/S0370269398008600.

[2] N. Arkani-Hamed, S. Dimopoulos, and G. Dvali, "The hierarchy problem and new dimensions at a millimeter," Phys. Lett. B 429 (1998) 263–272, arXiv:hep-ph/9803315 [hep-ph]. http://www.sciencedirect.com/science/article/pii/S0370269398004663.

[3] N. Arkani-Hamed, S. Dimopoulos, and G. Dvali, "Phenomenology, astrophysics and cosmology of theories with submillimeter dimensions and TeV scale quantum gravity," Phys. Rev. D 59 (1999) 086004, arXiv:hep-ph/9807344 [hep-ph]. http://prd.aps.org/abstract/PRD/v59/i8/e086004.

[4] L. Randall and R. Sundrum, "A large mass hierarchy from a small extra dimension," Phys. Rev. Lett. 83 (1999) 3370–3373, arXiv:hep-ph/9905221 [hep-ph]. http://prl.aps.org/abstract/PRL/v83/i17/p3370_1.

[5] L. Randall and R. Sundrum, "An alternative to compactification," Phys. Rev. Lett. 83 (1999) 4690–4693, arXiv:hep-th/9906064 [hep-th]. http://prl.aps.org/abstract/PRL/v83/i23/p4690_1.

[6] ATLAS Collaboration, "Improved luminosity determination in pp collisions at $\sqrt{s} = 7$ TeV using the ATLAS detector at the LHC," Eur. Phys. J. C 73 (2013) 2518, arXiv:1302.4393 [hep-ex]. http://link.springer.com/article/10.1140%2Fepjc%2Fs10052-013-2518-3.

[7] CMS Collaboration, "Search for microscopic black hole signatures at the Large Hadron Collider," Phys. Lett. B 697 (2011) 434–453, arXiv:1012.3375 [hep-ex]. http://www.sciencedirect.com/science/article/pii/S0370269311001778.

[8] CMS Collaboration, "Search for microscopic black holes in pp collisions at $\sqrt{s} = 7$ TeV," J. High Energy Phys. 1204 (2012) 061, arXiv:1202.6396 [hep-ex]. http://link.springer.com/article/10.1007%2FJHEP04%282012%29061.

[9] CMS Collaboration, "Search for microscopic black holes in pp collisions at $\sqrt{s} = 8$ TeV with the CMS detector," CMS PAS EXO-12-009 (2012) . https://cds.cern.ch/record/1460444.

[10] CMS Collaboration, "Search for microscopic black holes in pp collisions at $\sqrt{s} = 8$ TeV," J. High Energy Phys. 1307 (2013) 178, arXiv:1303.5338 [hep-ex]. http://link.springer.com/article/10.1007%2FJHEP07%282013%29178.

[11] A. Quadt, "Top quark physics at hadron colliders," Eur. Phys. J. C 48 (2006) 835–1000. http://link.springer.com/article/10.1140%2Fepjc%2Fs2006-02631-6.

[12] G. Altarelli, "The standard model of particle physics," arXiv:hep-ph/0510281 [hep-ph].

[13] E. Radermacher, "The experimental discovery of the intermediate vector bossons W^+, W^- and Z^0 at the CERN $p\bar{p}$ collider," Prog. Part. Nucl. Phys. 14 (1985) 231–328. http://www.sciencedirect.com/science/article/pii/0146641085900559.

[14] ATLAS Collaboration, "Observation of a new particle in the search for the standard model Higgs boson with the ATLAS detector at the LHC," Phys. Lett. B 716 (2012) 1 – 29, arXiv:1207.7214 [hep-ex]. http://www.sciencedirect.com/science/article/pii/S037026931200857X.

[15] CMS Collaboration, "Observation of a new boson at a mass of 125 GeV with the CMS experiment at the LHC," Phys. Lett. B716 no. 1, (2012) 30 – 61, arXiv:1207.7235 [hep-ex]. http://www.sciencedirect.com/science/article/pii/S0370269312008581.

[16] Particle Data Group, "Review of particle physics (RPP)," Phys. Rev. D 86 (Jul, 2012) 010001. http://prd.aps.org/abstract/PRD/v86/i1/e010001.

[17] OPERA Collaboration, "Observation of a first candidate event in the OPERA experiment in the CNGS beam," Phys. Lett. B 691 no. 3, (2010) 138 – 145, arXiv:1006.1623 [hep-ex]. http://www.sciencedirect.com/science/article/pii/S0370269310007537.

[18] I. Antoniadis, "A possible new dimension at a few TeV," Phys. Lett. B 246 (1990) 377–384. http://www.sciencedirect.com/science/article/pii/037026939090617F.

[19] P. Horava and E. Witten, "Eleven-dimensional supergravity on a manifold with boundary," Nucl.Phys. B475 (1996) 94–114, arXiv:hep-th/9603142 [hep-th]. http://www.sciencedirect.com/science/article/pii/0550321396003082.

[20] P. Horava and E. Witten, "Heterotic and Type I string dynamics from eleven-dimensions," Nucl. Phys. B 460 (1996) 506–524, arXiv:hep-th/9510209 [hep-th]. http://www.sciencedirect.com/science/article/pii/0550321395006214.

[21] J. D. Lykken, "Weak scale superstrings," Phys. Rev. D 54 (1996) 3693–3697, arXiv:hep-th/9603133 [hep-th]. http://prd.aps.org/abstract/PRD/v54/i6/pR3693_1.

[22] D. Kapner, T. Cook, E. Adelberger, J. Gundlach, B. R. Heckel, et al., "Tests of the gravitational inverse-square law below the dark-energy length scale," Phys. Rev. Lett. 98 (2007) 021101, arXiv:hep-ph/0611184 [hep-ph]. http://prl.aps.org/abstract/PRL/v98/i2/e021101.

[23] S. Hawking, "Particle creation by black holes," Commun. Math. Phys. 43 (1975) 199–220. http://link.springer.com/article/10.1007%2FBF02345020.

[24] K. S. Thorne, "Nonspherical gravitational collapse–a short review," Magic Without Magic: John Archibald Wheeler 1 (1972) 231.

[25] R. Myers and M. Perry, "Black holes in higher dimensional space-times," Annals of Physics 172 no. 2, (1986) 304 – 347.

http://www.sciencedirect.com/science/article/pii/0003491686901867.

[26] S. Giddings and S. Thomas, "High energy colliders as black hole factories: The end of short distance physics," Phys. Rev. D 65 (2002) 056010, arXiv:hep-ph/0106219 [hep-ph]. http://prd.aps.org/abstract/PRD/v65/i5/e056010.

[27] P. Aichelburg and R. Sexl, "On the gravitational field of a massless particle," Gen. Rel. Grav. 2 (1971) 303–312. http://link.springer.com/article/10.1007%2FBF00758149.

[28] S. W. Hawking, Hawking on the Big Bang and Black Holes. World Scientific Publishing Company, 1993. http://www.worldscientific.com/worldscibooks/10.1142/1751.

[29] R. Penrose, "Unpublished," 1974.

[30] P. D. D'Eath and P. N. Payne, "Gravitational radiation in black-hole collisions at the speed of light. I. Perturbation treatment of the axisymmetric collision," Phys. Rev. D 46 (Jul, 1992) 658–674. http://link.aps.org/doi/10.1103/PhysRevD.46.658.

[31] P. D. D'Eath and P. N. Payne, "Gravitational radiation in black-hole collisions at the speed of light. II. Reduction to two independent variables and calculation of the second-order news function," Phys. Rev. D 46 no. 2, (1992) 675–693. http://link.aps.org/doi/10.1103/PhysRevD.46.675.

[32] D. M. Eardley and S. B. Giddings, "Classical black hole production in high-energy collisions," Phys. Rev. D 66 (2002) 044011, arXiv:gr-qc/0201034 [gr-qc]. http://prd.aps.org/abstract/PRD/v66/i4/e044011.

[33] S. Dimopoulos and G. L. Landsberg, "Black holes at the Large Hadron Collider," Phys. Rev. Lett. 87 (2001) 161602, arXiv:hep-ph/0106295 [hep-ph]. http://prl.aps.org/abstract/PRL/v87/i16/e161602.

[34] D. Ida, K. Oda, and S. C. Park, "Rotating black holes at future colliders. II. Anisotropic scalar field emission," Phys. Rev. D 71 (2005) 124039, arXiv:hep-th/0503052 [hep-th]. http://prd.aps.org/abstract/PRD/v71/i12/e124039.

[35] H. Yoshino and Y. Nambu, "Black hole formation in the grazing collision of high-energy particles," Phys. Rev. D 67 (2003) 024009, arXiv:gr-qc/0209003 [gr-qc]. http://inspirehep.net/record/974903.

[36] H. Yoshino and V. S. Rychkov, "Improved analysis of black hole formation in high-energy particle collisions," Phys. Rev. D 71 (2005) 104028, arXiv:hep-th/0503171 [hep-th]. http://prd.aps.org/abstract/PRD/v77/i8/e089905.

[37] Douglas M. Gingrich, "Black hole cross-section at the LHC," Int. J. Mod. Phys. A 21 (2006) 6653–6676, arXiv:hep-ph/0609055 [hep-ph]. http://www.worldscientific.com/doi/abs/10.1142/S0217751X06035087.

[38] Douglas M. Gingrich, "Experimental limits on the fundamental Planck scale in large extra dimensions," arXiv:1210.5923 [hep-ex].

[39] P. C. Argyres, S. Dimopoulos, and J. March-Russell, "Black holes and submillimeter dimensions," Phys. Lett. B 441 (1998) 96–104, arXiv:hep-th/9808138 [hep-th]. http://www.sciencedirect.com/science/article/pii/S0370269398011848.

[40] P. Kanti, "Black holes at the Large Hadron Collider," Lect. Notes Phys. 769 (2009) 387–423, arXiv:0802.2218 [hep-th]. http://link.springer.com/chapter/10.1007%2F978-3-540-88460-6_10.

[41] P. Kanti and J. March-Russell, "Calculable corrections to brane black hole decay: The scalar case," Phys. Rev. D 66 (2002) 024023, arXiv:hep-ph/0203223 [hep-ph]. http://prd.aps.org/abstract/PRD/v66/i2/e024023.

[42] P. Kanti and J. March-Russell, "Calculable corrections to brane black hole decay. II. Greybody factors for spin 1/2 and 1," Phys. Rev. D 67 (2003) 104019, arXiv:hep-ph/0212199 [hep-ph]. http://prd.aps.org/abstract/PRD/v67/i10/e104019.

[43] E. Newman and R. Penrose, "An approach to gravitational radiation by a method of spin coefficients," J. Math. Phys. 3 no. 3, (1962) 566–578. http://jmp.aip.org/resource/1/jmapaq/v3/i3/p566_s1?isAuthorized=no.

[44] Douglas M. Gingrich, "Missing energy in black hole production and decay at the Large Hadron Collider," J. High Energy Phys. 0711 (2007) 064, arXiv:0706.0623 [hep-ph]. http://iopscience.iop.org/1126-6708/2007/11/064/.

[45] S. S. Gubser, I. R. Klebanov, and A. A. Tseytlin, "String theory and classical absorption by three-branes," Nucl. Phys. B 499 (1997) 217–240, arXiv:hep-th/9703040 [hep-th]. http://www.sciencedirect.com/science/article/pii/S0550321397003258.

[46] P. Kanti, "Black holes in theories with large extra dimensions: A review," Int. J. Mod. Phys. A 19 (2004) 4899–4951, arXiv:hep-ph/0402168 [hep-ph]. http://www.worldscientific.com/doi/abs/10.1142/S0217751X04018324.

[47] C. M. Harris and P. Kanti, "Hawking radiation from a (4+n)-dimensional black hole: Exact results for the Schwarzschild phase," J. High Energy Phys. 0310 (2003) 014, arXiv:hep-ph/0309054 [hep-ph]. http://iopscience.iop.org/1126-6708/2003/10/014/.

[48] V. Cardoso, M. Cavaglia, and L. Gualtieri, "Black hole particle emission in higher-dimensional spacetimes," Phys. Rev. Lett. 96 (2006) 071301, arXiv:hep-th/0512002 [hep-th]. http://link.aps.org/doi/10.1103/PhysRevLett.96.071301.

[49] V. Cardoso, M. Cavaglia, and L. Gualtieri, "Erratum: Black hole particle emission in higher-dimensional spacetimes," Phys. Rev. Lett. 96 no. 21, (2006) 219902. http://prl.aps.org/abstract/PRL/v96/i21/e219902.

[50] V. Cardoso, M. Cavaglia, and L. Gualtieri, "Hawking emission of gravitons in higher dimensions: Non-rotating black holes," J. High Energy Phys. 0602 (2006) 021, arXiv:hep-th/0512116 [hep-th]. http://iopscience.iop.org/1126-6708/2006/02/021/.

[51] B. Koch, M. Bleicher, and S. Hossenfelder, "Black hole remnants at the LHC," J. High Energy Phys. 0510 (2005) 053, arXiv:hep-ph/0507138 [hep-ph]. http://iopscience.iop.org/1126-6708/2005/10/053/.

[52] T. J. Humanic, B. Koch, and H. Stoecker, "Signatures for black hole production from hadronic observables at the Large Hadron Collider," Int. J. Mod. Phys. E 16 (2007) 841–852, arXiv:hep-ph/0607097 [hep-ph]. http://www.worldscientific.com/doi/abs/10.1142/S0218301307006320.

[53] B. Koch, M. Bleicher, and H. Stoecker, "Black holes at LHC?," J. Phys. G 34 (2007) S535–542, arXiv:hep-ph/0702187 [hep-ph]. http://iopscience.iop.org/0954-3899/34/8/S44/.

[54] C. Harris, P. Richardson, and B. Webber, "CHARYBDIS: A black hole event generator," J. High Energy Phys. 0308 (2003) 033, arXiv:hep-ph/0307305 [hep-ph]. http://iopscience.iop.org/1126-6708/2003/08/033/.

[55] M. Cavaglia, R. Godang, L. Cremaldi, and D. Summers, "Catfish: A Monte Carlo simulator for black holes at the LHC," Comput. Phys. Commun. 177 (2007) 506–517, arXiv:hep-ph/0609001 [hep-ph]. http://www.sciencedirect.com/science/article/pii/S0010465507002524.

[56] D. C. Dai, G. Starkman, D. Stojkovic, C. Issever, E. Rizvi, et al., "BlackMax: A black-hole event generator with rotation, recoil, split branes, and brane tension," Phys. Rev. D 77 (2008) 076007, arXiv:0711.3012 [hep-ph]. http://prd.aps.org/abstract/PRD/v77/i7/e076007.

[57] Douglas M. Gingrich, "Monte Carlo event generator for black hole production and decay in proton-proton collisions – QBH version 1.02," Comput. Phys. Commun. 181 (2010) 1917–1924, arXiv:0911.5370 [hep-ph]. http://www.sciencedirect.com/science/article/pii/S0010465510002602.

[58] T. Sjostrand, S. Mrenna, and P. Z. Skands, "PYTHIA 6.4 Physics and Manual," J. High Energy Phys. 0605 (2006) 026, arXiv:hep-ph/0603175 [hep-ph]. http://iopscience.iop.org/1126-6708/2006/05/026/.

[59] G. Corcella, I. Knowles, G. Marchesini, S. Moretti, K. Odagiri, et al., "HERWIG 6: An event generator for hadron emission reactions with interfering gluons (including supersymmetric processes)," J. High

Energy Phys. 0101 (2001) 010, arXiv:hep-ph/0011363 [hep-ph]. http://iopscience.iop.org/1126-6708/2001/01/010/.

[60] ATLAS Twiki Pages. https://twiki.cern.ch/twiki/bin/view/AtlasPublic/LuminosityPublicResults.

[61] ATLAS Collaboration, "The ATLAS Experiment at the CERN Large Hadron Collider," Journal of Instrumentation 3 (2008) S08003. http://iopscience.iop.org/1748-0221/3/08/S08003/.

[62] J. L. Caron, "ATLAS detector in A4 format with English captions. Détecteur ATLAS format A4 avec légende et caractéristiques en anglais.," March, 1998. http://cds.cern.ch/record/841458/.

[63] ATLAS Collaboration, "The trigger chambers of the ATLAS muon spectrometer: Production and tests," Nucl. Instrum. Meth. A 535 (2004) 265–271. http://www.sciencedirect.com/science/article/pii/S0168900204016511.

[64] ATLAS Collaboration, "Luminosity determination in pp collisions at $\sqrt{s} = 7$ TeV using the ATLAS detector at the LHC," Eur. Phys. J. C 71 (2011) 1630, arXiv:1101.2185 [hep-ex]. http://link.springer.com/article/10.1140%2Fepjc%2Fs10052-011-1630-5.

[65] van der Meer, S., "Calibration of the Effective Beam Height in the ISR," CERN-ISR-PO-68-31 (1968) . http://cds.cern.ch/record/296752?ln=en.

[66] S. Dimopoulos and G. L. Landsberg, "Black Holes at the Large Hadron Collider," Phys. Rev. Lett. 87 (2001) 161602, arXiv:hep-ph/0106295 [hep-ph]. http://link.aps.org/doi/10.1103/PhysRevLett.87.161602.

[67] ATLAS Collaboration, "Search for microscopic black holes in multijet final states with the ATLAS detector at $\sqrt{s} = 7$ TeV,". http://inspirehep.net/record/1204114.

[68] T. Sjostrand, S. Mrenna, and P. Z. Skands, "A brief introduction to PYTHIA 8.1," Comput. Phys. Commun. 178 (2008) 852–867, arXiv:0710.3820 [hep-ph]. http://www.sciencedirect.com/science/article/pii/S0010465508000441.

[69] M. Bahr, S. Gieseke, M. Gigg, D. Grellscheid, K. Hamilton, et al., "Herwig++ physics and manual," Eur. Phys. J. C 58 (2008) 639–707, arXiv:0803.0883 [hep-ph]. http://link.springer.com/article/10.1140/epjc/s10052-008-0798-9.

[70] ATLAS Collaboration, "The ATLAS simulation infrastructure," Eur. Phys. J. C 70 (2010) 823–874, arXiv:1005.4568 [physics.ins-det]. http://cds.cern.ch/record/1267853?ln=en.

[71] GEANT4 Collaboration, "Geant4 − a simulation toolkit," Nucl. Instrum. Methods Phys. Res. Sect. A 506 (2003) 250 – 303. http://www.sciencedirect.com/science/article/pii/S0168900203013688.

[72] ATLAS Collaboration, "Summary of ATLAS Pythia 8 tunes," ATL-PHYS-PUB-2012-003, ATL-COM-PHYS-2012-738 (2012) . http://cds.cern.ch/record/1474107?ln=en.

[73] H.-L. Lai, M. Guzzi, J. Huston, Z. Li, P. M. Nadolsky, J. Pumplin, and C.-P. Yuan, "New parton distributions for collider physics," Phys. Rev. D 82 (Oct, 2010) 074024, arXiv:arXiv:1007.2241 [hep-ph]. http://link.aps.org/doi/10.1103/PhysRevD.82.074024.

[74] S. Gieseke, C. Rohr, and A. Siodmok, "Colour reconnections in Herwig++," Eur. Phys. J. C 72 (2012) 2225, arXiv:1206.0041 [hep-ph]. http://link.springer.com/article/10.1140%2Fepjc%2Fs10052-012-2225-5.

[75] J. Pumplin, D. R. Stump, J. Huston, H.-L. Lai, P. Nadolsky, and W.-K. Tung, "New generation of parton distributions with uncertainties from global QCD analysis," J. High Energy Phys. 2002 (2002) 012, arXiv:hep-ph/0201195 [hep-ph]. http://iopscience.iop.org/1126-6708/2002/07/012.

[76] W. Lampl, P. Loch, S. Menke, S. Rajagopalan, S. Laplace, G. Unal, H. Ma, S. Snyder, D. Lelas, and D. Rousseau, "Calorimeter clustering algorithms: Description and performance," ATL-LARG-PUB-2008-002 (2008) . http://cds.cern.ch/record/1099735.

[77] M. Cacciari, G. P. Salam, and G. Soyez, "The anti-k$_t$ jet clustering algorithm," J. High Energy Phys. 0804 (2008) 063, arXiv:0802.1189 [hep-ph]. http://iopscience.iop.org/1126-6708/2008/04/063/.

[78] ATLAS Collaboration, "Jet mass and substructure of inclusive jets in $\sqrt{s} = 7$ TeV pp collisions with the ATLAS experiment," J. High Energy Phys. 1205 (2012) 128, arXiv:1203.4606 [hep-ex]. http://link.springer.com/article/10.1007/JHEP05(2012)128.

[79] ATLAS Collaboration, "Jet energy measurement with the ATLAS detector in proton-proton collisions at $\sqrt{s} = 7$ TeV," Eur. Phys. J. C 73 (2013) 2304, arXiv:1112.6426 [hep-ex]. http://link.springer.com/article/10.1140/epjc/s10052-013-2304-2.

[80] ATLAS Collaboration, "A search for new physics in dijet mass and angular distributions in pp collisions at $\sqrt{s} = 7$ TeV measured with the ATLAS detector," New J. Phys. 13 (2011) 053044, arXiv:1103.3864 [hep-ex]. http://iopscience.iop.org/1367-2630/13/5/053044/.

[81] ATLAS Collaboration, "Search for new physics in dijet mass and angular distributions using 4.8 fb^{-1} of pp collisions at $\sqrt{s} = 7$ TeV collected by the ATLAS detector," ATLAS-CONF-2012-038 (2011) . http://cds.cern.ch/record/1432206.

[82] ATLAS Collaboration, "Search for new phenomena in the dijet mass distribution using 5.8 fb^{-1} of pp collisions at $\sqrt{s} = 8$ TeV collected by the ATLAS detector," ATLAS-CONF-2012-088 (2012) . http://cds.cern.ch/record/1460400.

[83] CDF Collaboration, "Search for new particles decaying into dijets in proton-antiproton collisions at $\sqrt{s} = 1.96$ TeV," Phys. Rev. D 79 (2009) 112002, arXiv:0812.4036 [hep-ex]. http://prd.aps.org/abstract/PRD/v79/i11/e112002.

[84] CMS Collaboration, "Search for dijet resonances in 7 TeV pp collisions at CMS," Phys. Rev. Lett. 105 (2010) 211801, arXiv:1010.0203 [hep-ex]. http://prl.aps.org/abstract/PRL/v105/i21/e211801.

[85] ATLAS Collaboration, "Jet energy resolution in proton-proton collisions at $\sqrt{s} = 7$ TeV recorded in 2010 with the ATLAS

detector," Eur. Phys. J. C 73 (2013) 2306, arXiv:1210.6210 [hep-ex]. http://link.springer.com/article/10.1140%2Fepjc%2Fs10052-013-2306-0.

[86] ATLAS Collaboration, "Jet energy measurement with the ATLAS detector in proton-proton collisions at $\sqrt{s} = 7$ TeV," Eur. Phys. J. C 73 (2013) 2304, arXiv:1112.6426 [hep-ex]. http://link.springer.com/article/10.1140/epjc/s10052-013-2304-2.

[87] ATLAS Collaboration, "Expected performance of the ATLAS experiment - detector, trigger and physics," arXiv:0901.0512 [hep-ex]. http://cds.cern.ch/record/1125884?ln=en.

[88] A. L. Read, "Presentation of search results: The CL(s) technique," J.Phys. G28 (2002) 2693–2704. http://iopscience.iop.org/0954-3899/28/10/313/.

[89] G. Cowan, K. Cranmer, E. Gross, and O. Vitells, "Asymptotic formulae for likelihood-based tests of new physics," Eur. Phys. J. C 71 (2011) 1554, arXiv:1007.1727 [physics.data-an]. http://link.springer.com/article/10.1140%2Fepjc%2Fs10052-011-1554-0.